ADDIS ABABA UNIVERSITY
COLLEGE OF NATURAL AND COMPUTATIONAL SCIENCES
MATERIALS SCIENCE PROGRAM

Ternary Composite Materials based on Manganese Dioxide Doped Reduced Graphene Oxide and Conducting Polymer Electrode Material for Supercapacitors

By:

Peninah Nzangi Mwilu (Id No: GSR/5774/14)

Supervisor: Dr. Girum Ayalneh Tiruye (PhD)

March, 2024
Addis Ababa, Ethiopia

ADDIS ABABA UNIVERSITY
COLLEGE OF NATURAL AND COMPUTATIONAL SCIENCES
MATERIALS SCIENCE PROGRAM

Ternary Composite Materials based on Manganese Dioxide Doped Reduced Graphene Oxide and Conducting Polymer Electrode Material for Supercapacitors

By:

Peninah Nzangi Mwilu (Id No: GSR/5774/14)

Supervisor: Dr, Girum Ayalneh Tiruye (PhD)

A Master's thesis submitted to the Materials Science Program, Addis Ababa University in partial fulfilment of the requirements for The Degree of Master of Science in Materials science

Declaration

I, Peninah Nzangi Mwilu (Id No: GSR/5774/14), hereby declare that this MSc research thesis titled "Ternary Composite Material based on Manganese Dioxide Doped Reduced Graphene Oxide and Conducting Polymer Electrode Material for Supercapacitor'' has been conducted by me and has not been submitted to any other institution for award of any academic qualification. The content of the thesis has not been plagiarized and where works of other researchers have been used, they have been appropriately cited.

Candidate's Name	**Signature**	**Date**
PENINAH NZANGI MWILU		19/03/24

APPROVED BY BOARD OF EXAMINERS

This is to certify that we have read this MSc research thesis and that in our opinion; it is fully adequate, in scope and quality, as a Master's thesis for The Degree of Master of Science in Materials Science

Advisor

Dr. Girum Ayalneh Signature Date: 16/03/2024

External Examiner

Dr. Getachew Adam Signature Date 19/03/2024

Internal Examiner

Dr. Georgis Alene Signature Date 19/03/2024

Chairperson

Dr. Getachew Gizaw Signature Date 19/03/2024

Abstract

Ideal energy storage devices should have both high energy and power density. Electrodes having high specific surface area and thinner dielectrics are used in supercapacitors. Because of these characteristics, they have power and energy densities that are higher than those of batteries and traditional capacitors, respectively. In this work, a ternary composite comprising reduced graphene oxide, Manganese dioxide, and poly-2,5-dimethylaniline (rGO/MnO_2/PDMA) was synthesized via in-situ polymerization. To investigate the effect of manganese dioxide on the composite material, different ratios of MnO_2 (80%,60%, and 30%) were synthesized.

The characterization techniques employed are Fourier-Transform Infrared (FTIR), X-ray Diffraction (XRD), Brunner Emmet Teller (BET), and Scanning Electron Microscopy-Energy Dispersive Spectroscopy (SEM-EDS), Cyclic Voltammetry (CV), Galvanostatic Charge/Discharge (GCD), and Electrochemical Impedance Spectroscopy (EIS) techniques in 1MNa_2SO_4.

A maximum specific capacitance of 176.4F/g for rGO/MnO_2/PDMA in a three-electrode system was attained at a current density of 0.0016A/cm^2. 80%MnO_2 had the best electrochemical performance and the performance dwindled as the ratio of MnO_2 decreased. Asymmetric electrodes performed better than symmetric electrodes in a two-electrode system with maximum specific capacitance values registered at 0.0016A/cm^2 current density for ternary composites as 86 F/g respectively. The ternary composite performed better than the binary composite and the conducting polymer. Despite excellent performance by rGO, it is very expensive and therefore uneconomical for commercial applications. This opens possible research opportunities that aim to use it in small quantities to increase the conductivity and specific capacitance of other cheaper materials, to lower production cost.

Keywords: reduced graphene oxide(rGO), Supercapacitors, specific capacitance, Two-electrode system, Three-electrode system, Asymmetric configuration, Ternary composite

Acknowledgment

First and foremost, I would like to thank God almighty for granting me life, energy, and good health to conduct my research. My sincere gratitude goes to my advisor and the coordinator of the ESIMSAD program, Dr. Girum Tiruye Ayalneh, for his informed guidance, encouragement, and great support in delivering this master's research. He has been a priceless advisor to me and has advised me on my studies. Despite his extremely busy schedule, he has always made himself available to direct and offer guidance whenever called upon. This work would not have been duly completed without his guidance and motivation. I would also like to acknowledge all my lecturers from the materials science department, Dr. Manalebish, Dr. Yedilfana, Dr. Getachew, Dr. Amare, and Prof.Shimelis, who have seen me through all my coursework since I started my program, they have been so kind and supportive for my entire stay here. Particularly, I would like to recognize Dr. Yeldilfana's commitment to include me in many forums, especially for CNCS-AAU, the Computational Society of Ethiopia, and the Chemical Society of Ethiopia community and always welcoming me to attend and learn from those forums. Such inclusivity has given me a sense of belonging and made me feel at home despite being many miles away from home. I want to extend my sincere gratitude to the ESIMSAD program under the sponsorship of the European Union in collaboration with the African Union for giving me this life-changing opportunity to further my studies and for sponsoring my studies and ensuring a comfortable life by facilitating my stay during my study period. Similarly, I would like to thank my host university AAU for helping me to settle in and offering accommodation services and security for the entirety of my stay in Ethiopia. I will forever be grateful for the kindness shown to me by the entire AAU fraternity including the support staff, they became my family when my biological family was far away and I will forever cherish their contributions to my academic success. Finally, I would like to acknowledge my Family for their prayers, support, and encouragement they offered me during my studies and for always cheering me on and wishing me the very best in life, I owe my success to them as well for always helping me see past the challenges I encountered in life and for motivating me to push past my comfort zone to unveil unending new opportunities in life.

Contents

List of tables

List of Figures

List of acronyms

rGO	reduced graphene oxide
DMA	2,5-demethoxyaniline
PDMA	poly (2,5-dimethoxy aniline)
EDLCs	Electrochemical double-layer capacitors
SCs	Supercapacitors
TMO	Transition metal oxides
PTFE	Polytetrafluoroethylene
ESs	Electrochemical supercapacitors
ESPW	Electrochemical stable potential window
IL	Ionic liquids
OEs	Organic electrolytes CPs
Conducting polymers MOFs	
Metal-organic frameworks P_d	
Power density	
E_d	Energy density
FTIR	Fourier transform infra-red
XRD	X-ray diffraction
SEM	Scanning electron microscopy
GCD	Galvanostatic charge-discharge
EIS	Electrochemical impedance spectroscopy
CV	Cyclic voltammetry
BET	Brunner-Emmett-Teller
XPS	X-ray photoelectron spectroscopy
CNTs	Carbon nanotubes
PANI	Polyaniline
PPy	Polypyrrole
WE	Working electrode
RE	Reference electrode
CE	Counter electrode
GPEs	Gel polymer electrolytes
SPEs	Solid polymer electrolytes
ECPs	Electronically conducting polymers
GNF	Graphite nanofibers
ESR	Electrochemical series resistance
ASCs	Asymmetric supercapacitors
MnO_2/PDMA-80%-60%-30%	The % of MnO_2 in binary composite
rGO/MnO_2/PDMA-80%-60%-30%	The % of MnO_2 in the ternary composite

Chapter One

1. Introduction

1.1. Background of the study

In the modern environment, practically every human function is facilitated and efficient by the use of electronic equipment. These are so important that a country's economic development is significantly influenced by its technological growth. However, renewable energy sources such as solar, wind, and hydroelectric power are intermittent and therefore not always accessible. Dependable electrochemical energy storage devices such as batteries and supercapacitors need to be connected to these energy sources to enable accessibility to energy at all times. The increasing use of electronic gadgets and the rapidly expanding number of automated cars are placing a great deal of demand on the world's conventional energy sources, such as fossil fuels, hastening their rapid depletion[1]. Furthermore, the overuse of these conventional fuels endangers the environment by releasing CO_2 into the atmosphere, which causes pollution and global warming[2]. To lessen these worldwide concerns, it is imperative to connect energy-driven technology with sporadic energy sources like solar or wind energy. To provide a steady power supply, these energy sources must be connected to efficient electrochemical energy storage devices[3].

Complementary electronic device characteristics are mostly determined by the dimensions, price, and adaptability of different energy storage systems. Batteries are among the most well-known and widely used electrochemical energy storage systems in use today. However, these present serious problems owing to their short cycle times, use of hazardous chemicals, inadequate power density, and safety concerns[4]. Supercapacitors are an essential complement to batteries in this situation because of their extended cycle life, low maintenance needs, high power densities, and quick rates of charge and discharge[5]. Nevertheless, when supercapacitors are utilized with equipment that needs to function for extended periods between charges, their low energy density still presents a problem (*Figure 1*). Because the performance of a supercapacitor is heavily influenced by its electrode materials, scientists from all over the world are trying to come up with new ways to make effective electrode materials that are low-cost, non-toxic, lightweight, have a long cycle life, and have both a higher energy density and a higher power density [6].

Furthermore, it has been discovered that electrolytes are one of the key elements affecting how electrochemical supercapacitors (ESs) function. The electrolytes are classified into several categories, including organic, ionic, aqueous, solid-state or quasi-solid-state, and redox-active electrolytes.

The electrochemical stable potential window of the electrolytes is a key factor in defining the operating cell voltage of the ESs assuming the electrode materials remain stable over the working voltage range. Apart from the operational voltage window's crucial function in the determination of the energy density of an electrolyte or solution, these properties also include power density, internal resistance, rate performance, operating temperature range, cycling lifetime, self-discharge, and toxicity, all of which are significant for the practical applications of electrolytes and solutions. For instance, because the average potential of the aqueous electrolyte is around 1.23 V (the potential window of H_2/O_2 evolution processes at 1.0 atm and ambient temperature), aqueous electrolyte-based ESs normally have a working potential window of approximately 1.0–1.3 V.

Conversely, the potential windows of ionic liquid (IL) and organic electrolyte (OE) based devices are typically 3.5–4.0 V and 2.5–2.7 V, respectively. Along with the electrolyte potential window property, the electrolyte-electrode material interaction plays a major function in the performance of electrolytes. For example, the relationship between the size of the electrolyte ions and the carbon electrode material pore size has a significant impact on the possible specific capacitance.

Ionic conductivity is a major factor in electrolyte internal resistance, mostly for organic and ionic liquids electrolytes. The electrolytes' boiling point, viscosity, and freezing point can also have a major effect on their thermal stability and, thus, their operating temperature range. Aging and ES failure are also related, as was previously indicated, to the electrochemical degradation of the electrolytes. Intriguingly, new electrolytes—like solid-state electrolytes—are essential to the evolution of multiple novel types of electrochemical sensors (ESs), including micro-electrochemical sensors and pliable or solid-state ESs.

In recent years, tremendous development has been accomplished in the study and production of ES electrolytes using a wide range of electrolyte types, including aqueous, organic, IL, redox-type, solid, and semi-solid. For example, using neutral aqueous electrolytes has been found to greatly extend the operating potential of ESs (aqueous electrolyte-based electrochemical sensors) to approximately 2 V. Numerous innovative organic electrolytes that offer ESs larger operating potential windows and lower toxic levels in comparison to commercially available organic electrolytes have been made. With the evolution of Ionic liquids (IL) electrolytes, the operating cell voltage of the associated electrochemical sensors was improved to 4 V despite their high viscosity and low ionic conductivity.

Furthermore, in contrast to their liquid electrolyte-based counterparts, flexible or solid-state electrolyte replacements ESs have been developed in the hunt for solid or semi-solid electrolytes and are claimed to be leak-free. Redox-type electrolytes have also recently been proposed as electrolytes for electrochemical sensors ESs because of the added pseudocapacitance from the electrolyte's redox reaction at the electrode/electrolyte interface.

Ideal electrolyte needs to meet several requirements such as compatibility with electrolyte materials, flammability, a wide operating temperature range, affordability, low volatility environmental friendliness, great chemical, electrochemical, and ionic conductivity stability, and high electrochemical and chemical inactiveness to ES components like current collectors, packaging and electrodes. However, it is challenging for an electrolyte to meet all these needs as every electrolyte has its advantages and disadvantages. Therefore, there is a lot of research going on to increase the performance of electrolytes and correlated ESs[7].

Most commercially available supercapacitors produce an electric double-layer capacitor (EDLC) by utilizing carbon electrodes to store charge. Some charge that can be held in these EDL capacitors is severely limited since the electrolyte physically interacts with the electrode surface to keep the charge. Consequently, scientists are working to develop new materials that can undergo redox processes to boost the supercapacitor’s capacitance, energy, and power densities. Redox-active materials that may store charge through a highly reversible redox interaction with the electrolyte include metal oxides, conducting polymers (CPs), Metal-Organic Frameworks (MOFs), and MXenes [8].

Due to their enormous surface area, adjustable architectures, and lack of toxicity, conducting polymers are of particular interest among these materials [9]. However, these materials do have certain inherent shortcomings, like low electrical conductivity and unstable structural properties. Fortunately, by adding other materials to carbon-based electrodes to produce synergistic effects with unique properties from both parent materials, these disadvantages can be potentially eliminated[10]. Because of their multiple oxidation states and affordability, metal oxides have become a desirable electrode material for supercapacitors.

The primary disadvantages of metal oxides include their poor electrical conductivity, susceptibility to acidic solutions, and challenges in processing them to make electrodes. On the other hand, despite their good conductivity and ease of synthesis, conducting polymers lack mechanical integrity and have a short cycle life, which limits their practical usage. To overcome one another's shortcomings and produce a potential composite material for supercapacitor applications, conducting polymers and metal oxide can combine to form composites[11].

This study is focused on synthesizing a ternary composite of reduced graphene oxide (rGO) with manganese dioxide (MnO_2), and poly 2,5-dimethoxy aniline (PDMA), (rGO/MnO_2 /PDMA). This combines the high conductivity advantages of rGO with the high energy storage capacity of MnO_2 and PDMA[12]. For electrochemical supercapacitors in particular, manganese dioxide is regarded as the most promising electrode material due to its affordability, favorable electrochemical reactivity, and environmental compatibility.

Recent research demonstrates the exceptional performance of electrochemical supercapacitors built on thin manganese oxide films produced on conductive substrates. Additionally, their shape, electrical conductivity, and surface area are all closely correlated with their specific capacitance [13]. Graphene is the ideal electrode material for electrochemical double-layer capacitors due to its outstanding electrical conductivity, high surface area, mechanical strength, fracture strength, and great chemical stability. Because graphene layers exhibit lower capacitance and re-stack even after exfoliation, they should be combined with conductive polymers or transition metal oxide/hydroxide/sulfides to be employed in supercapacitor applications [14].

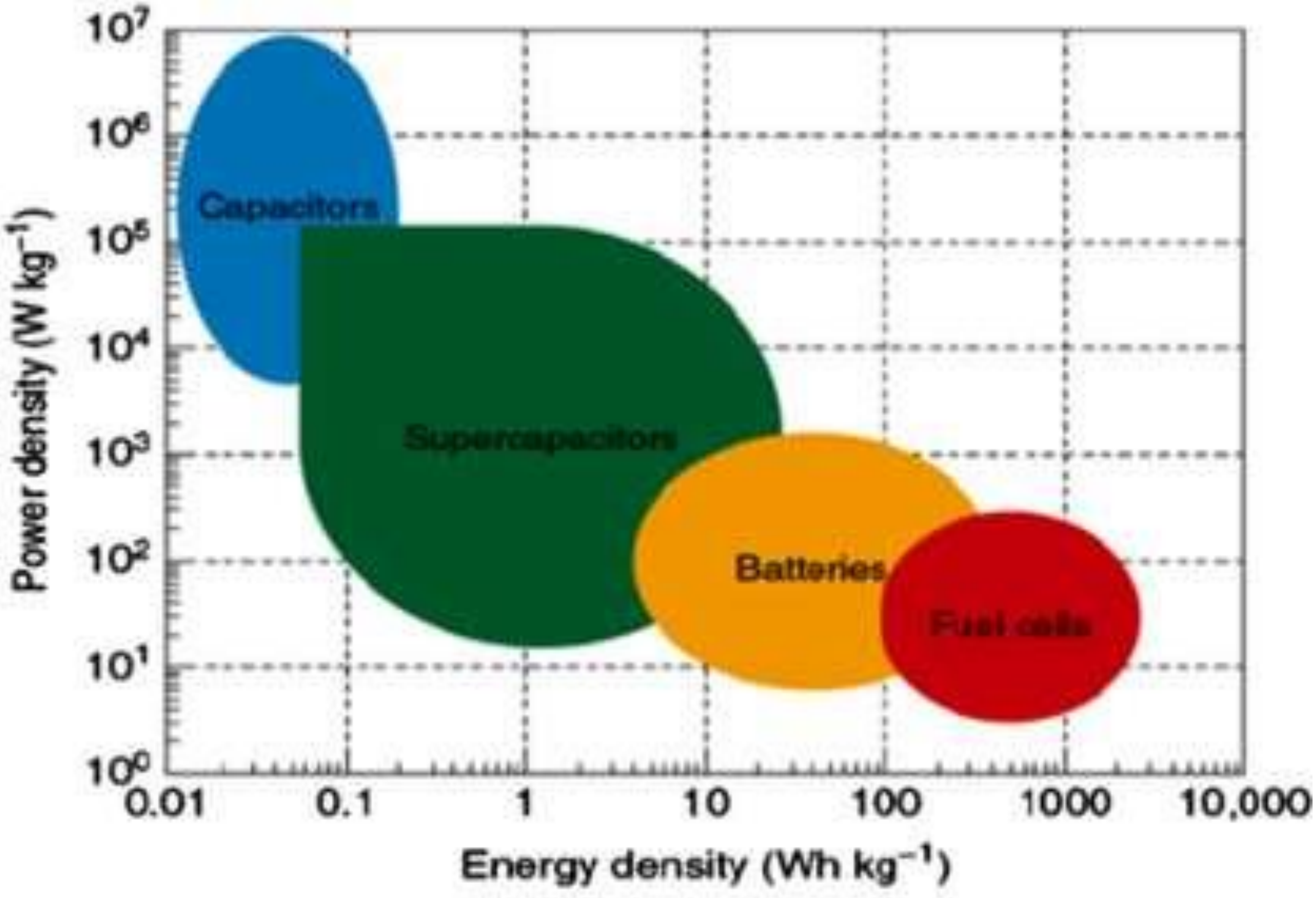

Figure 1. A Ragone plot of energy density (Wh/kg) against power density(W/kg) for energy storage devices[15]

1.2. Statement of the Problem

Renewable energy storage technologies are without a doubt one of the difficulties the world is facing in this century. Supercapacitors and batteries are the two main electrochemical energy storage technologies applied for versatile energy applications. Batteries are complementary to supercapacitors as they are characterized by high energy density but lower power density compared to supercapacitors. Despite both devices being suitable for energy storage, batteries are faced with serious challenges such as short service life, and lower reliability compared to supercapacitors. By using appropriate design and effective materials, SCs could outperform batteries in terms of energy and power densities by a great extent, making them a versatile alternative for energy storage. As a result, to meet the demands of growing ecological concerns and modernization, new, inexpensive, and environmentally friendly energy storage technologies must be devised. The emergence of supercapacitors has proven to be a potential alternative to other energy storage devices, however, there is quite a long way to go for this to be realized. This is because supercapacitors confront several difficulties, with low energy density, high production costs, high self-discharge, and low voltage per cell taking the top spots. Creating new electrode materials for supercapacitors with a high specific area and high conductivity is one of the most intensive ways to get around the problem of low energy density [16].

In response to these challenges, it is, without a doubt vital that new electrode materials be fabricated in the quest to carb these challenges and hopefully achieve better energy storage capabilities compared to the conventional supercapacitors. Having said this, composite electrode materials seem to be the probable solution to the supercapacitors and therefore worth dedicating the research towards. Particularly, there is limited research related to the capacitive performance of tertiary composite materials based on reduced graphene oxide, metal oxides, and conducting polymer literature. Therefore, this work will focus on synthesizing composite electrode materials from reduced graphene oxide, manganese dioxide, and polyaniline derivative, to generate information about the capacitive performance of the composite electrode material in supercapacitors.

1.3. Research Questions

1.3.1. General Research Questions

i. What is the electrochemical capacitive performance of the synthesized composite material and how does it compare with those of the individual electrode materials that make up the composite material?

ii. How do the spectroscopic parameters of the synthesized composite materials compare to those of the standard?

1.3.2. Specific Research Questions

i. What are the electrochemical (EIS, CV, and CD) performances of the synthesized composite materials and how do they compare with those of the individual electrode materials that make up the composite materials?
ii. How do the FTIR, SEM, BET, and XRD results of the synthesized ternary and binary composite materials compare to the individual components, rGO, and PDMA synthesized materials?

1.4. Objectives

1.4.1. General Objective

The general objective of this thesis is to Synthesize and characterize a ternary composite material based on manganese dioxide nanoparticles doped poly (2,5-dimethoxy aniline) using reduced graphene oxide as a matrix for electrode materials for high-performance supercapacitors.

1.4.2. Specific Objectives

i. To determine the physicochemical properties of reduced graphene oxide (rGO) and PDMA
ii. To explore a nanocomposite of manganese oxide nanoparticles and PDMA as electrode materials for supercapacitors
iii. To establish the performance of a ternary composite based on rGO and manganese oxide doped poly (2,5-dimethoxy aniline).

1.5. Relevance of the Study

This work is justified by the fact that supercapacitors do not release toxic chemicals to the environment and are therefore, safe for use in many energy storage applications especially in the effort of coupling intermittent renewable energy resources with energy storage devices to fight climate change in the rapidly growing world economy. The research on supercapacitors is quite new in the science society and therefore there is limited information available and a lot of knowledge to be gained in the future. It is factual to point out that superior electrode materials with both high energy and power densities are yet to be achieved and therefore the need for researchers to be relentless in trying out different combinations of electrode materials with different advantageous qualities to determine which ones give better and viable results. In particular, there is no literature available about electrode materials MnO_2/PDMA and rGO/MnO_2/PDMA.

1.6. The Scope of the Study

This research is focused only on the synthesis and characterization of the ternary composite based on rGO, metal oxide (MnO_2), and derivative of conducting polymer (PDMA). The study aimed to create a high-performance electrode material, with high specific capacitance, energy, and power density for supercapacitor application. The performance of composite material was investigated by calculating the specific capacitance, energy, power densities, and electrical series resistance of the composite. This research was conducted in the photovoltaic laboratory at the materials science program at Addis Ababa University.

The study was conducted over six months, between the 15th of August 2023 and the 15th of January 2024. The chemicals used in this experimental research were provided by the materials science program and all the electrochemistry analyses were conducted using the electrochemical station at the same laboratory. The following characterization techniques employed in this study are; FTIR for chemical structure and functional groups determination, XRD for accessing the crystallinity of the samples, SEM for elucidation of structural morphology, and BET for surface area, particle size, and porosity determination. For electrochemical characterization, CV, GCD, and EIS were used.

Chapter Two

2. Literature Review

2.1. Supercapacitors as Energy Storage Devices

Energy sources are the most significant and powerful untapped resource for mankind, and they can change the course of human history[10]. Modern human growth depends heavily on the utilization of many energy resources, including wind, fossil fuels, geothermal, atomic, chemical, and solar energy, among others, in all sectors of society[1]. Finding effective and ecologically friendly ways to store excess energy is now essential to provide a steady supply of energy for various electrical equipment. The two most often used categories of electrochemical energy storage devices are supercapacitors and batteries[17].

The components of a supercapacitor are two electrodes, an appropriate electrolyte, and a separator. The electrodes submerged in the electrolyte have a major impact on the supercapacitor's performance. Supercapacitors have several advantages over conventional energy storage technologies, including a long lifespan, pliable packaging, high power, a broad temperature range (-40°C to 70°C), lightweight, and little maintenance [16]. Supercapacitors are especially useful in applications requiring short load cycles, high power delivery, and high reliability, like electric cars, load cranes, forklifts, and energy recapture sources.

There are two types of supercapacitors: pseudo-capacitors and electrochemical double-layer capacitors (EDLCs). The two types differ in how they store energy. The much quicker charge-discharge process in EDLC devices can complete over 100,000 cycles in a matter of seconds. The compact Helmholtz layer, the diffusions layer in the electrolyte, and the space charge layer in the electrode make up an EDLC, which has a thickness of around 1 nm[18]. The EDLCs' capacitive performance is ascribed to electrical charge storage at the interface of electrolyte and electrode, which is merely a physical procedure of adsorption-desorption of ions on the electrodes' surface and devoid of faradaic processes. Consequently, excellent cycle performance and rapid charging and discharging rates can be achieved with EDLCs[19].

EDLCs have a high power density and low energy density because of the partial contact that exists between the porous electrodes and the electrolyte. In contrast to EDLCs, conducting polymers and transition metal oxides/hydroxides, which are the active components of pseudocapacitors, are responsible for the rapid and reversible redox reaction that generates their capacitance[20]. Due to the low conductivity of pseudocapacitive materials, pseudocapacitors can consequently yield larger specific capacitance at lower power densities. As a result, carbon compounds with electrical double-layer capacitance are often coupled with pseudocapacitive materials to improve the overall electrode performance[21].

2.2. Reaction Mechanisms in Supercapacitors

EDLCs' capacitance is determined by the reversible accumulation of electric charge on the electrode surface, and this is majorly influenced by the specific surface area of the electrode materials. When an electrical potential difference is applied between the two electrodes, the cations and anions in the electrolyte migrate towards the surfaces of the negatively charged electrode and the positively charged electrode, respectively, to balance the electrons and holes (as shown in *Figure 2*). The Stern model can be used to simulate both the accumulation of cations and anions on electrode surfaces and the movement of ionic species in diffuse layers.

The following equation can be used to express the electrode's total capacitance (Ct):

$$\frac{1}{C_t} = \frac{1}{C_H} + \frac{1}{C_D} \qquad (1)$$

here the capacitances at the diffuse layer and the Helmholtz layer are denoted by the letters C_D and C_H, respectively. Since they have the advantages of a high surface area, high electrical conductivity, and electrochemical stability, nanocarbon electrode materials such as activated carbon, carbon nanotubes (CNTs), and graphene are often the most extensively utilized materials for EDLCs[16].

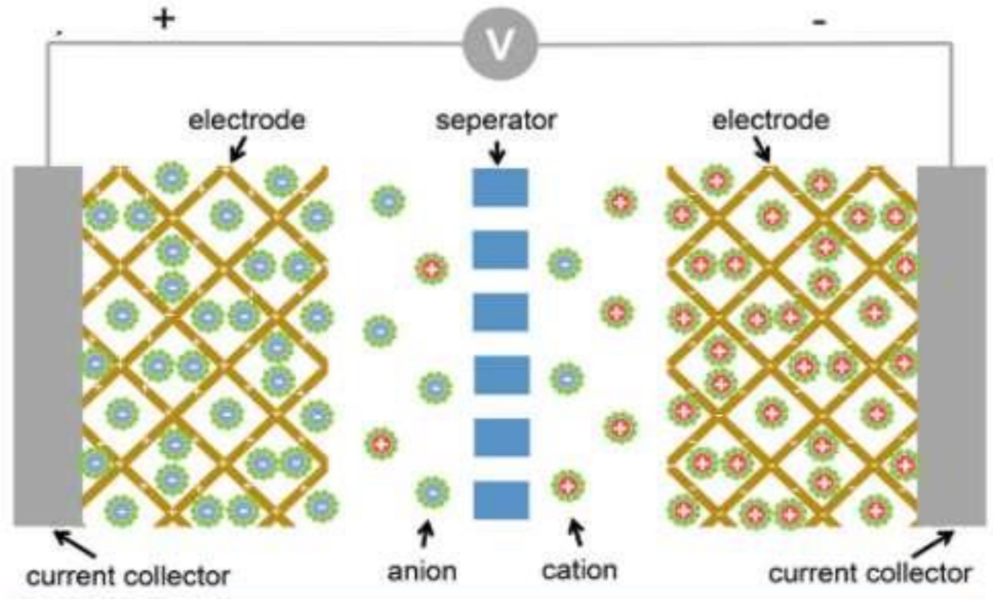

Figure 2. A schematic diagram of the energy storage mechanism of EDLCs[19]

Pseudocapacitors have a higher capacitance than EDLCs because of both the rapid and reversible redox reaction that occurs between the active components and the electrolyte. Therefore, compared to EDLCs, pseudocapacitors can supply capacitance at much higher values. The most widely used pseudocapacitive materials include conductive polymers, such as polyaniline [PANI] and polypyrrole [PPy], and transition metal oxides/hydroxides, such as RuO_2, MnO_2, and $Co\ (OH)_2$.

A simple equation for their reaction mechanisms is as follows:

$$M\text{�}^{+} + x\text{�}^{-} \rightarrow \text{��}(\text{�} - \text{��})^{+} \qquad (2)$$

For conductive polymers, reversible ion exchanges between the electrolyte and polymer backbone occur rapidly throughout the redox reactions. Selecting the proper potential window is essential for this operation since conductive polymers will easily break down outside of it or transition to an insulating state when the potential is too negative. Transition metal sites in oxides and hydroxides, in contrast to conductive polymers, frequently serve as redox-active centres to give different valence states. Despite having lesser conductivity than conductive polymers, they can have higher electrochemical stability. Pseudocapacitance active materials are usually incorporated into carbon-based materials to increase the total capacitance of the electrode materials through their interactions[22]. *Figure 3* below shows a general classification of different supercapacitors.

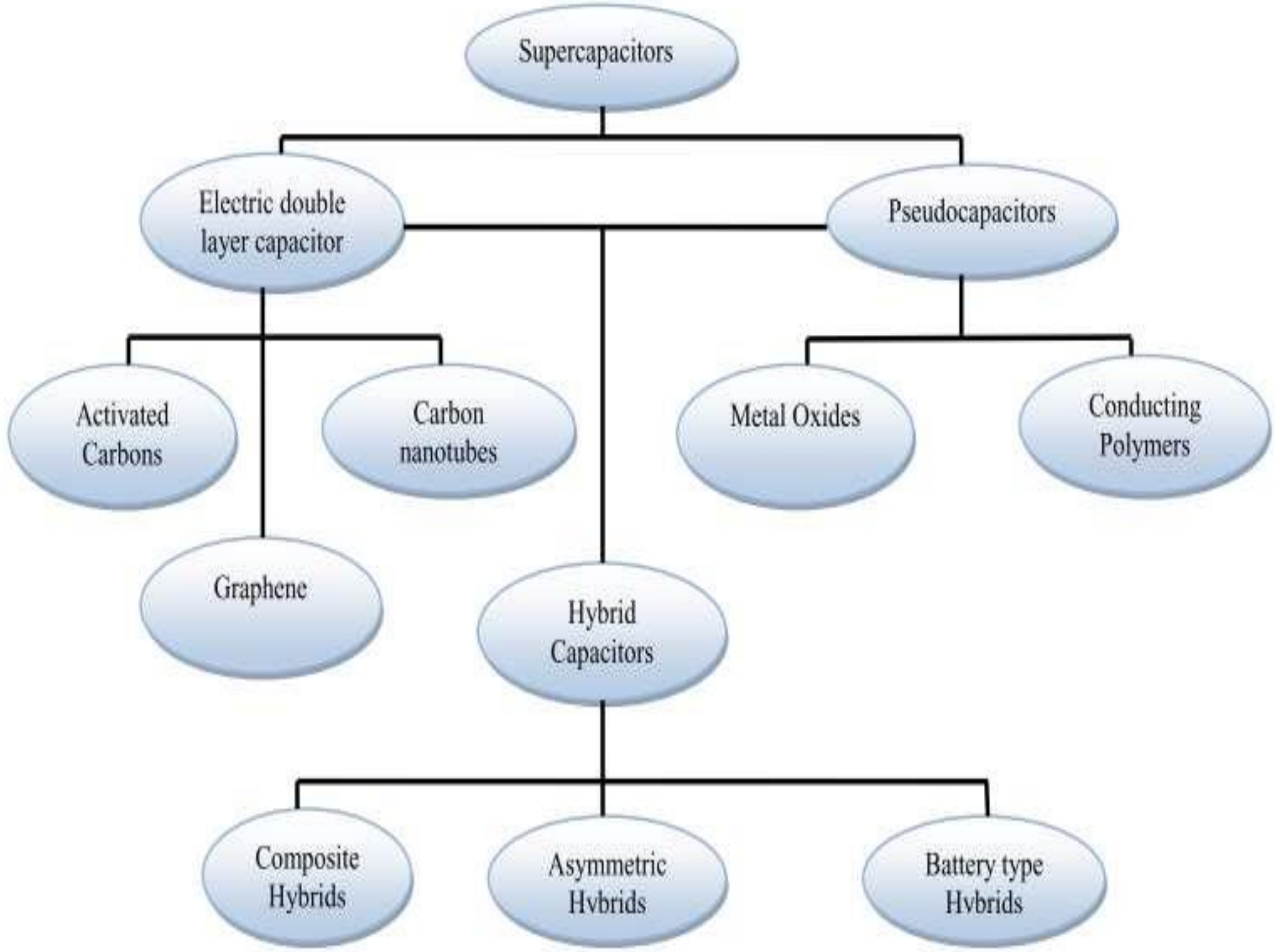

Figure 3. Classification of supercapacitors[23]

Researchers often use a two- or three-electrode setup to explore the electrochemical characteristics of the electrode active materials. The working electrode (WE), reference electrode (RE), counter electrode (CE), and electrolyte are the essential components of a three-electrode setup which is schematically depicted in *Figure 4*. In contrast, a two-electrode setup consists of a complete cell with two electrodes: the working electrode and the counter electrode. The working electrode might be utilized just as such or with an active chemical coated on it. Saturated calomel electrodes and platinum electrodes are commonly used as the reference electrode and counter electrode, respectively.

Most electrolytes are composed of organic solvents and aqueous solutions. Waste organic solvents should be replaced with aqueous solutions since they are less likely to contaminate the environment when used as electrolytes. Supercapacitors' electrochemical abilities are often assessed using galvanostatic charge-discharge (GCD), cyclic voltammetry (CV), and electrochemical impedance spectroscopy (EIS). The specific capacitance, cycle life, charge-discharge rate, and other metrics that are obtained from these methods are used by researchers to determine the electrochemical performance of a supercapacitor. With the constant current charge-discharge curve, the specific capacitance may be found using Equation (3)[24]:

$$C = \frac{I\Delta t}{M\Delta V} \qquad (3)$$

where I is the charge current, t is the discharge period, V is the potential window during the discharging process, M is the total mass of active materials, and C is the specific capacitance. The specific capacitance of the GCD method is dependent on the discharge current, active material mass, potential window, and discharge duration parameters.

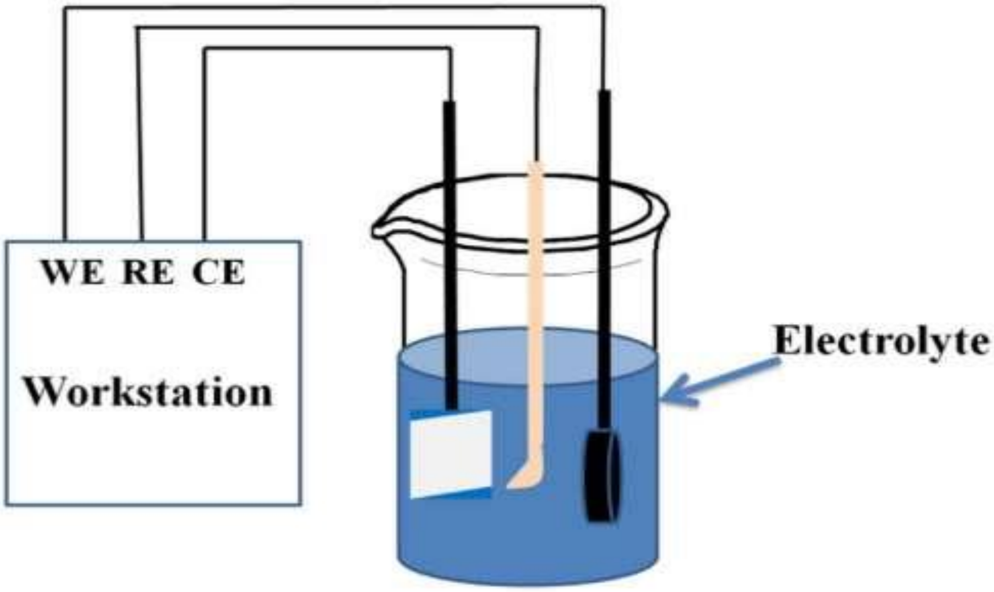

Figure 4. Schematic representation of a three-electrode system configuration[24]

variable currents can produce varying specific capacitance since defective active materials can have variable resistances (such as electrolyte and contact resistance, etc.). The reversibility of the charge-discharge process of active materials can be represented by the symmetry of the charge-discharge curves; the symmetry of the curves directly translates to the reversibility of the electrode materials. Additionally, the life cycle of the electrode materials can be examined using many constant current cycles of charge-discharge progress. Equation (4) provides the specific capacitance for the CV technique based on the CV curves[24]:

$$\text{�}= \frac{A}{(\text{��}\times\text{��}\times\text{��})} = \frac{\text{�}}{f} \qquad (4)$$

where A represents the integral area of the cyclic voltammogram curve, v is the voltage window, f is the scan rate, m represents the active material mass, and I is the charge-discharge current. The charge/discharge current and scan rate of an ideal supercapacitor are both constant, but because redox processes can happen at the interface, the real supercapacitor's CV curves inevitably stray from the ideal rectangle. As a result, the shape of CV curves can reveal information about the performance of supercapacitors. Specifically, for EDLCs, the capacitance performance is higher the closer the rectangle is to the center; for pseudocapacitors, the location of the redox reaction peak can reveal information about the kind of redox reactions occurring in the system. The cycle life of the supercapacitor may also be evaluated using the CV approach. The EIS approach can be used to visualize the kinetic characteristics of material diffusion and charge transfer at the electrode/solution interface using a Nyquist plot. Furthermore, the effectiveness of ESR and solution resistance functions can be ascertained with this technique.

2.3. Electrolytes used in Supercapacitors

Supercapacitor electrochemical performance is significantly influenced by the electrolyte, which is made up of salt and solution. In both the case of an EDLC and a pseudocapacitor, the electrolyte is an important source of information on the electrical double layer and redox reactions respectively. A supercapacitor typically uses three different types of electrolytes: quasi-solid-state, solid-state, and liquid-state. Aqueous, organic, and ionic electrolytes are subcategories of these liquid electrolytes, and organic and inorganic electrolytes are the general divisions of the solid and semi-solid electrolytes[7].

Aqueous electrolytes (e.g., H_2SO_4, KOH, Na_2SO_4, and NH_4Cl aqueous solution) usually have better conductivity than organic and ionic liquid electrolytes with a potential window of 1 V to 1.3 V. The potential window is restricted by acidic and alkaline electrolytes up to 1V-1.23 V, while the neutral electrolyte extends up to 1V-1.6 V[25].

To create the organic electrolytes used in supercapacitors, salts with high conductivity are dissolved in organic solvents. Because of their higher operating voltage, which is typically between 2.5 and 2.8 V, OEs currently control the majority of the market. The energy and power densities of cells improve dramatically with a broadened operating voltage. Additionally, using organic electrolytes lowers the overall cost of the supercapacitor cell by enabling the use of an inexpensive current collector and packing materials. The two solvents that are most frequently employed with organic electrolytes are propylene carbonate (PC) and acetonitrile (ACN). Organic electrolytes are more expensive, have a lower specific capacitance, are less conductive, and, most importantly, raise safety concerns due to their flammability and toxicity, despite having a greater operating cell voltage[26].

A lot of attention was drawn to ionic liquids, solvent-free electrolytes at room temperature, because of their stability and wide voltage window. Therefore, it is simple to adjust the chemical and physical properties of electrolytes by changing their anions and cations. Ionic liquids have garnered considerable interest as substitute electrolytes for supercapacitors due to their good conductivity (~10 mS cm-1) and higher potential window (2 to 6 V)[27]. Ionic liquids contain very little vapor pressure and are non-flammable, thermally, and chemically stable. Examples are Hydrophobic-butyl-N-methyl pyrrolidinium bis(trifluoromethanesulfonic) imide (PYR14TFSI) shown by Baldacci et al. to be a useful ionic liquid. Ionic liquids are, however, very expensive and therefore not economical for large-scale applications[28].

Solid electrolytes are known for their strong ionic conductivity. Solid-state electrolytes have dual functions as separators and high ionic conductivity electrolytes. Additionally, they simplify the supercapacitor cell's construction and packing. They perform well because they are lightweight. Polymer electrolytes, or solid-state organic electrolytes, and inorganic solid material electrolytes are the two main groups of solid-state electrolytes[29]. *Figure 5* demonstrates the classification of electrolytes used in supercapacitors.

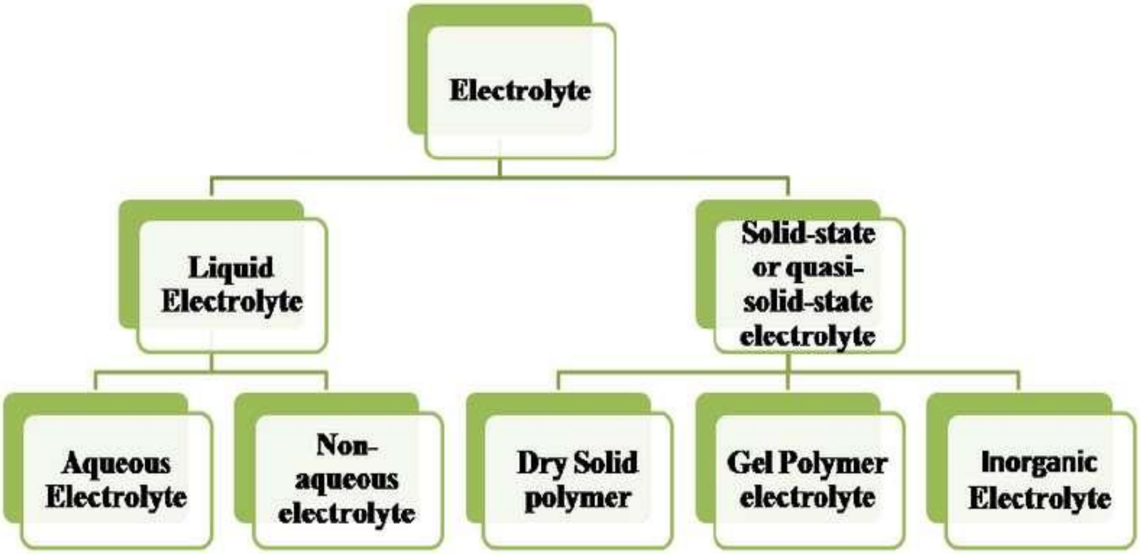

Figure 5. Classification of electrolytes for electrochemical supercapacitors[30]

2.4. Electrode Materials for Supercapacitors

Three types of materials can be used as electrodes: transition metal oxides (TMOs), conductive polymers, and carbon compounds.

2.4.1. Carbon Compounds

For Electrochemical Double double-layer capacitors (EDLCs), carbon compounds are typically utilized as the electrode material. They possess superior electrical conductivity, a large specific surface area, and a pore size distribution that may be adjusted. Carbon materials can offer high power densities but poor energy densities due to EDLCs' storing technique, which restricts total performance. For electrode materials, carbon-based materials including graphene, carbon nanotubes, and carbon nanofibers have been thoroughly investigated. Nevertheless, the performance of EDLCs is restricted by the low specific capacitance of carbon materials, and the high cost of those materials limits their applicability[31]. Among these carbon materials, reduced graphene oxide (rGO)(*Figure 6* b) is the most preferred electrode material because besides having two dimensional all -sp2 hybridized carbon (*Figure 6*), rGO exhibits good mechanical qualities, electronic transport properties, high surface area, and cycling stability[32].

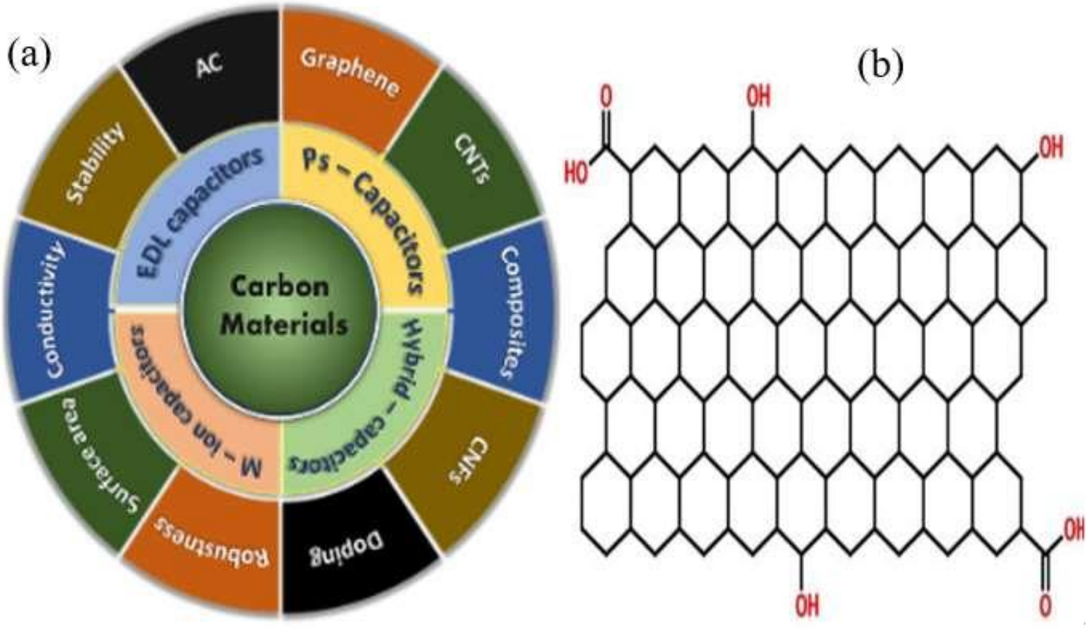

Figure 6. Examples of carbon-based electrode materials in supercapacitors(a), and chemical structure of reduced graphene oxide(b)

2.4.2. Conductive Polymers

Since their initial synthesis in 1862, Electronically conductive polymers also referred to as intrinsically conducting polymers (ICPs), have been classified as a group of organic polymers having high electronic conductivity [33]. Electronically conducting polymers (ECPs) are promising materials for the production of high-performing supercapacitors because they have high specific capacitances (charge processes affect the entire mass of the polymer, instead of just the surface, as in the case of double-layer activated carbons), high conductivities in the charged states, and generally quick charge-discharge processes.

The potential to create devices with low ESR and high specific energy and power is shown by these characteristics. The n/p-type, or the configuration in which an n-doped polymer and a p-doped polymer are used as negative and positive electrodes, is the most promising polymer supercapacitor configuration in terms of charge storage capacity and cell voltage and is capable of outperforming the double-layer carbon supercapacitors. However, this setup is not straightforward to implement, and the n-doping procedure presents the biggest challenges. The n- and p-dopingundoping process potentials of the polymer electrodes determine the cell potential range where the charge-discharge operations of polymer-based supercapacitors take place [34].

Since there are no structural abnormalities, like phase changes, during the charge/discharge operation, CPs may hold the charge in its entirety. Because of their greater surface areas and ability to store redox energy as a result, CPs can provide a higher capacitance [35]. Because they have a greater specific capacitance and a quicker rate of redox transfer, conducting polymers such as polypyrrole, polythiophene, and polyaniline have been employed extensively in pseudo-capacitor resources. PANI was singled out as the material that was most advantageous among them due to its simple synthesis, novel doping chemistry, fascinating electroactivity, high conductivity, specific capacitance, low cost, and relatively high conservational stability [36].

CPs are organic polymer electrode materials that exhibit better conductivity, capacitance, and low equivalent series resistance than conventional polymers. The quick-reversible redox processes from the -conjugated polymer chains give rise to the particular capacitances in CPs [35], in this scenario, the ions travel to the backbone of the polymer by the oxidation process(doping), and back into the electrolyte solution during the reduction step, also known as de-doping. Nevertheless, the redox reactions in conducting polymers result in mechanical stress, which limits stability and accelerates degradation via several charge-discharge cycles [37]. The low power densities in CPs, which result from the slow ion diffusion rates in bulk, are one of the key drawbacks that impair their performance. Prior research indicated that the previous capacitance of the PPy-based electrode began to fall by 50% merely after 1000 cycles. Accordingly, after 1000 cycles, the capacitance of PANI nanorods had lost roughly 29.5% of its value. Therefore, low cycling stability is the fundamental issue with CP-based electrodes [38].

There are many ways to synthesize CPs, but the one that is most frequently employed is the oxidation of monomers using chemical or electrochemical processes [39]. The fabricated polymers are in 2 or 3 general states. The "p-doped"(oxidized) state, as opposed to the "n-doped"(reduced) state, dominates in newly produced polymers. The polymer backbone is positively charged and gives a high level of electronic conductivity when it is in the p-doped condition. Due to their stable performances, oxidizable polymers are currently receiving more recognition from researchers than non-redox polymers [35].

Supercapacitor electrodes are a good fit for conducting polymer hydrogels. There are various methods for creating polymer hydrogels, such as (i) in-situ polymerization of monomers within the insulating polymer matrix, and (ii) adding crosslinkers during the polymerization process to facilitate the gel formation. However, while the final CP hydrogels produced using the first technique frequently exhibit good mechanical properties, their electrochemical properties fall short of expectations. The second technique has produced CP hydrogels that exhibit good electrochemical behavior. However, it is challenging to manufacture and fabricate a unique hydrogel with good mechanical performance. Additionally, it is strenuous to create a polymer hydrogel electrolyte with good electronic conductivity and acceptable capacitive performance.

2.4.3. Metal Oxides

Metal oxides are more chemically stable than conductive polymers and have a greater specific capacitance between 100-2000 F g-1, and higher energy density compared to carbon materials [40].In general, metal oxides can offer supercapacitors a significantly higher energy density than traditional carbon materials, as well as superior electrochemical stability over polymer materials. They show how ions electrodes and materials at the proper potential can react electrochemically to produce faradaic reactions and store energy in the form of electrostatic carbon material. Thus far, efforts have been made to improve the wettability and capacitive performance of carbonaceous materials through chemical surface changes.

Depositing metal oxide/hydroxide particles is a dependable method for improving the specific capacitance of electrodes. The metal oxide/hydroxide, which can be either of the following: ruthenium oxide, manganese oxide, cobalt oxide, nickel oxide, or mixed metals, is essential for improving electrode capacitance via the fast faradaic pseudocapacitance effects. The increase in electrode electrical conductivity is a critical component in promoting the capacitive effects of metal-based carbon capacitors.

To date, various transition metal oxides (Co_3O_4, NiO, $NiCo_2O_4$, MnO_2, $NiCo_2S_4$, $NiMoO_4$& Mn_3O_4) have been widely used as electrode materials (Hou et al., 2020). Because of its extremely high theoretical specific capacitance (1380 F g-1), inexpensive price, wide operating potential window in mild electrolytes, nontoxicity, and environmental friendliness, MnO_2 is one of the best options among them. Metal oxides however suffer from low specific capacitance and rate capability since their actual application is hindered by; Poor electrical conductivity, Slow ionic transport rate, and difficult solubility in electrolytes.

Despite their many advantages, employing these materials separately presents several difficulties, such as low specific capacitance, poor CP stability over repeated cycles, and poor conductivity in metal oxides. Scientists advise combining these materials into composites to address these issues. Some advantages of this method include improving the capacitance and stability of composite electrodes.

For the production of composite electrodes, there are two approaches: electrochemical methods and chemical methods that proceed through in situ synthesis. The advantages of electrochemical synthesis include controllable processes, the ability to monitor polymer mass, and reproducibility. In a study to examine the functionality of poly pyrrole/manganese oxide nanowires (Ppy/NwMnO$_2$) made electrochemically, the specific capacitance of Ppy and Ppy/NwMnO$_2$ was calculated as 109 and 203 F/g, respectively [36].

2.5. Composite Materials as Electrode Material for Supercapacitors

Transition metal oxides (TMOs), conductive polymers, and carbon-based compounds can be used as electrode materials. Because of their great chemical stability, mechanical, and electrical characteristics, and large surface areas, several carbon materials, including carbon nanotubes (CNT), graphite nanofibers (GNF), carbon black, and graphite, offer alternatives for carbon support for fillers and electrodes for polymer composites.

Because of their great graphitic structure, high specific surface area and electric conductivity, vapor-grown graphite nanofibers (GNFs) have been investigated for usage as adsorbents, electrode materials, and hydrogen storage devices. Furthermore, GNFs are intriguing potential materials to aid metallic nanoparticles by improving the electrochemical characteristics and electrocatalytic activity of the graphene nano fiber-based electrode. The observed increased electrocatalytic activity is thought to be caused by the good electrical conductivity of GNF and the way the metal nanoparticles are oriented on the GNF. In contrast to the performance of monolithic polymers, Carbon-based materials have been used to reinforce conductive polymer nanocomposites, which has garnered a lot of attention due to the synergistic effect it has on enhancing their electrical and mechanical properties. This is achieved through the interaction of the two components. For example, carbon nanotubes (CNTs) or graphene/CP nanocomposites have been studied for their potential use as sensors, supercapacitors, batteries, and more.

In general, EDLC electrode materials are fashioned from carbon-based substances due to their remarkable attributes. These materials boast a substantial specific surface area, adaptable pore size distribution, and outstanding electrical conductivity. Although carbon materials can provide remarkable power densities, their energy densities may be subpar due to EDLCs' storage mechanism, which limits overall performance[41]. Many carbon-based materials have been investigated as potential electrode materials, including graphene, carbon nanotubes, and carbon nanofibers. However, the low specific capacitance of carbon materials constrains the capacity of EDLCs, and the expensive cost of those carbon-based materials restricts the applications of those materials [42].

Conducive polymers have good conductive and pseudocapacitive qualities, but their stability is low, making them quickly slide off the substrate [43].TMOs are more chemically stable than conductive polymers and have a greater specific capacitance (100-2000 F g1), and higher energy density than carbon materials [44]. RuO_2 is regarded as the ideal pseudocapacitive electrode material due to its high theoretical capacitance and quick Faraday redox reaction [45]. However, its high cost and environmental toxicity substantially impede its use in supercapacitors [46]. Co_3O_4, MnO_2, and ZnO are possible alternatives to RuO_2 because of their advantages of being abundant in nature and having a high specific capacitance [47]. However, low electrical conductivity is a disadvantage shown by many transition metal oxide electrodes[48].

Ternary metal oxides, such as AB_2O_4 (A or B = Ni, Co, Mo, Mn, and so on), exhibit more active reaction sites and better electrical conductivity than binary metal oxides because of the coexistence of two metal ions and the synergistic effects of elements [49]. Because of their low cost, increased electrochemical activity, and availability as a naturally plentiful resource, metal molybdates (AMoO4, A = Ni, Mn, Co, etc.) and spinel cobaltates (XCo_2O_4, X could represent Ni, Cu, Zn, Mn, and so on) have also attracted a lot of scientific interest. A composite material made of metal oxide and rGO conducting polymer ($rGO/PANI/MnO_2$) was previously created, and it displayed a maximum specific capacitance of 592 F/g at 1 A/g current density, which corresponds to excessive specific energy and specific power (66.6 Wh/kg and 1800 W/kg, respectively) [36].

MnO_2 has received the bulk of the study's attention when it comes to metallic oxides. The most competitive transition metal oxide has been extensively researched to be MnO_2, which is widely available, has no environmental degradation, and has a great theoretical specific capacitance of about 1380 F /g [50]. However, due to its low conductivity and slow ion transport rate, its employment in supercapacitors is severely hampered [51].To overcome this restriction, carbonaceous materials having large surface areas and high electrical conductivity, such as graphene, may be utilized as scaffolds for the deposition of MnO_2 nanostructures [52]. The interaction proximity between electrolytes and electrode materials is improved and a large surface area with a large number of active sites is given, both of which improve electrochemical characteristics [53].

Graphenated CNTs are joined to create porous structures that act as an efficient electronic channel. MnO_2 nanoparticles are evenly dispersed on the surface. Additionally, the special composition of MnO_2nanosheets@graphene incorporated CNTs composites reduces the distance traveled by ions, fosters the transfer of charges, and speeds up reversible reduction-oxidation reactions, all of which enhance capacitance performance. The highest power density is 0.4 kW /kg (200 W /cm2) and an energy density of 51.2 W h /kg is reached. Combining the chemical vapor deposition (CVD) and hydrothermal methods, a 3D graphene/MnO_2 foam composite was created. The research demonstrates that 3D-graphene/MnO_2 composite electrodes have outstanding cycle stability and a specific capacitance of 333.4 F /g recorded at a current density of 0.2 A/ g [54].

2.6. Synthesis Methods for Preparation of Conducting Polymers, Carbon-based, Metal oxides, and composite materials

CPs are classified as the cationic and anionic salts of highly conjugated polymers. While chemical oxidation and electrochemical polymerization are used to create the cation salts, electrochemical reduction or chemical reduction employing reagents like sodium naphthalide is also an option for creating the anion salts of highly conjugated polymers. The backbone of an oxidized conducting polymer loses electrons, producing a cationic radical. On the other hand, an anionic radical is produced when electrons are introduced to the backbone of a decreased conducting polymer. But compared to its cation counterpart, this reduced conducting polymer is far less stable.

Chemical and electrochemical polymerization are the two main synthetic processes used to create conducting polymers. For mass production, chemical oxidation polymerization has been preferred but to keep the environment clean and safe, it is vital to limit by-products and waste materials [55]. Aromatic, benzoid (such as aniline) or nonbenzoid (such as 1-aminoanthracene), and heterocyclic compounds (such as pyrrole, and thiophene) can all be polymerized using electrochemical techniques [56].

Chemical polymerization is a typical technique used to create conducting polymers in large quantities, such as polyaniline, and polypyrrole [57]. This method involves either condensation polymerization essentially referred to as addition polymerization or step-growth mechanism which is a chain-growth mechanism [44]. In this case, the dopant acid is used to dissolve the monomer. For 4-5 hours, the mixture is continuously stirred as the oxidant, dissolved in the suitable solvent (water is frequently used), is added drop by drop. The precipitate that results is then filtered, washed, and dried. The major advantage of chemical synthesis is that it not only allows for a variety of methods to create various CPs but also makes it possible to produce these materials in massive quantities, something that is currently not conceivable with electrochemical synthesis. Additionally, there are more alternatives for covalent alteration of the CP backbone using chemical synthesis techniques.

Electrochemical synthesis is a comparatively simple synthetic method for creating CPs, which can be done using either constant current, constant potential or potentiodynamic procedures. Due to their conductivity characteristics, all conducting polymers can be polymerized electrochemically [58]. Typically, a three-electrode setup (working, counter, and reference electrodes) is used for electrochemical polymerization in a solution made up of a monomer, an electrolyte, and suitable additives. The electrolyte, time for deposition or method (continuous vs. pulsed), and applied potential are a few essential aspects that must be considered. All of these factors affect the mechanical, conductivity, and film morphology of the material, which directly affects how useful it is for various applications. Small films or coated electrodes can be prepared and characterized via electrochemical synthesis, which is versatile concerning the dopant that can be introduced from the electrolyte[59].

Electrochemical oxidation has a variety of benefits over chemical oxidation, including the flexibility to incorporate different dopants, simple control of the microstructures, sequential deposition to create stacked structures, and the capacity to create copolymers. An anodic potential is used to oxidize the monomer at the electrode surface after it has been dissolved in a solution containing a dopant. Both the electrolyte and the solvent must be stable at the oxidation potential. Typically, big potential window organic solvents like acetonitrile are used[60].PDMA(*Figure 8*) was created using a common chemical polymerization process [61]. Similarly, metallic oxides can be synthesized chemically or electrochemically with suitable solvents and electrolytes respectively [62].

Carbon materials such as graphene, carbon nanotubes, etc. can be synthesized both electrochemically and chemically by use of appropriate reagents and solvents. Reduced graphene oxide has widely been successfully synthesized by the Modified Hummers method (*Figure 7*). Composite electrode materials can be synthesized either via in situ polymerization by dispersing metal oxides and carbon materials in the polymer matrix, or by ex-situ where all the electrode materials are individually synthesized and then composite materials are prepared by mixing the materials in suitable solvents, appropriate temperatures usually about 373K and enough time and stirring for composite formation ranging from 4 hours to 12 hours depending on the temperature used. The composite product is then filtered and washed thoroughly with an acid of choice to remove unreacted components and oligomers and with distilled water before drying in an oven for 12 hours. The dry products are crushed into powder by use of a motor and pestle, weighed, and stored in glass storage vials for further analysis for electrochemistry performance as well as physicochemical characterization. In this particular work, In situ polymerization was employed to synthesize the composite materials (MnO_2/PDMA) and (rGO/MnO_2/PDMA) [42].

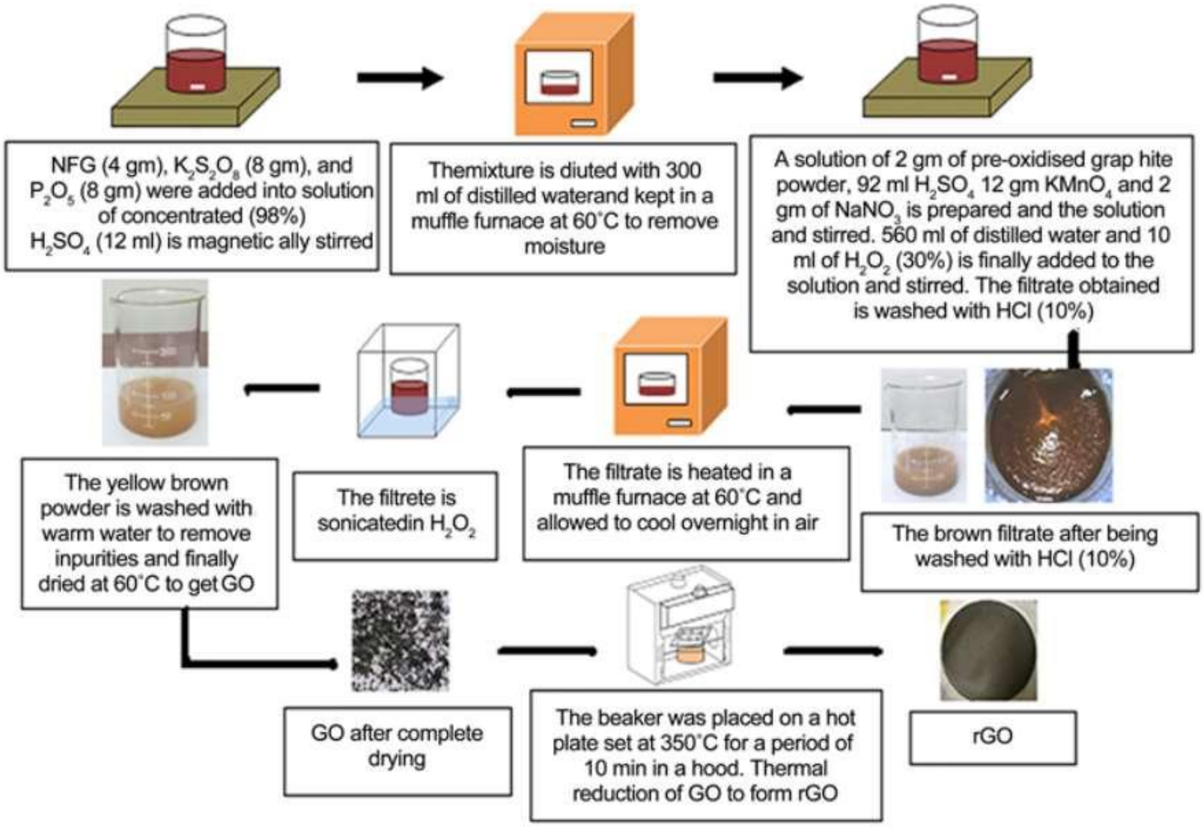

NFG (4 gm), $K_2S_2O_8$ (8 gm), and P_2O_5 (8 gm) were added into solution of concentrated (98%) H_2SO_4 (12 ml) is magnetic ally stirred

Themixture is diuted with 300 ml of distilled waterand kept in a muffle furnace at 60˚C to remove moisture

A solution of 2 gm of pre-oxidised grap hite powder, 92 ml H_2SO_4 12 gm $KMnO_4$ and 2 gm of $NaNO_3$ is prepared and the solution and stirred. 560 ml of distilled water and 10 ml of H_2O_2 (30%) is finally added to the solution and stirred. The filtrate obtained is washed with HCl (10%)

The brown filtrate after being washed with HCl (10%)

The filtrate is heated in a muffle furnace at 60˚C and allowed to cool overnight in air

The filtrete is sonicatedin H_2O_2

The yellow brown powder is washed with warm water to remove inpurities and finally dried at 60˚C to get GO

GO after complete drying

The beaker was placed on a hot plate set at 350˚C for a period of 10 min in a hood. Thermal reduction of GO to form rGO

rGO

Figure 7. The Steps followed for the synthesis of GO and rGO[63]

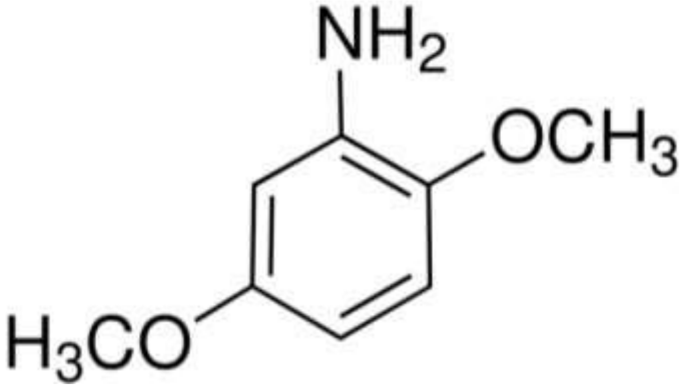

Figure 8. Chemical structure of 2,5-dimethylaniline

2.7. Assembly of Electrodes

Supercapacitors are divided into three categories based on the electrode configurations: symmetric, asymmetric, and battery-type supercapacitors. Whereas an asymmetric supercapacitor employs two distinct materials for electrodes, a symmetric supercapacitor uses two electrodes that are comparable to one another. Because of their higher energy densities, the third form of hybrid supercapacitor, referred to as a battery-type hybrid supercapacitor, also garnered a lot of research attention. It employs a battery electrode and a supercapacitor electrode. Because metal ions, like lithium and sodium ions, are intercalated within the electrode nanostructure for charge storage, a high energy density is achieved.

When compared to ordinary supercapacitor electrodes, battery-type hybrid supercapacitors offer promising options for long-lasting power supply. However, a significant challenge is maintaining the balance of charge between the two electrodes. They can link batteries and supercapacitors. In battery-type solar cells, graphite is employed as the positive electrode and lithium-ion doped graphite as the negative electrode. Compared to EDLC, this structure increases the energy density by a factor of two to three due to its higher kinetics. However, it has been found that asymmetric electrode orientation performs better than symmetric configuration[64].

2.7.1. Symmetric Assembly of Electrodes

The +ve and -ve electrodes of symmetric SCs are composed of the same electrode material. Compared to normal SCs, it has a high energy density and great stability for the potential window. Selecting the appropriate electrolyte and electrode materials is crucial since the same electrode material has benefited but has reached high energy density in symmetric SC. Because of their remarkable and unique properties, the majority of materials, such as metals, metal oxides, graphene, activated carbon, carbon nanoparticles, conductive polymers, and composite materials, have already been used as electrode materials in supercapacitors (SCs). The same electrode material, which can be either carbonaceous, metal oxide/hydroxide, conductive polymer, or a mix of any of the aforementioned electrode materials, makes up the working and counter electrodes of a symmetric supercapacitor electrode assembly. Chen et al. grew α-Fe2O3 on a conductive carbon substrate to create an aqueous symmetric supercapacitor. With 2 M Li2SO4 and a high operating voltage of 2.0 V, it has produced an energy density of 11 mWh cm−3 and a power density of 1543.7 mW cm−3. At a current density of 20.0 mA cm−2, the capacitance retention was 83.08% after 5000 cycles [79]. Khattak et al. recently created a solid-state symmetric supercapacitor utilizing an aerogel hybrid electrode of α-Fe_2O_3/graphene. Fe_2O_3/graphene aerogel was created for this via an in situ hydrothermal process. Using a three-electrode system, the electrochemical properties of Fe_2O_3/graphene aerogel were first investigated[65]. Redox peaks were well characterized and correlated with the Fe2+ → Fe3+ redox processes. A great specific capacitance of 1045.3 F/g was achieved at 0.4 A/g current density. To study the possibilities of Fe_2O_3/graphene aerogel, a PVA-KOH gel electrolyte was placed between the two electrodes to form a symmetric supercapacitor. The aerogel was coated over nickel foam. The symmetric device generated an energy density of 9.8 Wh kg−1 and a power density of 90.1 W kg−1 within the cell voltage range of 0–0.8 V. Furthermore, the device's exceptional flexibility and stability were proved by its electrochemical performance under varying bending conditions (90 and 180°). Park et al. have also developed a solid-state symmetric supercapacitor with a composite α-Fe_2O_3/poly(3,4-ethylenedioxythiophene) (PEDOT) anode material. Initially, hierarchical core-shell type Fe_2O_3/PEDOT nanoparticles were prepared using vapor deposition polymerization, liquid-liquid diffusion-assisted crystallization, and sonochemical techniques. The generated material had a high surface area (376.4 m2 g−1), conductivity (120 S cm−1), and great capacitive capabilities. The solid-state symmetric supercapacitor was built using a hydrogel electrolyte based on H_2SO_4-PVA, with the positive and negative electrodes made of Fe_2O_3/PEDOT. The gadget worked and produced good energy and power densities of 252.8 F/g, 136.3 Wh/ kg, and 10,526 W kg−1 up to 2.0 V. Additionally, it showed a high Csp [66].

2.7.2. Asymmetric Assembly of Electrodes

Since the two electrodes in asymmetric SCs are composed of distinct materials, we refer to them as asymmetric hybrid SCs. Research interest has increased since one electrode in this hybrid SC is formed of carbon-based material, while the other electrode is constructed of different electrode materials, such as conducting polymers, metal oxide/hydroxide, or composite materials. Since using conducting polymer, metal oxide, or composite material for the negatively charged electrode is bad because it reduces the efficiency in pseudocapacitors, this issue is lessened if the negative electrode is made of carbon-based material and the positive electrode is made of other materials[67].In particular, the carbon-based material used as the cathode in asymmetric hybrid solar cells with two dissimilar electrodes provides the power density, while other materials such as metal oxide or conductive polymers used as the anode provide the energy density. This type of SC aims to fuse the best aspects of EDLC with pseudocapacitors. Additionally, composite hybrid SCs use composite electrodes made of metal oxide and carbon. The charge is held by the metal oxide, and the charge carrier can pass through the carbon. The conductivity of this hybrid composite SC is determined by the components' composition. Here, the capacitance value is mostly dependent on the material's pore diameter.

By utilizing several kinds of electrodes, the voltage of the cell could be raised to 2.0 V. Qu et al., for instance, built AC/MnO_2 nanorod ASCs using K_2SO_4 as the electrolyte, and after 23 000 cycles, the capacitors showed impressive cycling stability in the range 0 and 1.8 V with a capacitance loss of less than 6%. Shi et al. created flexible ASCs with graphene serving as the anode and ultrathin MnO_2 nanosheets serving as the cathode. After 10,000 cycles, a high Ed (97.2 Wh kg−1) and 774 F g−1 capacitance were retained. In actuality, the size and shape of the electrodes have a significant influence on their electrochemical performance. Jiang presented the synthesis of ultrathin porous MnO_2 nanoflowers, exhibiting a pore size distribution centered at around 3.6 nm and a huge specific surface area of 595 m^2 g−1. The authors claim that the porous architectures and ultrathin nanosheets promote ion dispersion and transportation, which results in improved electrochemical characteristics. When compared to MnO_2/MnO_2 and FMCNTs/FMCNT symmetric SCs, the as-assembled MnO_2 functional mesoporous carbon nanotubes SCs showed a higher Ed. This was likely because of the high operating potential range in aqueous electrolytes (0-2.0 V) and the synergy of two mesoporous electrodes[68].

Combining MnO_2 with other conductive materials, such as carbon compounds or conductive polymers, can also increase the electrochemical performance of MnO_2-based ASCs by increasing its conductivity and power capacity. For instance, Xia and Huo reported using a hydrothermal technique to generate a MnO_2/CNT nanocomposite. By combining the MnO_2/CNT nanocomposite (cathode) with AC as the anode, the asymmetrically assembled MnO_2/CNT/AC demonstrated exceptional cycle stability and a high Energy density of 23 Wh kg−1 and Power density of 330 W kg−1. An ASC based on a nitrogen-doped p-BC (p-BC/N) anode and nanofiber-coated MnO_2 (p-

BC@ MnO_2) cathode made of 3D bacterial cellulose (BC) pellicles was produced by Chen et al. On the one hand, the p-BC functioned as a matrix to quicken the movement of ions and electrons. Conversely, the MnO_2 that was attached offered a substantial specific surface area that facilitated quick redox reactions. As a result, the ASCs produced a maximum Pd of 284.63 kW kg−1 and a reasonably high Ed of 32.91 Wh kg−1. Additionally, it demonstrated a high degree of cycling performance, demonstrating 95.4% of the previous specific capacitance after 2000 cycles. Huang et al. produced and used a CuO@ MnO_2 core-shell structure as a cathode. The CuO@MnO_2//MEGO ASCs were built in 1.0 m Na_2SO_4 aqueous electrolyte by using microwave-exfoliated graphite oxide (MEGO) as the anode. It has a 1.8 V potential range for reversible charging and discharging. The most significant results were high Energy and power densities of 22.1 Wh kg−1, and 85.6 kW respectively, and capacitance retention of 101.5% after 10,000 cycles.

Tao et al. reported on the fabrication of a flexible ASC made of carbon cloth (CC) anode and activated carbon (AC) cathode made of polypyrrole (PPy)–MnO_2. Because of CC's superior flexibility and conductivity, it was used as both the substrate and collector. The microstructure having PPy-wrapped MnO_2 uniformly adorned on carbon cloth was visible on the PPy–MnO2–CC anode. In addition to providing corrosion protection for MnO_2, the PPy wrap enhanced conductivity and flexibility throughout the charge/discharge process. Having a high Energy density of 8.67 mWh cm−3 and capacity retention of 98.6% after 1000 cycles, this device demonstrated remarkable electrochemical capabilities based on the synergistic impact of outstanding pseudocapacitive performance arising from MnO_2 and PPy. Guo et al. used a DNA-assisted technique to create a CNT@DNA-MnO_2/CNT@DNA ASC that registered an Energy density of 11.6 Wh kg−1[68].

Chapter Three

Methodology

3. Materials

Chemicals: From **Adrich;** Graphite powder-99.9%, 2,5-dimethoxyanaline-98%, and MnO_2-70%

CARLO ERBA Reagents; H_2SO_4-96%, P_2O_5-98%, HCL-37%

Neolab Life Science Co.; $K_2S_2O_8$-98.5%, $KMnO_4$-99.9%, Activated Carbon-99%

LOBA Chemie; APS-98%

UNI-CHEM; NaNO3-99%, and $AgNO_3$-99.9%

All the chemicals are of analytical grade standard.

Instrument: FTIR, XRD, SEM-EDS, BET, Electrochemical working station (GCD, CV, EIS software)

3.1. Synthesis Methods:

3.1.1. Synthesis of Reduced Graphene Oxide (rGO)

First GO was synthesized by the modified hummers method and then its thermal reduction to rGO follows.

A mixture was prepared by combining 4 grams of graphite powder, 12 ml of H_2SO_4, and 8 grams of P_2O_5. The solution was stirred using a magnetic stirrer for 6 hours. After that, 12 ml of H_2SO_4 was added to the filtrate along with 8 grams of $K_2S_2O_8$. The mixture was stirred using a magnetic stirrer for another 6 hours. The resulting mixture was cooled down to room temperature and then diluted with 300 ml of distilled water. The filtrate was dried overnight in air and then heated in a muffle furnace in the air at 60°C for 2 hours to remove any remaining moisture[63]. 2 grams of pre-oxidized graphite powder were added to a mixture of 92 ml of H_2SO_4 and 12 grams of $KMnO_4$, while continuously stirring in a water bath. After 15 minutes, 2 grams of $NaNO_3$ were added to the solution. The solution was then stirred at room temperature for 2 hours. Next, 200 ml of distilled water was added to the solution and stirred for 15 minutes. Following this, 10 ml of 30% H_2O_2 and 560 ml of distilled water were added to the solution. The filtrate obtained was washed with 10% HCl. The brown suspension obtained was heated in a muffle furnace for 30 minutes at 60˚C and then allowed to cool overnight in air. The brown dispersion was dialyzed extensively with distilled water for 1 week, to remove residual metallic ions and acids. Finally, the filtrate was air-dried overnight and sonicated for 5 hours with H_2O_2. The resulting yellow-brown residual powder was washed with warm water up to 3 times to remove impurities. The dry GO powder was obtained after heating the filtrate at 60˚C for 4 hours.

To obtain rGO from GO, 100 mg of the dried GO powder was taken in an empty beaker and covered with aluminum foil that had many punched pores. The beaker was placed on a hot plate set at 350˚C for 10 minutes in a hood. This thermal reduction process eliminates oxygen from GO, hence increasing its electrical conductivity and converting GO to rGO. The resulting black powder of rGO was collected from the beaker and weighed[63].

3.1.2. Synthesis of Poly(2,5-dimethoxyaniline) (PDMA)

There are two major synthesis methods for conducting polymers; the electrochemical method and the chemical synthesis method. The electrochemical synthesis method produces high-purity substances and it is easy to monitor the polymerization process. However, only small amounts of polymer can be produced at a time. Chemical synthesis produces higher amounts of samples at a time, and therefore this work utilized the chemical synthesis procedure for the synthesis of PDMA. Alternative acids such as sulphuric acid could also be used in place of HCl, but this work used HCl acid in the polymerization technique. APS can be replaced by hydrogen peroxide as the oxidizing agent in the chemical synthesis procedure of PDMA.

The PDMA was synthesized by a standard chemical polymerization method. In a 150ml conical flask,2g of 2,5-dimethoxy aniline was mixed with 50ml of 1M HCl and the solution cooled to 0-5^{0}C.To this, a prechilled solution of 5g ammonium persulfate (APS) dissolved in 50ml 1M HCl was added dropwise over 25 minutes under vigorous stirring. During the addition of ammonium persulfate solution, a deep blue color developed rapidly. This polymerization process was carried out up to 4 h. Subsequently, the solution was filtered and washed with double distilled water repeatedly to remove the impurities and finally washed with a 1MHCl solution to obtain a dark green precipitate. The precipitate was dried under a vacuum oven overnight at 80^0C, cooled, and crushed into a powder. The PDMA powder was stored in a desiccator at room temperature for later use [61].

3.1.3. Synthesis of MnO_2/PDMA Binary Composite

Composite materials could be realized by both in-situ and ex-situ polymerization techniques. The Ex-situ technique is a more physical technique that combines the individual electrode materials into a composite by physical stirring under elevated temperatures. The in-situ method usually utilizes chemical reactions to realize the composite materials. In-situ polymerization technique was used to synthesize all the composites of this work.

In a conical flask,2g of DMA was dissolved in 50ml 1M HCl and to it,8.7g of MnO_2 was added with constant stirring in an ice bath. A solution of 5g APS previously dissolved in 50ml 1M HCl was slowly added to the reaction mixture and the stirring continued under the same temperature conditions for 12 hours. The obtained mixture was then filtered in a Buchner funnel and washed thoroughly with distilled water and 1M HCl to remove the unreacted residues. The obtained product was dried overnight in an oven at 80^0C, cooled, powdered, weighed, and stored in a desiccator ready for use. This procedure was repeated for 4g (60%) and 1g (30%) amounts of MnO_2 to determine the effects of varying the amounts of MnO_2 on the electrochemical performance of the binary composite.

3.1.4. Synthesis of rGO/MnO_2/PDMA Ternary Composite

To synthesize this composite, 0.1g of the previously synthesized rGO was sonicated together with 8.7g of MnO_2 in 100ml of deionized water and this solution was added to a DMA solution made of 2g DMA dissolved in 50ml 1M HCl in an ice bath maintained at 0-5^0C with constant stirring. 5g of APS was then dissolved in 50 ml 1M HCl and the solution was added to the reaction mixture slowly with continued stirring. The stirring in these temperature conditions was continued for 12 hours and the resultant reaction mixture was filtered in a Buchner funnel, washed with distilled water, and 1M HCl. The product was dried overnight in a vacuum oven at 80^0C. The dried product was cooled and the powder was weighed and stored in a desiccator for future use. This procedure was repeated for 4g (60%) and 1g (30%) amounts of MnO_2 to determine the effects of varying the amounts of MnO_2 on the ternary composite electrochemical performance. The manganese dioxide amounts were varied according to literature, taking the percentages that have not yet been explored as discussed by S. Deng in his work ‘’Synthesis and electrochemical properties of MnO2 nanorods/graphene composites for supercapacitor applications’’[69]. *Figure 9* represents the experimental events undertaken in the laboratory from the synthesis to the characterization of the electrode materials.

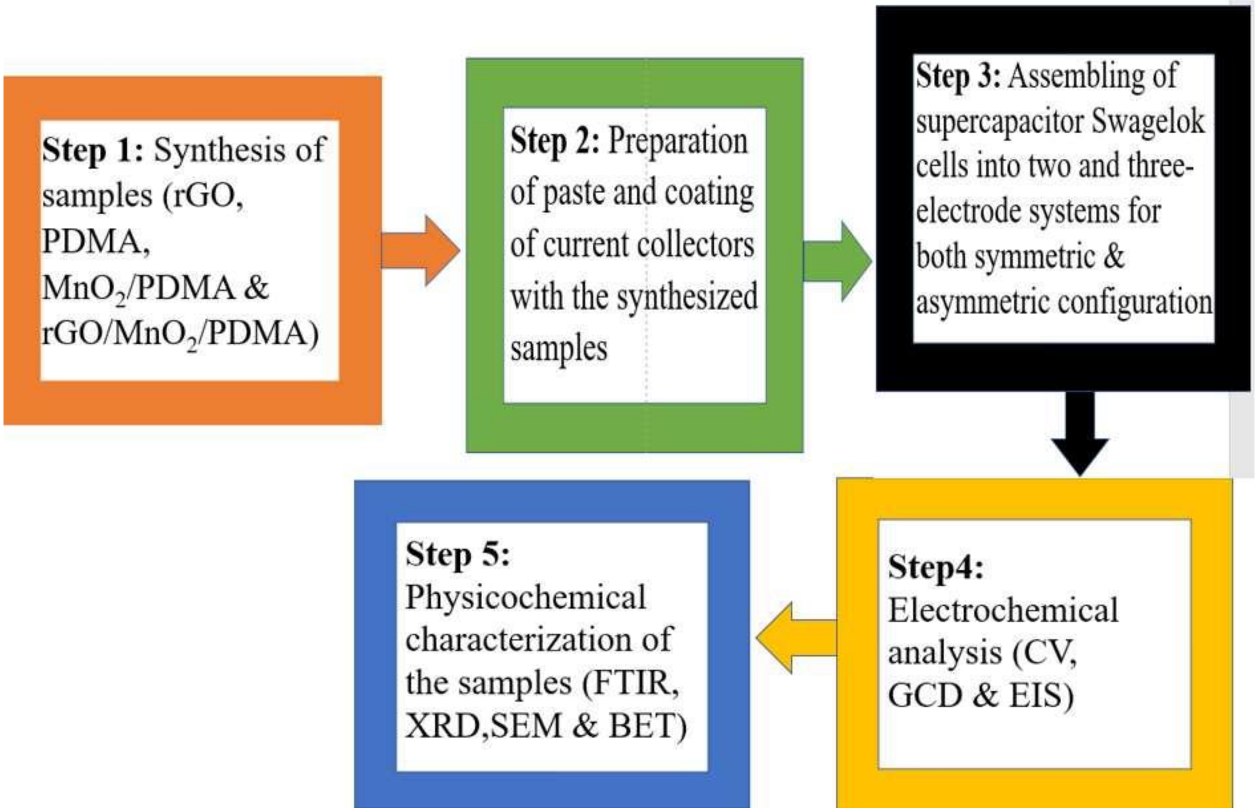

Figure 9. Systemic flow of activities from the synthesis of the electrode materials to their characterization

3.2. Characterization Methods

3.2.1. Physical Characterization Techniques

3.2.1.1. XRD characterization of synthesized samples

X-ray Diffraction Analysis (XRD) is a non-destructive method that is used in materials science to determine the crystallographic structure of a material. The technique works by exposing the material to X-rays and then measuring the intensity and scattering angle of the X-rays that leave the material. The primary use of XRD is to identify materials based on their diffraction pattern. In addition to phase identification, XRD also provides information on the actual structure of the material, including deviations from the ideal structure due to internal stresses and defects. XRD is widely applied to identify crystalline phases and orientation, determine structural properties such as lattice parameters, strain, grain size, Epitaxy, Phase composition, and preferred orientation, Measure the thickness of thin films and multi-layers, and determine atomic arrangement.

Crystals are regular arrays of atoms, whilst X-rays can be considered as waves of electromagnetic radiation. Crystal atoms scatter incident X-rays, primarily through interaction with the atoms' electrons. This phenomenon is known as elastic scattering; the electron is known as the scatterer. A regular array of scatterers produces a regular array of spherical waves.

X-rays are used to produce the diffraction pattern because their wavelength, λ, is often the same order of magnitude as the spacing, d, between the crystal planes (1-100 angstroms). The output is signal peaks in a graph of intensity vs Diffraction angle (2θ). The peak shape, peak position, peak width, and peak intensity are significant to the interpretation of results in XRD[70]. Every crystalline substance creates a unique pattern. Each substance in a mixture produces its pattern independently. Microstructure, quantitative resolution of chemical species, isomorphous substitutions, unknown crystalline materials, and solids are all identified, as well as crystal structure, crystallinity level, crystallite size, and atomic spacing. XRD spectrometry is employed in forensics, nanomaterials, catalysis, geochemical materials, composite materials, minerals, and pharmaceuticals because it produces independent patterns of components in mixes. Crystals give sharp peaks because they have a regular arrangement of atoms while amorphous solids do not possess any regular interior arrangement of atoms like in glass. The XRD data results can be matched with the existing Joint Committee on Powder Diffraction Standards (JCPDS) files to find the crystal system of the material you have used for your experiment. Additional peaks can be indicative of composite material and increased crystallinity[69].

According to Mosley's law, every element has its unique signature in the form of Kα emission. As seen before, electromagnetic radiation can be diffracted by atomic planes only when half of its wavelength is less than the inter-atomic distance(D) as illustrated by equation 5;

$$\frac{\lambda}{2} \leq D \qquad (5)$$

The Bragg's law is a consequence of constructive interference and is given by:

$$2d \sin\theta = n\lambda \qquad (6)$$

Where d is the interplanar spacing, λ is the wavelength, n is an integer and θ is the angle of reflection. From an XRD data, a crystallite size can be calculated using the Scherrer's formula;

$$d = K\frac{\lambda}{\beta\cos\theta} \qquad (7)$$

Where d is the diameter of the crystallite, K is a constant that depends on the shape of the crystallite, usually 0.9, λ is the wavelength and β is the full width at half maximum peak (FWHM). Small crystallite size and lattice strain cause peak broadening[71].In this work, XRD was used to identify the crystallinity of the synthesized materials.

3.2.1.2. SEM Characterization of Synthesized Samples

A Scanning Electron Microscope produces images of a sample by scanning it with a focused beam of electrons. The image consists of the variation as a function of the probe position, of some signal generated by the sample under the probe. The interaction of the electrons with the atoms of the sample produces various signals which contain information about the surface topography of the sample and also about the composition of the sample. Among the signals produced are secondary electrons (SE), Backscattered electrons (BSE), Photons of characteristic X-rays, Absorbed current, and transmitted electrons.

The specimen in SEM should be completely dry. The sample can be solid or bulk specimens of any size that will fit within the specimen chamber. Specimens can be studied in low vacuum, high vacuum, and at a wide range of very low or elevated temperatures. Both conductive and non -

conductive samples can be studied with the help of SEM and a resolution better than 1nm can be achieved. A very narrow electron beam used in SEM results in a large depth of field of scanning electron microscope micrographs. SEM combines the ease of operation of an optical microscope and the analysis capacities of TEM.

In a typical SEM, an electron beam is thermionically emitted from an electron gun fitted with a tungsten filament cathode. This cathode is electrically heated for the emission of electrons. The low energy (0.2 keV to 40 keV) electron beam is focused by one or two condenser lenses to a spot of 0.4nm to 5nm in diameter. This focused beam of electrons is then passed through a system of magnetic lenses used for the deflection of the beam in the x and y directions. Thus, a rectangular area of the surface of the sample is scanned by the electron beam. To see the surface structures and assess the variations on the surface, SEM material sciences and surface sciences are magnified numerous times. The resulting image is a distribution map of the intensity of the signal emitted from the scanned area. The energy exchange between the electron beam and the specimen gives rise to the reflection of high-energy electrons by elastic scattering, the emission of secondary electrons by inelastic scattering, and the emission of electromagnetic radiation[72].

3.2.1.3. FTIR Characterization of Synthesized Samples

FTIR Analysis, also known as FTIR Spectroscopy, is an analytical technique used to identify organic, polymeric, and sometimes inorganic materials. This method involves using infrared light to scan test samples and observe their chemical properties. The FTIR instrument sends infrared radiation, ranging from 10,000 to 100 cm-1, through a sample. The sample molecules absorb some radiation, converting it into rotational and/or vibrational energy, while some radiation passes through. The resulting signal at the detector presents as a spectrum, typically ranging from 4000 cm-1 to 400 cm-1, that represents a molecular fingerprint of the sample. Each molecule or chemical structure produces a unique spectral fingerprint, making FTIR analysis a great tool for chemical identification. Band identification can help identify the molecules that make up a substance since the absorption bands are connected to the vibrations of specific functional groups inside the molecule.

FTIR spectroscopy is a well-established technique used in the evaluation of industrially manufactured materials for quality control. In the process of material analysis, it is frequently the initial stage. A shift in the distinctive absorption band pattern denotes the existence of contamination or a change in the material's composition. FTIR microanalysis is usually used to identify the source of abnormalities that are detected by visual inspection. This method works well for analyzing the chemical makeup of larger surface regions as well as tiny particles, usually 10–50 microns. It is employed in failure analysis investigations to identify oxidation, decomposition, or uncured monomers; to identify and characterize unknown materials such as films, solids, powders, or liquids; to identify contamination on or in a material such as particles, fibers, powders, or liquids; and to identify additives following extraction from a polymer matrix.

On the FTIR bench, a micro-ATR accessory is utilized to focus the beam on a single-bounce attenuated total reflectance (ATR) crystal to target small areas of interest. We can place the sample such that it is near the ATR crystal thanks to the optical viewing capabilities provided by the ATR cell. The irradiating area takes up around 0.2 mm of diameter. We shift the analysis to a microscopic FTIR instrument, which offers positioning resolution on the order of 10 microns in diameter when precise positioning is needed to define a sample area, layer, or micro-fine particle. Using tiny optics in conjunction with the focused infrared beam, we can introduce an ATR probe directly at the area of interest with the help of the microscopic FTIR in the reflectance. Additionally, we can spatially resolve differential chemistry in a very tiny area using this approach[73].

The FTIR spectrum is a plot of Transmittance (ordinate) vs. wavenumber (abscissa). The left side of the spectrum is the functional group region, also known as the diagnostic region while the right side of the spectrum after 1500 cm-1 is the fingerprint region. The peaks look downwards rather than upwards. *Table 1* below is very important when interpreting the spectrum to get meaningful functional group information on the sample material from the peaks.

Table 1IR correlation of functional groups with wavelength[74]

Functional group	Wavenumber(cm-1)
C-H	2850-3300
C=O	1680-1750
C=O*	1000-1300
O-H(alcohols)	3230-3550
O-H(acids)	2500-3300 (very broad peak)

3.2.1.4. BET Characterization of Synthesized Samples

The BET method is utilized to determine the surface area of porous materials (micro, meso, and macroporous). This measurement is crucial in understanding the physical structure of the material since the surface area influences how the solid will relate to its surroundings. Various characteristics, including catalytic activity, moisture retention, dissolution rates, and shelf life, are often linked to the surface area of the material. Surface area analysis is among the most essential methods used in material analysis, and it is critical in the design and production of solids. The surface area can be adjusted during both the synthesis and processing of the material[75]. As particles are broken down into smaller pieces through milling, their surface area increases due to the creation of additional surfaces. Similarly, the formation of pores within particles through processes like dissolution and decomposition also increases surface area. This effect is particularly pronounced in materials characterized by many narrow pores, like activated carbons, which can have specific surface areas exceeding 2,000 m2/g.

To determine the true or specific surface area of a particle at the atomic level, the BET theory utilizes the adsorption of an inert gas. Since gases and solids interact weakly, a cryogenic liquid must be used to cool the solid samples to stabilize the process. The solid sample's temperature is held constant while the concentration or pressure of the adsorbing gas is increased, generating a surface area isotherm. This is a plot of the relative pressure of the gas on the x-axis and the volume of the gas adsorbed on the y-axis. As the relative pressure increases, more gas molecules adsorb on the surface until a monolayer is achieved. By calculating the number of gas molecules in the monolayer, the area of the accessible surface can be calculated based on the known cross-sectional area of the adsorbate. The BET equation is used to calculate the surface area appropriately because gas adsorption as a function of pressure is not linear[76].

The BET equation was first developed in 1938 [76] and is still the widely used method to determine the number of molecules/atoms of a gas needed to form a monolayer, X_m, of adsorbed gas on a solid surface [77]. The BET equation (Equation 8) illustrates the relationship between the number of gas molecules adsorbed (X) at a given relative pressure (P/P_0), where C is a second parameter related to the heat of adsorption.

$$\frac{1}{X[(\frac{P_0}{P})-1]} = \frac{1}{X_m C} + \frac{C-1}{X_m C}\left(\frac{P}{P_0}\right) \qquad (8)$$

The BET equation strictly describes a linear plot of $1/[X(P_0/P)-1]$ vs. P/P_0 which for most solids, using nitrogen as the adsorbate, is restricted to a limited region of the adsorption isotherm, usually in the P/P_0 range of 0.05 to 0.35. The surface area, SA, is calculated from the slope and intercept according to Equation 9;

$$SA = \frac{1}{slope + intercept} \times CSA \qquad (9)$$

where CSA is the cross-sectional area of the adsorbate [75].

Gas adsorption is a useful technique for determining the surface area of solid materials. Knowing the surface area is important in various applications, including the manufacture and processing of carbon, catalysts, supercapacitors, pharmaceuticals, batteries, supercapacitors, ceramics, and minerals. For instance, the surface area of battery and supercapacitor components (i.e. anodes, cathodes, and separator membranes) can affect their performance, including characteristics such as charging and discharging rates, capacity, and impedance. The BET principle, which utilizes gas adsorption data, can be applied to porous and non-porous materials, irrespective of particle size and shape. Therefore, it is an essential tool for investigating and manufacturing a wide range of solids[78]. Porous materials are widely classified into six IUPAC classifications, groups I-III represent classifications of microporous materials, groups IV and V represent mesoporous materials, and group VI represents microporous materials. Mesoporous materials whose pore diameter ranges between 2-50nm are different from other porous materials because they present hysteresis loops in their adsorption/desorption curves, while the rest of the classifications have no hysteresis loops. *Figure 10* illustrates the different classifications of porous materials.

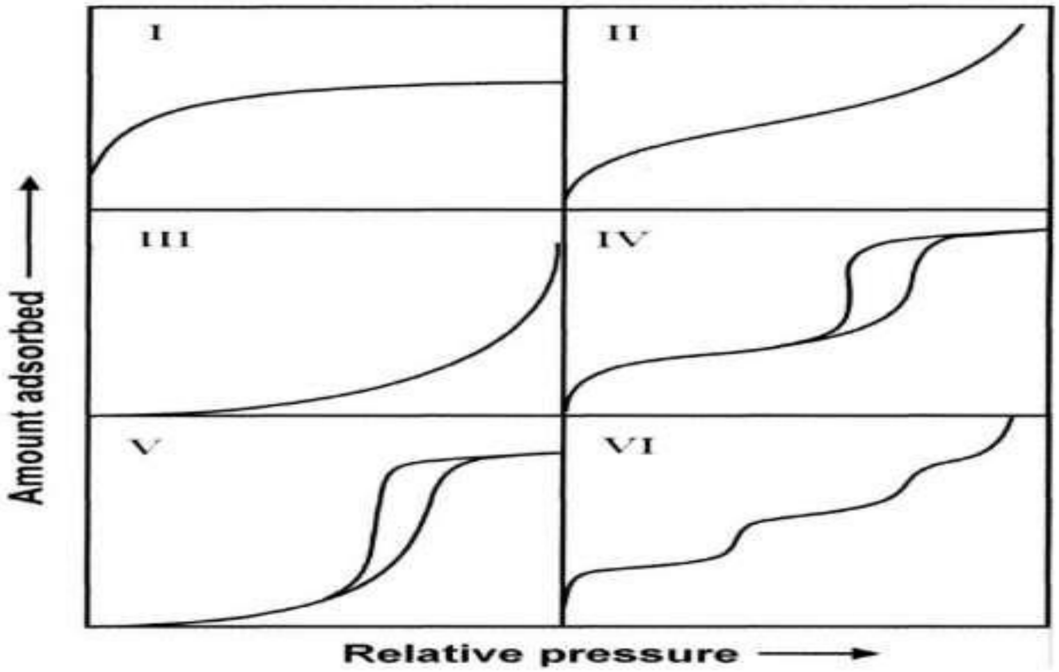

Figure 10. The IUPAC classification of adsorption/desorption isotherms of porous materials [79].

3.3. Preparation of Electrodes and Assembling of Devices

The silver current collector mesh was cut out, washed with water and acetone to remove impurities then vacuum-dried, cooled, weighed, and stored in a desiccator for later use. The measured amount of 80 wt% nanocomposite samples, 10 wt% activated carbon (as a conducting agent), and 10 wt% polytetrafluoroethylene (PTFE) (as a binder) was homogeneously mixed and pressed into a (1 cm × 1 cm) silver mesh current collector by applying pressure.

The sample-coated current collector was dried overnight in the oven and cooled and their weights were recorded to get the weight of the sample material. Swagelok cells were assembled asymmetrically in a Two-electrode system and a Three-electrode system with an activated carbon-coated current collector acting as the counter electrode with a slightly higher mass and the active material as the working electrode. Silver wire was used as the reference electrode in the 3-electrode system setup. *Figure 11* shows the steps used to prepare the paste and coating of the current collector and then assemble a two, and three-electrode system Swagelok cell. A two-electrode system only has the working and counter electrode but does not have a reference electrode like a three-electrode system. More information can be obtained from Appendix A2.

The electrochemical performance of the prepared electrode was tested by the traditional three-electrode system and two-electrode system. The electrochemical performance of the obtained electrode was tested on the electrochemical workstation using the Frequency Response Analyser (Fra) Version 4.9.007 serial number U3A71305 software for EIS analysis and General Purpose Electrochemical System (GPES) Version 4.9.007 software for both CV and GCD analysis[80].

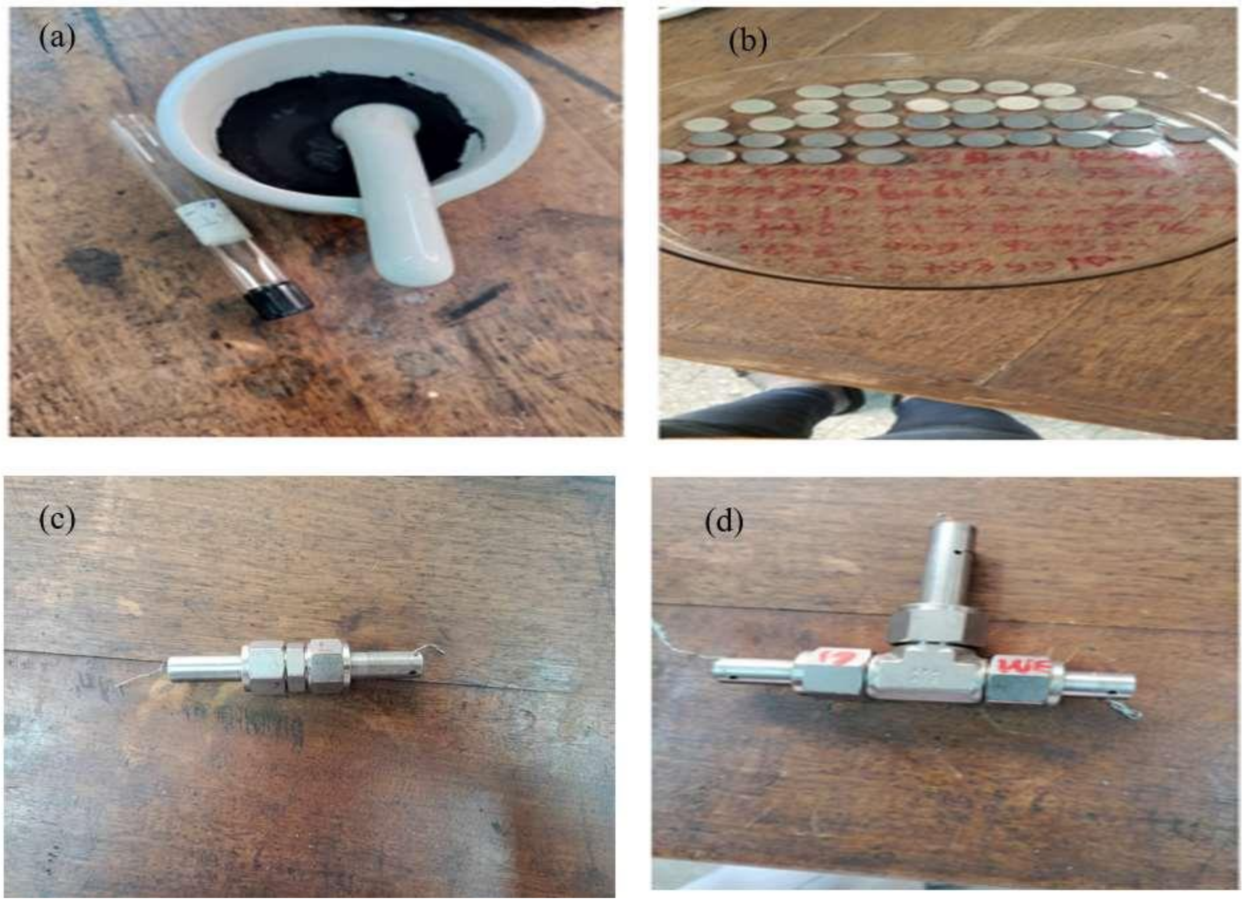

Figure 11. Preparation of paste (a), coating of current collectors with the paste, (b), and assembly of Swagelok cell into Two-electrode system (c), and Three-electrode system (d).

3.4. Electrochemical Studies

3.4.1. Cyclic Voltammetry (CV)

CV is an instrumental analytical method used to measure the current flowing through an electrochemical cell as the voltage cycles over a predetermined range, often at a defined pace. The resultant voltammogram, which is generally rectangular for a supercapacitor, is a plot of current vs voltage[81]. As a result, if the voltage is changed proportionally with time, the associated current also changes linearly, being positive when the voltage rises and negative when it falls. In practice, deviations from rectangularity will happen as a result of series resistance in the system, which may be connected to ion diffusion in the electrolyte, contacts between the electrode and the device's terminals, or electron transport in the electrode material. Consequently, the electrolyte has a major impact on internal resistance or ESR. The major benefit of employing an organic electrolyte is the highest achievable voltage. The organic electrolyte can assist in raising the unit cell's voltage above 2V. The typical voltage is between 2.5 and 2.7 V [39].

Conducting salts are dissolved in organic solvents to create organic electrolytes. Therefore, the composition of the dissolved salts and solvent, ionic size, conductivity, and purity factor all affect how well the organic electrolyte performs. The greatest voltage achieved is significantly influenced by the electrolyte's purity. As compared to organic electrolytes, aqueous electrolytes do not offer as high a voltage. The dissociation potential of water limits the highest voltage. However, aqueous electrolytes have been the most widely used for reporting an electrode's electrochemical properties.

The aqueous electrolytes have a lot of protons available, small ionic size, low resistance, and excellent conductivity. The electrolyte is the most popular option because it is affordable. Strong acid, strong alkaline, or neutral solutions are the most common aqueous electrolytes. Regardless of the type of electrode material, an acidic or alkaline electrolyte limits the potential window to 1V to 1.23V. On the other hand, the neutral aqueous can increase the potential window more than an acidic or alkaline electrolyte. Potentials as high as 1.6 V are frequently observed. Due to these resistances, two corners of the voltammogram are rounded off, with the rounding getting more evident with the sweep rate raise. This is because the current can’t react instantly to the the direction of the voltage sweep changes. The interfacial double layer won't get enough time to form at all at swift enough sweep rates, leading to insignificant capacitance. According to Fick’s Law mass transfer diffusion can be simplified to give the peak current as per equation 10,

$$I� = (2.69 \times 10^5)\,\overset{3}{�}����^{1/2}��^{1/2}� \qquad (10)$$

Here, (n) is the number of electrons obtained during the reduction, (S) is the working electrode's surface area in cm2, (DA) is the diffusion coefficient, (v) is the sweep rate, and (CA) is the amount of A in the bulk solution, expressed as a molar concentration. The CV data gives specific capacitance (Cp)of a material. The origin application is best used to plot and analyse CV data. A CV is a plot of current(A) on the ordinate vs potential (V) on the abscissa. In the resultant curve, the current changes by changing potential from v1 to v2.

Therefore, the specific capacitance of a material can be calculated using the formula bellow (equation 11);

$$C_p = \frac{A}{2mk(V_2 - V_1)} \qquad (11)$$

Where, Cp is the specific capacitance of the material in F/g, A is the area inside the CV curve having units AV, m is the total mass of the material, k is the scan rate of CV in volts per second and (V2-V1) is the potential window of the CV (total voltage range).However, it is not advisable to compute capacitance using CV as it is not accurate and it is only best used to determine the potential window to operate the material and from CV one can know what kind of behavior the material possesses [82].

In this work, CV was used to establish the potential window of 0-1V and to give an overall trend on the behavior of the sample materials. CV was run at different scan rates, 100,50,30,20,10,5 and at 1mV/s, and five scans for every scan rate were recorded. The analysis was performed with both 2 and 3-electrode systems set up, using 1M Na_2SO_4 as the electrolyte. Two different supercapacitors were assembled for both systems and the best chosen from the two.

3.4.2. Galvanostatic Charge-Discharge (GCD)

The process of applying a steady current while the supercapacitor is charged and discharged between two predetermined voltage points is called galvanostatic cycling. This is considered the "opposite" of cyclic voltammetry and it more closely mimics real-world performance. Ideally, the curve of voltage with time should be linear with alternating positive and negative slopes. However, digression from normalcy may occur due to series resistance and electrolyte degradation. After some time, series resistance can cause the cell voltage to drop rapidly when changing from charging to discharging. Furthermore, electrolyte deterioration or pseudo-capacitance reactions can yield inflections. Additionally, when a real supercapacitor is charged and not linked to any external load, it exhibits self-discharge, which is the small amount of current that flows through the device. The parasitic current could be substantial if the cell is shorted, which could happen if there is unintentional direct contact between the electrodes. Because of the increased relative magnitude of the parasitic current at low applied current densities, this causes the cell voltage to drop during discharge more quickly than is typical.

The specific capacitance, energy and power densities can be calculated from equations 12,13 and 14 respectively,

$$C_p = \frac{4 \times I \times t_{discharge}}{m \times V} \qquad (12)$$

where I and V, respectively, stand for the discharge current and voltage drop during galvanostatic discharge, Cp is the specific capacitance and m is the total mass of the electrode material. Two electrode system set up is used to get the specific capacitance because it is a full cell and resembles the commercial application or real environment as opposed to Three electrode system which is a half cell and therefore overestimates the capacitance values.

$$E_d = \frac{1}{2 C_p (\Delta V)^2} \qquad (13)$$

Where Ed is the energy density, Cp is the specific capacitance and ΔV is the potential drop. The units can be mathematically converted to WhKg-1. Finally, the power density (WKg-1) of the material can be calculated using the below equation

$$P_d = \frac{E_d}{\Delta t} \qquad (14)$$

Where Pd is the power density, Ed is the energy density and Δt is the discharging time. This information can be obtained from a plot of the GCD data using the Origin application [83]. In this work, GCD was run at a 0- 1V potential window previously established by CV. Two and Three-electrode system GCD results were employed in calculating the specific capacitance of the material, its energy density, power density, and Electrical Series Resistance (ESR).

3.4.3. Electrochemical Impedance Spectroscopy (EIS)

One of the most rigorous methods for electrochemical characterization is Electrochemical Impedance Spectroscopy (EIS). This method involves the application of an alternating potential to the device at different frequencies, and then measuring the resulting current's amplitude and phase change. The impedance is then derived from these measurements for each frequency, and it can be displayed as a Bode plot, impedance magnitude and phase shift versus frequency plot, or a Nyquist plot, the imaginary component of impedance against the real component plot[84].

The working electrode, which is where the chemistry of interest takes place, and the counter electrode, serving as the other half of the cell, make up the two-electrode configuration. Between the working and counter electrodes, the applied potential (EA) is measured, and the resulting current is measured in the working or counter electrode lead. In the two-electrode setup, the counter electrode serves two purposes. It completes the circuit, allowing charge to move through the cell, and it also keeps the interfacial potential constant no matter how much current is flowing. Under most circumstances, it is impossible to satisfy both of these prerequisites. It is highly challenging to maintain a constant counter electrode potential in a two-electrode system when current is flowing. This feature, in combination with an absence of compensation for the voltage drop across the solution, causes a two-electrode system to have inadequate control over the working electrode potential. Two distinct electrodes perform the functions of maintaining a reference voltage and passing current more effectively [85].

The three-electrode method is an improvement over the two-electrode arrangement by resolving many of its problems. It consists of a working electrode, a counter electrode, and a reference electrode, which work together to provide better control over the voltage of the working electrode. The reference electrode serves as a standard for measuring and adjusting the potential of the working electrode without passing any current. At low current density, the reference electrode should have a constant electrochemical potential. The potential drop between the reference and working electrode is minimal due to the reference electrode's minimal current flow, resulting in a more stable reference potential. The Saturated Calomel Electrode and the Ag/AgCl Electrode are two popular laboratory reference electrodes. The counter electrode's only function is to pass all of the current required to balance the current seen at the working electrode. To complete this duty, the counter electrode frequently swings to extremely high potentials[86]. The origin application software can be best utilized to plot the Nyquist curve and analyse EIS data. A Nyquist plot plots imaginary impedances (ordinate)vs the real impedances (abscissa) at different frequencies. Different behaviors can be analysed for the different frequency regimes. The point intercepting the real x-axis at the highest measure of frequency gives the ESR of the cell.

A typical supercapacitor does not have semicircles in the Nyquist plot but ECDL capacitors can have semicircles on the Nyquist plot due to the presence of functional groups or defects at the surface of carbon material contributing to the charge transfer or from the faradaic reactions happening at the pseudo-capacitive material.

The semi-circles can also be observed in laboratory cells due to the interfacial impedance occurring at the interface between the current collector and the active material. To tell whether the semi-circle recorded is due to interfacial contact resistance or due to the charge transfer, we can record impedance at multiple potentials. If the semi-circle is correlated to the charge transfer, the semicircle will change when a different potential is applied. If it is correlated to the interfacial impedance between the current collector and the active material, it will be constant across all potentials tested. The only noteworthy changes in the impedance spectra will be in the low-frequency region when applied potential changes.

The interfacial impedance is due to passive coating on the current collector material that limits ohmic coupling between the current collector and the electrode material. This kind of impedance can be minimized through roughening of current collectors or coating the interface with the active material. Also ensuring compact contact between the two and no semicircles will be observed in the high-frequency range[84].In this work, EIS was carried out at an established frequency range to establish how the different samples experienced ESR. This was done twice for all supercapacitors for both two and three-electrode systems for comparison and the Nyquist plots were drawn for all the electrode materials.

3.5. Data Analysis

The formulas discussed below have been utilized to calculate different parameters in the characterization techniques employed in this work.

From XRD data, a crystallite size is calculated using Scherrer's formula;

$$\text{�} = K \frac{\lambda}{\beta \cos \theta} \qquad (7)$$

Where d is the diameter of the crystallite, K is a constant that depends on the shape of the crystallite, usually 0.9, λ is the wavelength and β is the full width at half maximum peak (FWHM).

To calculate specific surface area in BET analysis, the equation below was used.

$$\text{�} = \frac{1}{\text{�����} + i\text{��������}} \times \text{��} \qquad (9)$$

where CSA is the cross-sectional area of the adsorbate

From the electrochemical analysis, specific capacitance, energy density, power density, and ESR have been calculated using the equations as follows :

The specific capacitance has been calculated from GCD curves according to equation 15 below;

$$\text{�} = 4 \frac{\text{�}}{m \left(\frac{dV}{d\text{��}}\right)} \qquad (15)$$

where m is the mass of active material in the working electrode, V is the potential window in volts, t is the discharge duration in seconds (s), I is the charge-discharge current in amperes (A), and C is the specific capacitance in (F/g).

Similarly, the values of Ed, Pd, and ESR were determined using the following equations 16, 17, and 18.

$$E\text{[illegible]} = \frac{(C \times V\text{[illegible]}}{(\text{[illegible]} \times \text{[illegible]} \times \text{[illegible]}} \qquad (\text{[illegible]})$$

here E$_d$ is the energy density in Wh/Kg, C is the specific capacitance in F/g and V is the potential window in Volts.

$$P\text{[illegible]} = \frac{(\text{[illegible]}^2 \times 1000)}{4\left(\frac{\text{[illegible]}}{\text{[illegible]}}\right)\text{[illegible]}} \qquad (17)$$

Where P$_d$ is the power density in W/kg, V represents the potential window in volts, m is the mass of the active electrode material and S.A is the surface area of the electrode’s current collector

$$\text{[illegible]} = \frac{I\text{[illegible]} \times \text{[illegible]}}{2 \times I} \qquad (18)$$

Where IR is the voltage drop in Volts, SA represents the surface area of the electrode and I is the current in Amperes.

Chapter Four

4. Results and Discussions

4.1. Physicochemical Analysis Results

The physicochemical analysis was conducted using the FTIR, XRD, SEM, and BET.

4.1.1. Fourier Transform Infrared Spectroscopy

FTIR characterization was performed using Spectrum 65 FTIR (PerkinElmer) equipment for the determination of functional groups present in the synthesized samples.

The structures of rGO, PDMA, MnO_2/PDMA, and rGO /MnO_2/PDMA were investigated using Fourier transform infrared (FTIR) spectroscopy. The FTIR spectra of rGO, PDMA, MnO_2/PDMA, and rGO/MnO_2/PDMA are shown in *Figure 12*. The acute C=C band at 1600 cm-1, the broad and strong peak at about 3400 cm-1 resulting from the –OH stretching vibration, and a peak at roughly 1700 cm-1 arising from the C=O stretching vibrations of carboxylic groups are the three peaks visible in the FT-IR spectra of rGO. This discovery confirms that graphene oxide forms and decreases the sp2 carbon atomic frame[87].

The 400–4000 cm−1 range of the PDMA (*Figure 12*(b))'s spectrum is where the main characteristic bands may be seen. An extensive, feeble band situated approximately at 3237 cm−1 is credited to the N–H stretching mode. The peak at 1194 cm−1 represents the quinoid rings in the polymer backbone, while the corresponding stretching vibration bands of the benzenoid rings are at 1504 and 1447 cm−1. The signal at around 1120 cm−1 is ascribed to the carbon–hydrogen plane bending vibration produced during protonation, whereas the bands at 1028 and 982 cm−1 indicate the presence of O–methoxy groups in PDMA. Finally, the ortho-substituted benzene ring is represented as an 800 cm−1 band[88].

The 400–600 cm−1 region is frequently associated with MnO_2 peaks (*Figure 12*c and d). The vibrations of Mn-O are the cause of the peaks at 563, 615, 665, and 670 cm−1. The peaks at 772 and 775 cm−1 are caused by the PDMA ring's C-H out-of-plane deformation. In addition, the peaks at 1279, 1290, 1029, and 1034 cm−1 are linked to the stretching of the C–N and C–H deformation vibrations. Further, the vibration bands 1157, 1165, 960, and 962 cm−1 are caused by the doped states of PDMA that are created. Figure 12(d) of the FTIR spectra of rGO/MnO_2/PDMA shows almost identical results to *Figure 12*(c), except for some main peak shifting resulting from changes in the chemical environment. The unique high spots in the rGO/MnO_2/PDMA spectra, which are only seen at about 1672, 1364, and 1160 cm−1, stand for the C=O, O–H, and C–O facets of the rGO carboxylic acid group, in that order. These characteristics confirm that the rGO is attached to MnO_2/PDMA. The peaks in the FTIR spectra demonstrate the effective synthesis of rGO, PDMA, binary, and ternary nanocomposites and they agree with the FTIR spectrum of PDMA produced by M. Gupta in their work titled “Synthesis and characterization of poly (2,5-dimethoxy aniline) and poly (aniline-Co-2,5-dimethoxy aniline): The processable conducting polymers”[71].

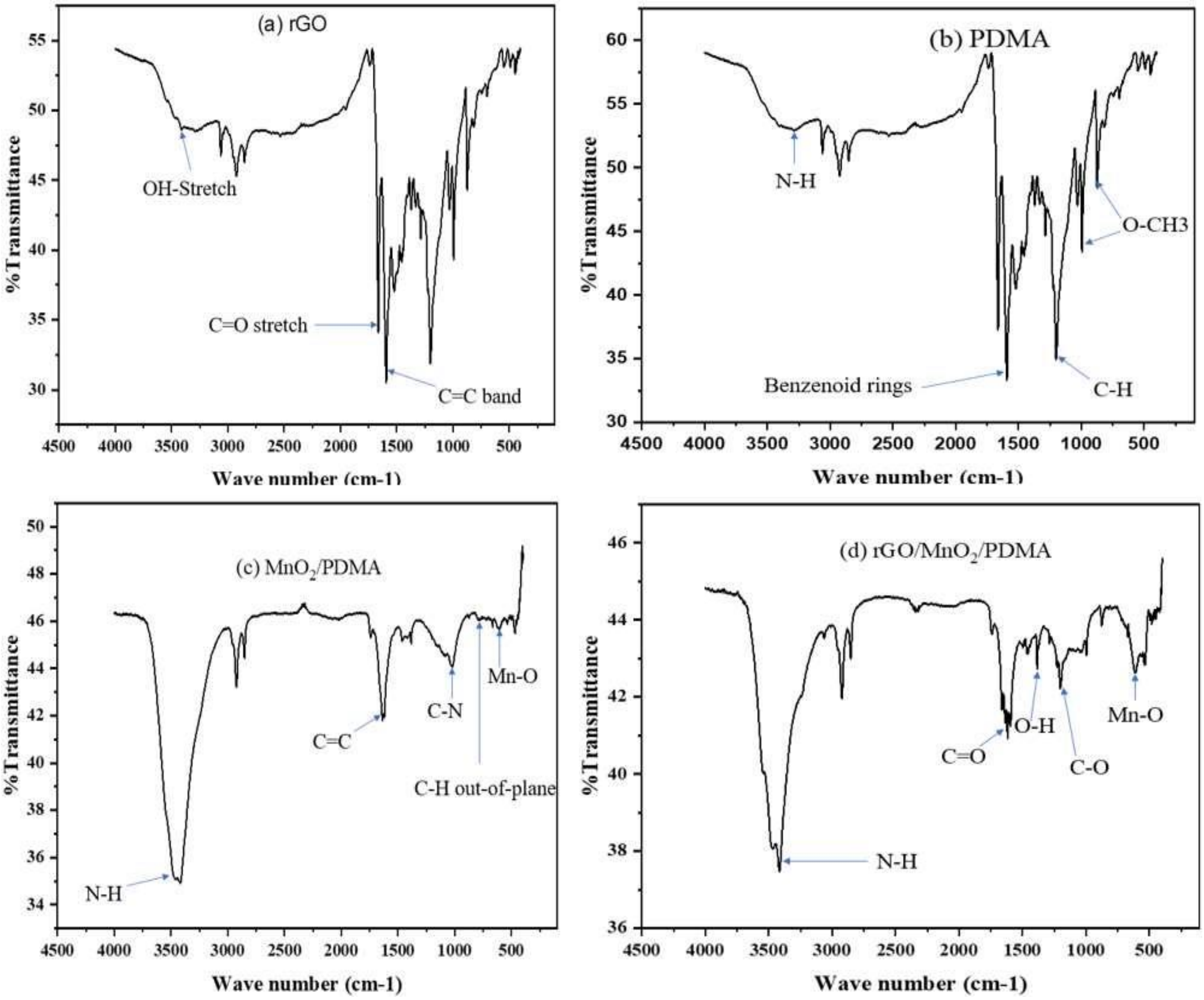

Figure 12. FTIR spectra of (a) rGO, (b)PDMA, (c) MnO_2/PDMA, and rGO/MnO_2/PDMA respectively

4.1.2. X-ray Diffraction Spectroscopy

XRD characterization was performed using Miniflex 600 (Rigaku) equipment for the determination of crystalline structures of the synthesized samples

The XRD pattern of rGO (*Figure 13*a) shows three peaks: a large peak at 2θ = 25.8°, a small peak centered at 2θ = 11.7°, and a third peak at 2θ = 40.3°. The interlayer distances of 4.47, 3.53, and 2.58 Å, respectively, are correlated with these peaks. The XRD pattern of PDMA (*Figure 13* b) demonstrates diffraction peaks at 2θ values of 11º, 16º, and 27.02º, which are responsible for the crystalline nature of the material. The MnO_2/PDMA (*Figure 13* (c)) and rGO/MnO_2/PDMA (*Figure 13* (d)) XRD patterns are similar, showing that the MnO_2 particles on the rGO substrate have been successfully immobilized by PDMA. The presence of additional peaks in the binary and ternary composite material depicts the multiple phases due to the formation of composite materials. All significant reflections [2θ= 21.20 (120), 29.12 (310), 37.50 (131), 42.50 (300), and 59.00 (160)] in the XRD pattern can be registered to the orthorhombic phase MnO_2, with lattice constants of a) 56.36 Å, b) 10.15 Å, and c) 54.09 Å (JCPDS 14-644). This is consistent with the patterns previously observed for MnO_2 and validates that the crystalline phase of MnO_2 occurs throughout the synthesis.

The prominent peak centered at approximately 2θ=26.30 indicates the effective synthesis of PDMA and is ascribed to the diffraction of the (110) plane of the as-formed PDMA crystalline phase. On the other hand, the steep peak at 2 θ = 11.00, which is its (002) plane for pure rGO, almost disappeared. The increased interspace distance of the graphene layer, resulting from PDMA/MnO_2 intercalation between rGO sheets, explains this. There is a presence of high-intensity sharp peaks in all the materials, representing high ordered arrangement of atoms and therefore high crystallinity levels in the synthesized materials. The additional peaks in the composite materials also present high crystalline composite materials. These results are in total agreement with those obtained by G. Han in his work titled "MnO_2 nanorods intercalating graphene oxide/polyaniline ternary composites for robust high-performance supercapacitors"[89].

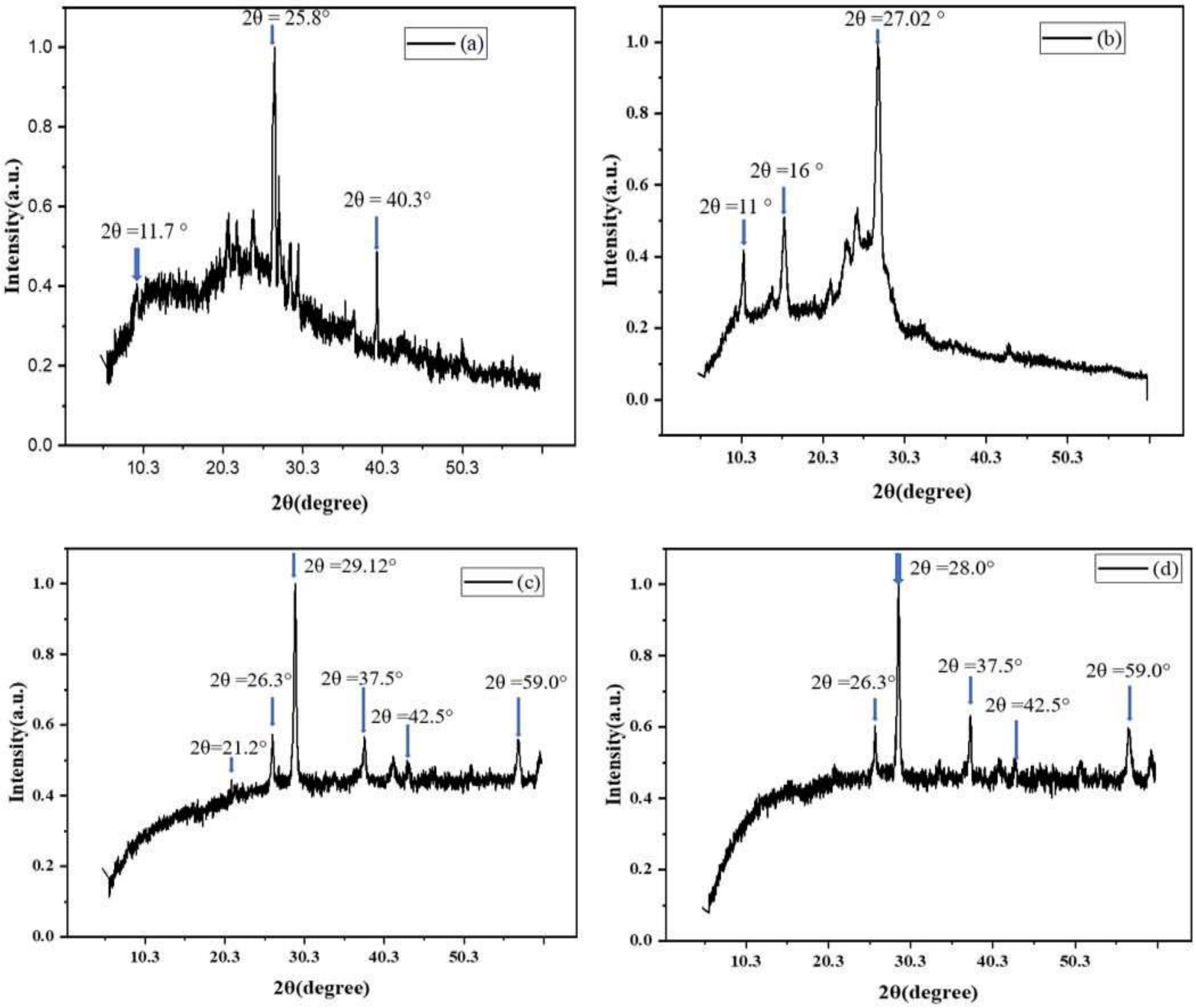

Figure 13. The XRD patterns of rGO(a), PDMA(b), MnO_2/PDMA(c), and rGO/MnO_2/PDMA(d)

4.1.3. SEM-EDS Analysis

The elemental composition and the morphological analysis of the samples (rGO, PDMA, MnO_2/PDMA, and rGO/MnO_2/PDMA) were performed using Zeiss Crossbeam 540 operated at 2 kV for imaging and 20 kV for EDS. EDS data was acquired using an Oxford Xmax detector with Aztec software optimized using copper reference. The rGO and PDMA nanoparticles demonstrated a smooth surface morphology (*Figure 14* a and b). *Figure 14* shows smooth plate-like layers of rGO sheets, while the PDMA image shows the presence of hexagonal-shaped rods of PDMA[90], Appendix A contains more information on the images for all the electrode materials under different magnifications. Furthermore, SEM images of MnO_2/PDMA show a highly agglomerated rice husk petal-like morphology that is evenly distributed on the long needle-like rods of PDMA[91].

The nanomorphology of MnO_2 is further supported by the broadening of additional peaks in XRD data of MnO_2/PDMA and rGO/MnO_2/PDMA. The ternary image shows multiple layers of rGO sheets with rough surfaces due to MnO_2 particles evenly distributed on their surfaces, as well as hexagonal rods of PDMA layered together with their surfaces completely covered with evenly distributed MnO_2 particles[32]. There is the presence of all three electrode materials in the ternary composite material rGO/MnO_2/PDMA image. The MnO_2 post-treatment systemically filled the pores in the surface of the PDMA nanoparticles, improving the interconnectivity of the grains thereby making the composites compact. Although the porosity of rGO favors electrolyte penetration and enhanced charge storage and transfer, it increases grain boundary density and reduces particle-particle interconnectivity thereby resulting in high charge transport resistance as observed in the Nyquist (*Figure 27*). MnO_2 nanoparticles served to fill the voids in the pure PDMA which is expected to increase the electron transport of the PDMA.

As seen in *Figure 14* rGO creates composites with a rough surface and features wrinkling and stacking structure. The rGO/MnO_2/PDMA nanocomposite has a uniformly distributed rGO distribution and a comparatively compact surface. MnO_2 nanoparticles accumulated between the rGO sheets and PDMA layers as illustrated in *Figure 14* binary and ternary composites. Due to this accumulation, there was insufficient use of rGO's strong conductivity since it reduced the interfacial contact between MnO_2 and rGO. The electrochemical performances of the nanocomposites in the redox processes were enhanced by the evenly distributed MnO_2. Furthermore, well-fabricated binary and ternary nanocomposites of active materials shorten the diffusion paths for electrons and electrolytes, enhancing the rate of migration and diffusion of electrolytes in electrochemical performances.

The elemental composition (*Figure 14*c) shows high amounts of carbon and oxygen in rGO as expected. High amounts of carbon, oxygen, and nitrogen are observed in PDMA affirming its successful synthesis. There is the presence of Manganese in high amounts for both the binary and the ternary composites among carbon, oxygen, and nitrogen elements as per the theoretical expectations, suggesting the successful synthesis of the composites. The rest of the elements present in minute amounts are a result of impurities present as all the chemicals are not completely pure. All the 20* magnification images have been taken at a scale of 1 micrometer while the 100* magnification has been taken at a 100nanometre resolution scale for all the materials. These results agree with M. Ates in his work titled Synthesis, characterization, and supercapacitor performances of activated and inactivated rGO / MnO_2 and rGO / MnO_2 / PPy nanocomposites[32].

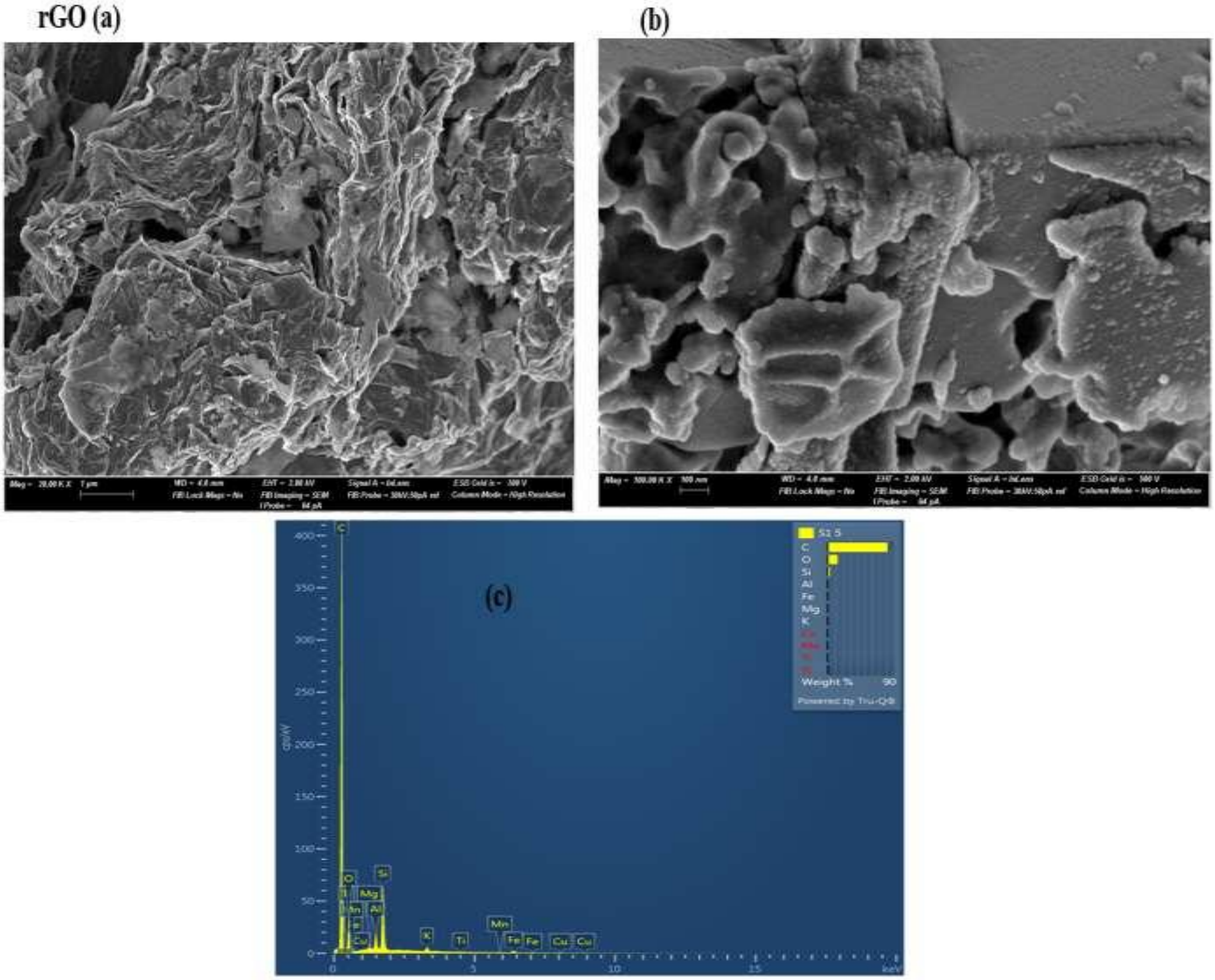
rGO (a)
(b)
(c)
C
O
Si
Mg
Mn
Al
Fe
Cu
K
Ti
S1 5
Weight %
90
Powered by Tru-Q®
cps/eV
400
350
300
250
200
150
100
50
0
5
10
15
keV

PDMA(a)

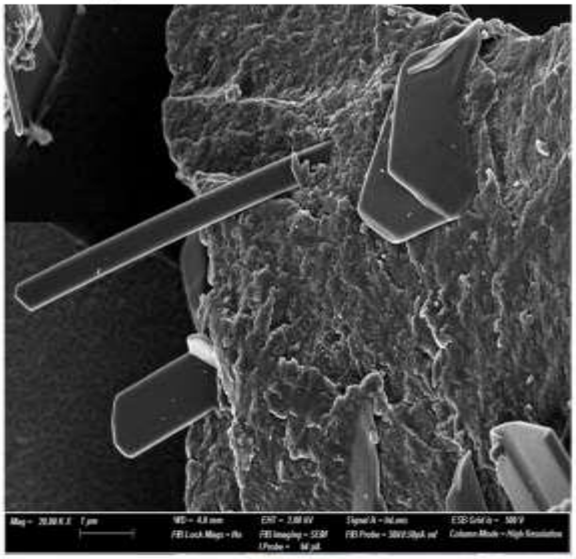
Mag = 20.00 K X
1 µm
WD = 4.8 mm
FIB Lock Mags = No
EHT = 2.00 kV
FIB Imaging = SEM
I Probe = 64 pA
Signal A = InLens
FIB Probe = 30kV:50pA
ESB Grid = 500 V
Column Mode = High Resolution

(b)

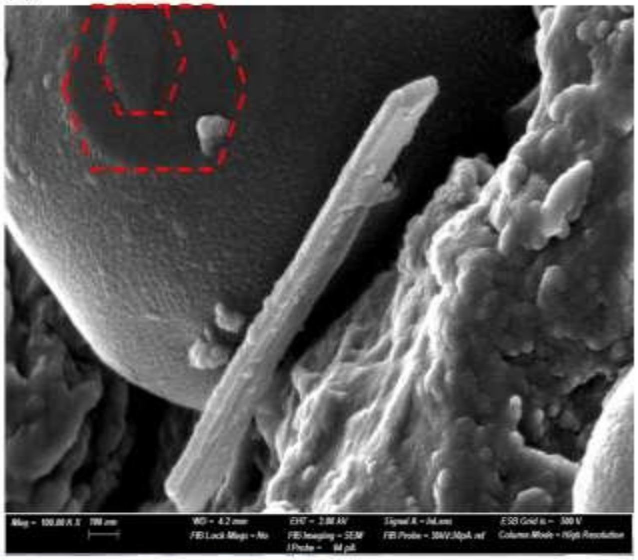
Mag = 100.00 K X
100 nm
WD = 4.2 mm
FIB Lock Mags = No
EHT = 2.00 kV
FIB Imaging = SEM
I Probe = 64 pA
Signal A = InLens
FIB Probe = 30kV:50pA
ESB Grid = 500 V
Column Mode = High Resolution

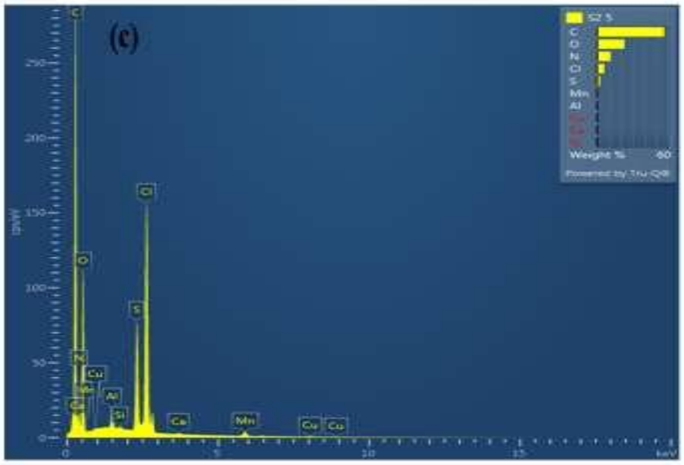
(c)
C
O
N
Cl
S
Cu
Mn
Al
Si
Ca
Mn
Cu
Cu
250
200
150
100
50
0
cps/eV
0
5
10
15
keV
S2 5
C
O
N
Cl
S
Mn
Al
Weight %
60
Powered by Tru-Q®

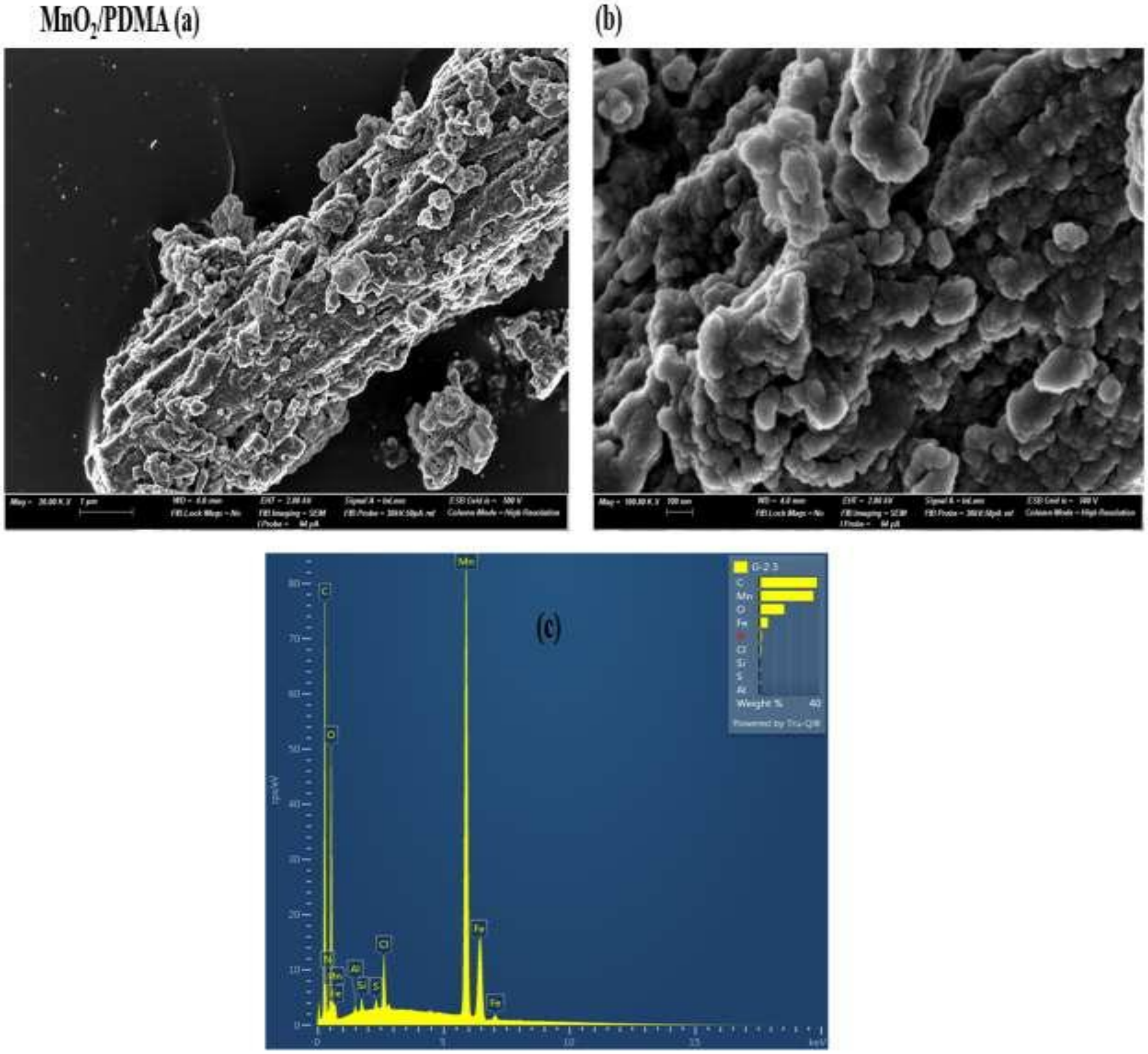
MnO$_2$/PDMA (a)
(b)
(c)
C
O
N
Mn
Fe
Al
Si
S
Cl
Mn
Fe
Fe
cps/eV
keV
0
5
10
15
0
10
20
30
40
50
60
70
80
G-2.5
C
Mn
O
Fe
N
Cl
Si
S
Al
Weight %
40
Powered by Tru-Q®

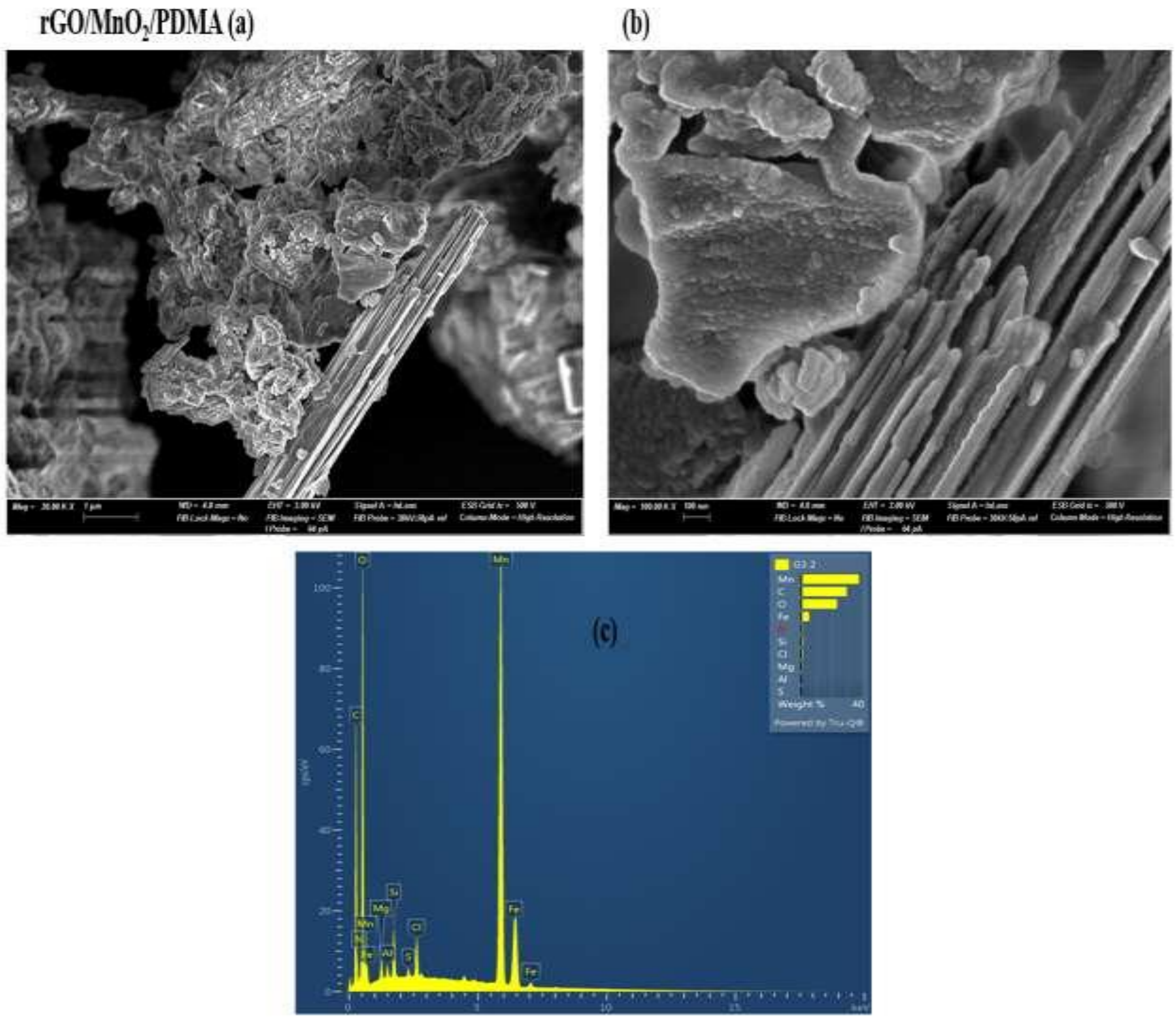

Figure 14. SEM-EDS images of rGO, PDMA, MnO_2/PDMA, and rGO/MnO_2/PDMA for (a) 1 micrometer and (b) for 100-nanometre magnification

4.1.4. BET Analysis

BET analysis was performed using TriStar II Plus Version 3.03 equipment for the surface area determination of the synthesized samples. The determination of N_2 adsorption-desorption isotherms (*Figure 15*) allows for an examination of the samples' porous structural characteristics as performed for rGO, PDMA, MnO_2/PDMA-80% and rGO/MnO_2/PDMA-80%. All the samples exhibit type V IUPAC classification of porous materials which signifies that they are mesoporous with type H3 hysteresis and have slit-shaped pores. According to Z. Alothman, Isotherms that indicate type H3 do not display any limit in adsorption at high P/Po, which is noticeable in non-rigid clusters of plate-like particles. The desorption curve of the H3 hysteresis manifests a slope connected to a force on the hysteresis loop, known as the tensile strength effect. This phenomenon is likely to occur for nitrogen at 77 K in the relative pressure range of 0.4 to 0.45[79].

Figure 16 shows that most of the particles' diameters are in the range of 2nm-50nm in all the samples which confirms that they are mesoporous. Unlike microporous materials, mesoporous materials usually have lower surface areas as indicated in *Table 1*, with rGO having the highest BET surface area of 12.8m^2/g. The binary composite has a slightly higher surface area(7.4m^2/g) compared to the ternary composite material(5.4m^2/g). This is because the high porosity of rGO is reduced by MnO_2 nanoparticles which occupy its pores rendering the ternary composite material less porous and therefore having less pore volume and consequently less surface area.

PDMA has a significantly low surface area (0.4m^2/g). Doping the PDMA with MnO_2 has, however, improved its surface area by many orders of magnitude making the binary composite's surface area five times higher than the pure PDMA (*Table 2*). This is because the doping of PDMA creates interlinkages that cause crystallinity to increase and consequently increase its pore volume. Despite the ternary composite having a lower surface area compared to the binary composite, it has a higher specific capacitance than the binary composite. This is MnO_2 offers an increased interfacial contact area between the rGO and the PDMA particles, as observed in the SEM images (*Figure 14*) creating shorter diffusion paths for rapid ionic diffusion, and a higher concentration of electrochemically active sites [85].

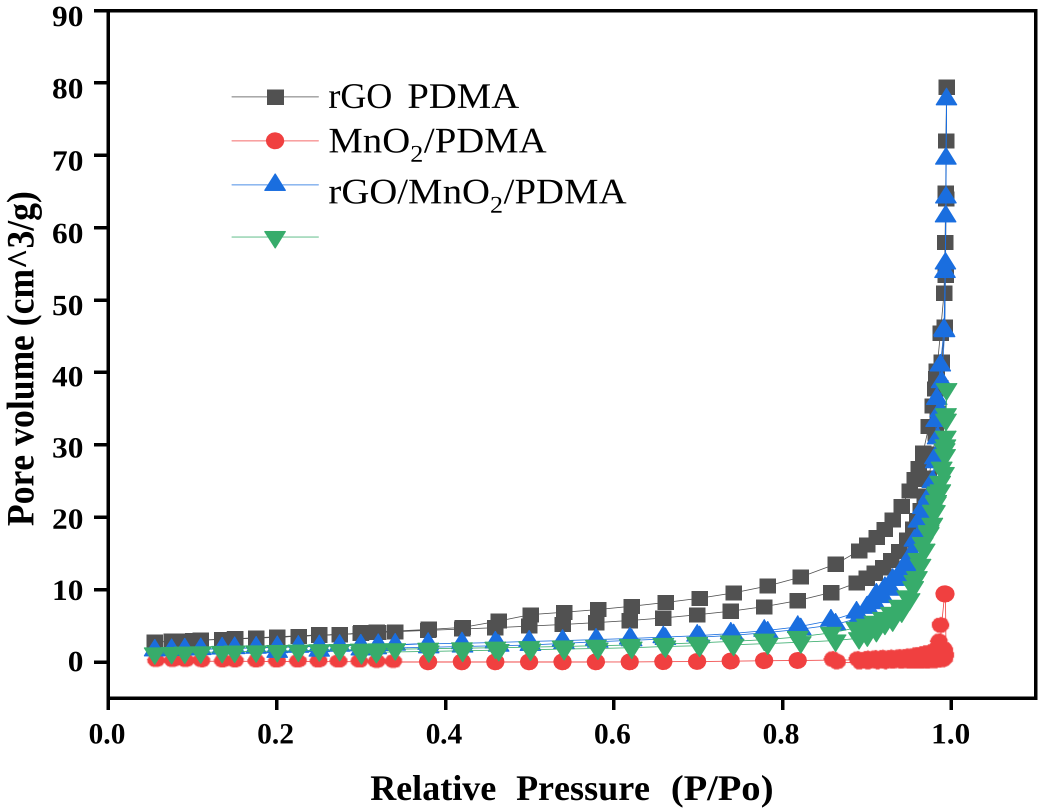

Figure 15. BET-adsorption/desorption isotherm plots of relative pressure against volume at STP for rGO, PDMA, MnO_2/PDMA, and rGO/MnO_2/PDMA

Table 2 Different Surface areas of rGO, PDMA, MnO_2/PDMA, and rGO/MnO_2/PDMA

Electrode Material	Surface Area(m^2/g)				
	BET	**Langmuir**	**t-Plot**	**BJH**	
				Adsorption	**Desorption**
rGO	**12.08**	**349.63**	**10.97**	**10.47**	**15.48**
PDMA	**0.4**	**0.09**	**0.82**	**0.38**	**0.57**
MnO_2/PDMA	**7.4**	**100.5**	**6.4**	**6.2**	**8.2**
rGO/MnO_2/PDMA	**5.4**	**83.4**	**4.5**	**4.2**	**5.8**

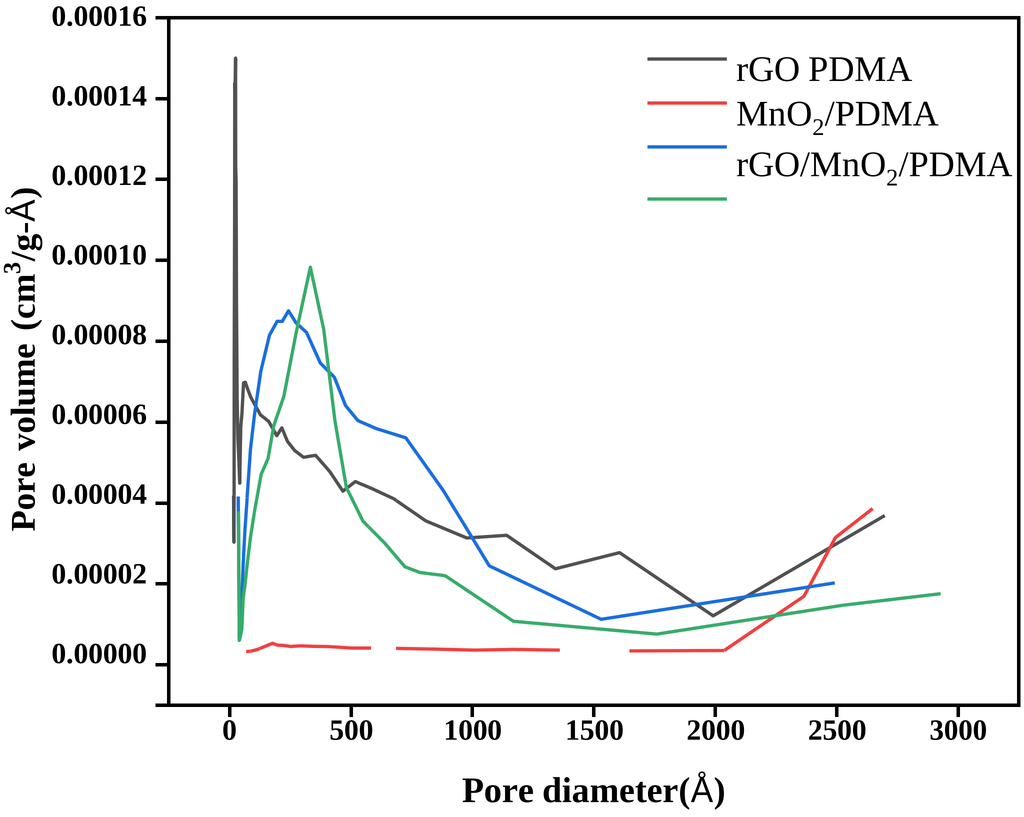

Figure 16. Graph of pore diameter against pore volume distribution for rGO, PDMA, MnO_2/PDMA, and rGO/MnO_2/PDMA

4.2. Electrochemical Characterization

In 1M Na_2SO_4 solutions, the capacitive performance of rGO, MnO2/PDMA, and rGO/MnO_2/PDMA was assessed using galvanostatic charge/discharge (GCD) and cyclic voltammetry (CV) techniques. Additionally, their electrochemical characteristics were assessed using electrochemical impedance spectroscopy (EIS).

4.2.1. Cyclic Voltammetry Measurements

The two-electrode arrangement is the closest to real-world supercapacitor applications. As a result, we created both symmetric and asymmetric supercapacitors, where the active materials serve as the positive and negative electrodes, respectively, and pure, binary, and ternary nanocomposites of materials as the positive electrode and activated carbon as the negative electrode. In the potential range between 0.0 and 1.0 V, (*Figure 17*) displays the two-electrode CV curves of rGO, PDMA, MnO_2/PDMA, and rGO/MnO_2/PDMA nanocomposites at a scan rate of 1 mV/s, and the CV curves for rGO at various scan rates (1,5,10,20,30,50, and 100 mV/s). *Figure 18* displays three-electrode CV curves of rGO, PDMA, MnO_2/PDMA, and rGO/MnO_2/PDMA nanocomposites at a scan rate of 1 mV/s, and the CV curves for rGO at scan rates (1,5,10,20,30,50, and 100 mV/s).

The CV curves progressively grew as the scan rate increased, just like in the literature. More rectangular form is produced at lower scan rates due to delayed ion migration. At all scan rates, rGO had the largest area under the curve, followed by the ternary composite (rGO /MnO_2/PDMA), the binary composite (MnO_2/PDMA), and PDMA, based on the order of their performance. The area under the CV curve is directly proportional to the amount of charge that a material can hold. This translates to the specific capacitance of the materials. The areas under the curves decrease with a decrease in the scan rate and increase when the scan rate is increased as depicted in Figures,18, and 19. Additionally, the area under the curves and therefore the capacitance of the material is larger in a three-electrode system compared to a two-electrode system. This is because the former is a half-cell, and therefore only gives the performance of a single electrode. On the other hand, a two-electrode system is a full cell(device) and it considers the two electrodes, leading to less specific capacitance values. This full-cell arrangement is what is used practically in industries as it gives practical capacitance values.

The rGO curve resembles a symmetrical rectangular shape, as would be expected from the behavior of a double-layer supercapacitor. However, the presence of pseudocapacitance caused by the pseudocapacitor materials (PDMA and MnO_2) caused the curve to deviate to non-symmetrical shapes in PDMA, binary, and ternary composites. These results agree with M. Ates in his work titled Synthesis, characterization, and supercapacitor performances of activated and inactivated rGO / MnO_2 and rGO / MnO_2 / PPy nanocomposites[89].

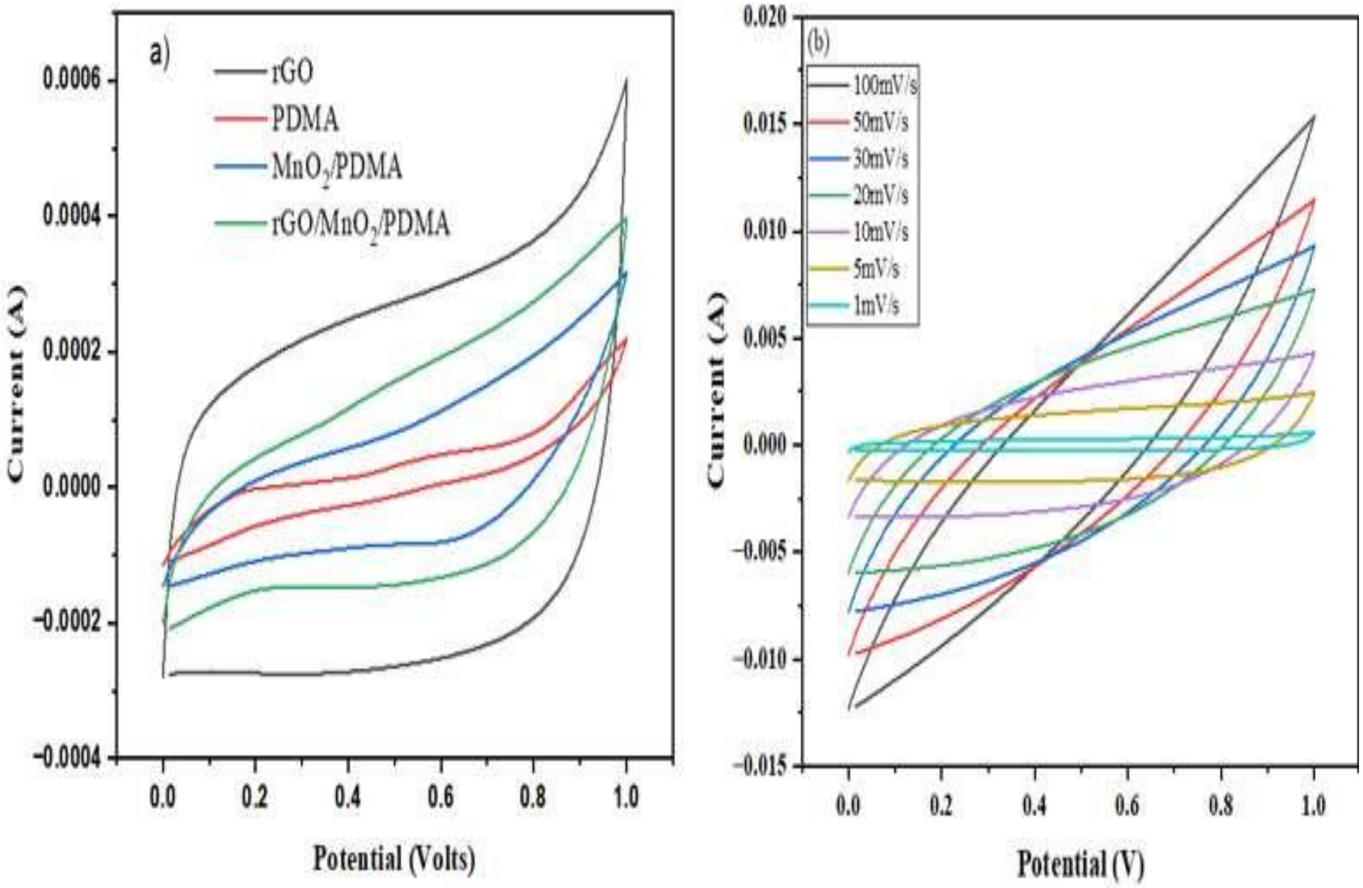

Figure 17. (a) Two-electrode CV curves for rGO, PDMA, MnO_2/PDMA, and rGO/MnO_2/PDMA at 1mV/s, (b) Two-electrode CV curves for rGO at different scan rates (100,50,30,20,10,5,1mV/s)

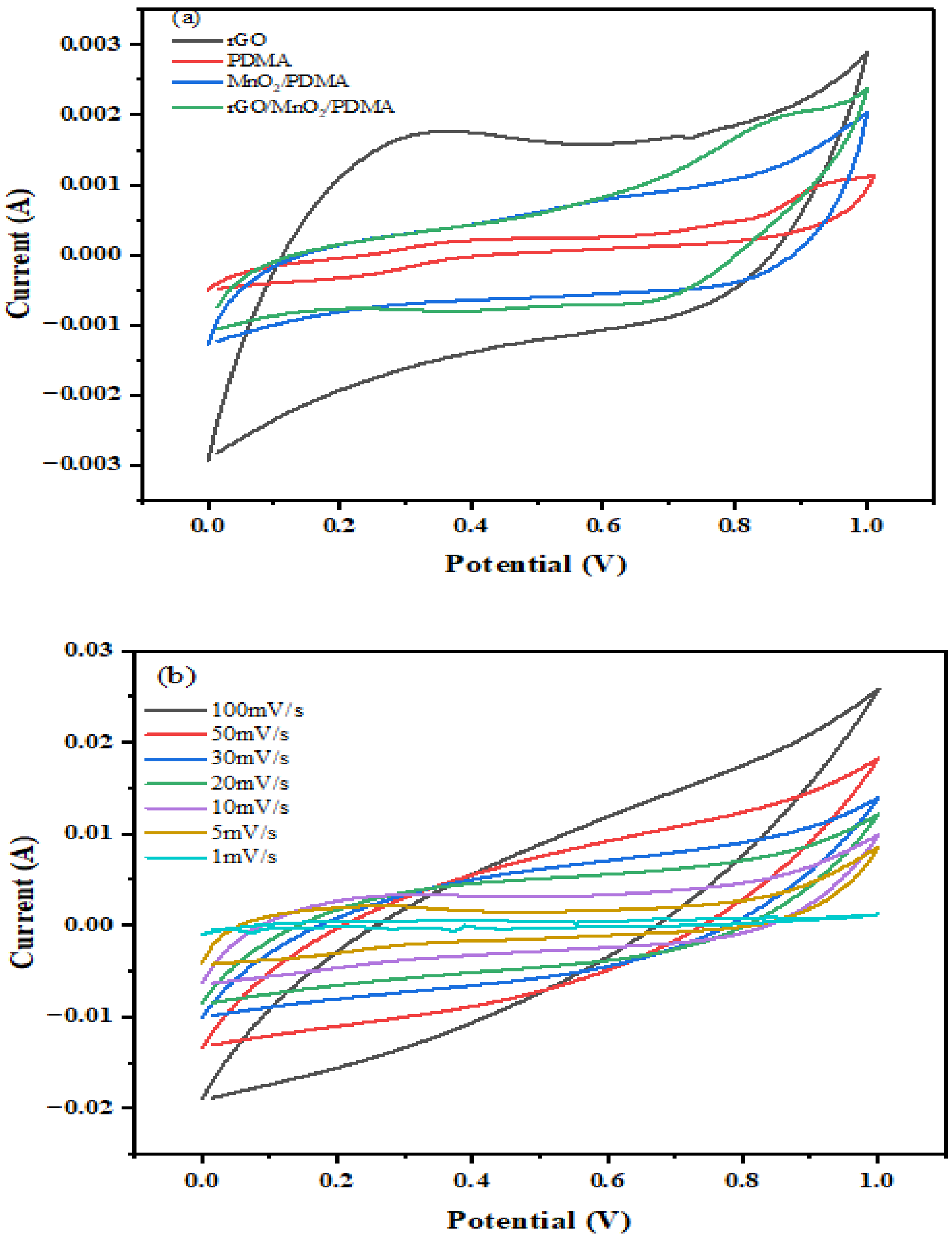

Figure 18. (a) Three-electrode CV curves for rGO, PDMA, MnO_2/PDMA, and rGO/MnO_2/PDMA at 1mV/s, (b) Three-electrode CV curves for rGO at different scan rates (100,50,30,20,10,5,1mV/s)

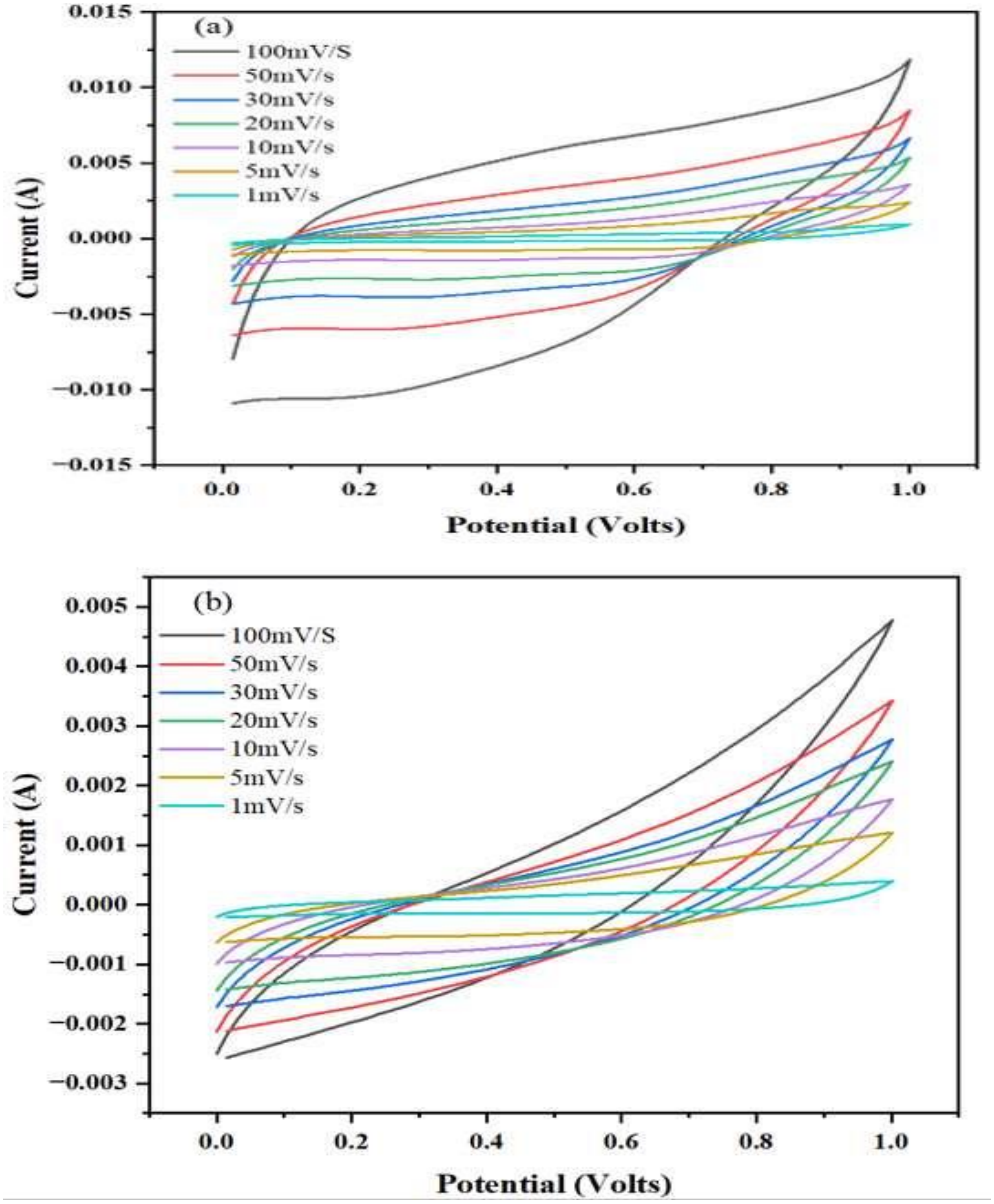

Figure 19. (a) Three, and (b) two-electrode system CV curves for rGO/MnO_2/PDMA at all scan rates(100,50,30,20,10,5,1mV/s)

4.2.2. Galvanostatic charge/discharge measurements

In a 1 M Na2SO4 solution, the galvanostatic charge/discharge curves of rGO, PDMA, MnO_2/PDMA, and rGO/MnO_2/PDMA were measured at current densities of 0.0016, 0.0031, 0.0047, 0.0063, and 0.0079A/cm^2. As seen in *Figure 20*, every curve displays an equilateral triangle form, suggesting that the hybrid materials are highly reversible throughout the charge/discharge process. The reason for the extended charging/discharging duration at lower current densities is the adequate insertion or release of Na+1 during the process.

Figure 20 a and b show a two, and three-electrode comparison of the galvanostatic charge/discharge curves of rGO, MnO_2/PDMA, and rGO/MnO_2/PDMA at 0.0016A/cm^2 current density. At the same current density of 0.0016A/cm^2, the maximum specific capacitance of rGO (499.5 F/g) is determined from the asymmetric arrangement of the three-electrode system, which is significantly greater than that of rGO/MnO_2/PDMA (176.4F/g), MnO_2/PDMA (157.9 F/g), and PDMA (66.3 F/g). The same pattern is seen when the current density is increased further, between 0.0016 and 0.0079 A/cm^2 (*Figure 21*a, and b), demonstrating the ternary hybrid's robustness as electrode material. The behavior of rGO GCD curves at different current densities, from 0.0016A/cm^2 to 0.0079A/cm^2, is shown in (*Figure 21*). The current density of 0.0016A/cm^2 is where the area under the curve is largest, and as the current increases, the area declines towards the current of 0.0079A/cm^2. This demonstrates that charge storage reduces with increasing current and increases with lower current, a relationship that is closely related to the area under the curve.

The corresponding maximum specific capacitance values, rGO (151.5F/g), rGO/MnO_2/PDMA (87F/g), MnO_2/PDMA (56.8F/g), and PDMA (50.3F/g), computed from an asymmetric two-electrode system configuration at the same current, show the same trend but have somewhat lower values.

Similarly, maximum specific capacitance values from symmetrically configured two-electrode systems were calculated. The specific capacitance values are significantly lower compared to the asymmetric configuration calculated above, with the binary composite giving better values than the ternary composite as a differentiating factor in the trend observed previously. rGO (117.6F/g), MnO_2/PDMA (18F/g), rGO/MnO_2/PDMA(2F/g) and PDMA(1.7F/g). This could be due to the reduced surface area in the ternary composite brought by the polymer nanoparticles occupying the pores of the rGO and therefore reducing the porosity and thus the surface area of the material.

To assess the effects of the amount of MnO_2 in the composite materials, the amount of MnO_2 (80%) used previously as per the results above was reduced to 60% and 30% respectively, assembled asymmetrically both in two and three-electrode systems and analysed electrochemically for comparison. The maximum specific capacitance values obtained from a current of 0.001 in three-electrode system are as follows; MnO_2/PDMA-60%(49F/g), rGO/MnO_2/PDMA-60%(32F/g) for the 60%MnO_2 and MnO_2/PDMA-30%(9F/g) and rGO/MnO_2/PDMA-30%(30.6F/g) for 30% MnO_2 content. For two- electrode system; MnO_2/PDMA-60%(22.3F/g) and rGO/MnO_2/PDMA-60%(15.9F/g) for 60%MnO_2, and MnO_2/PDMA-30%(12.4F/g) and rGO/MnO_2/PDMA-30%(26.7F/g) for 30%MnO_2 content. These results are well tabulated in *Table 3*.

From the results, it's evident that the specific capacitance decreases when the amount of MnO_2 is reduced. It is also notable that the binary composite at 60%MnO_2 has higher specific capacitance values than the ternary composite but it’s not the case for 30%MnO_2 as the ternary composite has higher specific capacitance values than the binary composite. This could be because the decrease in MnO_2 causes an increase in surface area in the ternary composite as the composite becomes more porous due to less MnO_2 occupying the rGO pores which therefore stores more charge as a result hence the higher capacitance values.

PDMA was run at much lower current densities from 0.00016-0.00079A/cm^2 because of its relatively lower performance and therefore its data could not be directly compared to other active materials under the same curve. These results agree with M. Ates in his work titled Synthesis, characterization, and supercapacitor performances of activated and inactivated rGO / MnO_2 and rGO / MnO_2 / PPy nanocomposites[89].

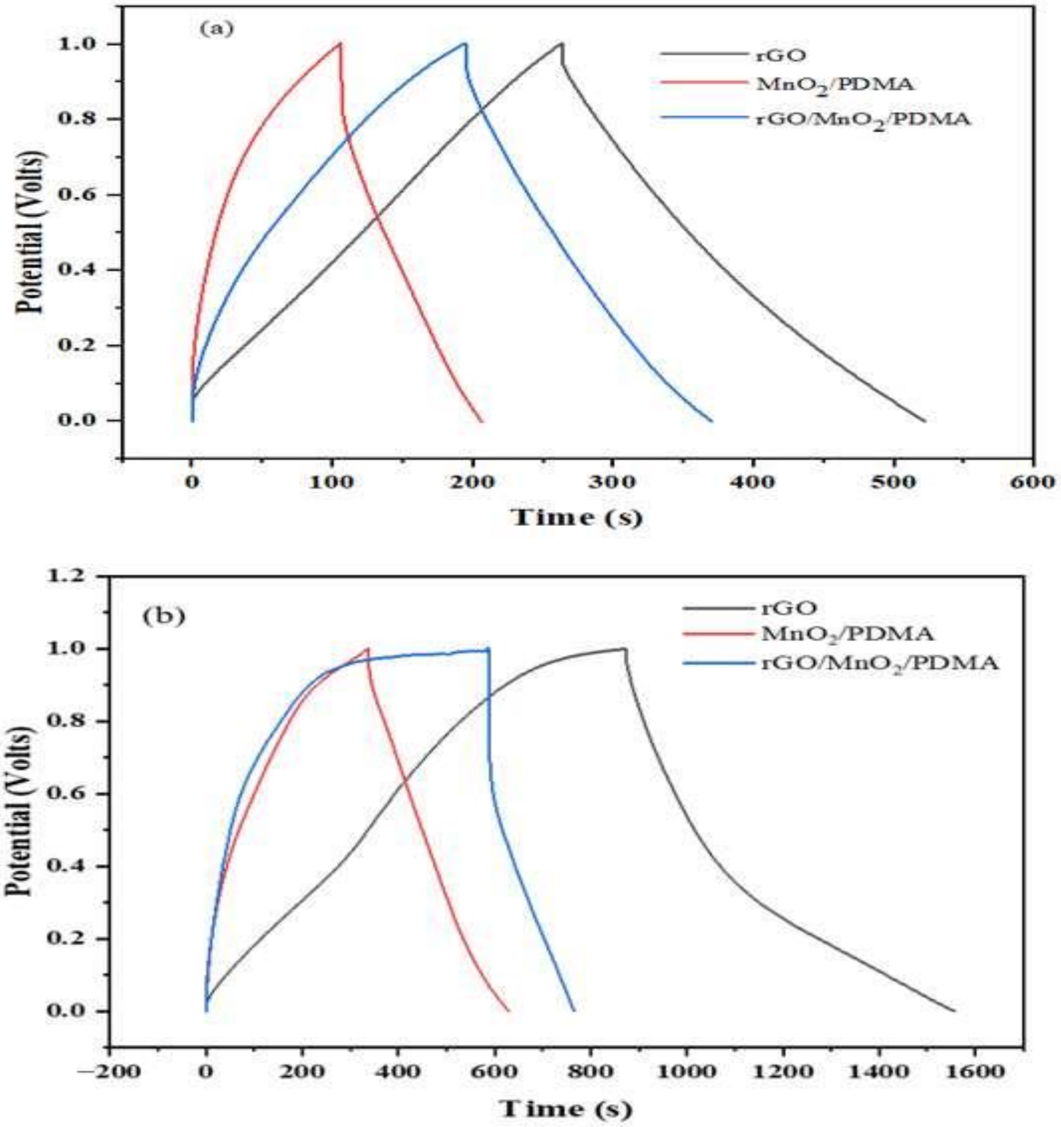

Figure 20. (a) Two, and (b) Three-electrode GCD curves for rGO, MnO$_2$/PDMA, and rGO/MnO$_2$/PDMA at 0.0016A/cm^2 current density

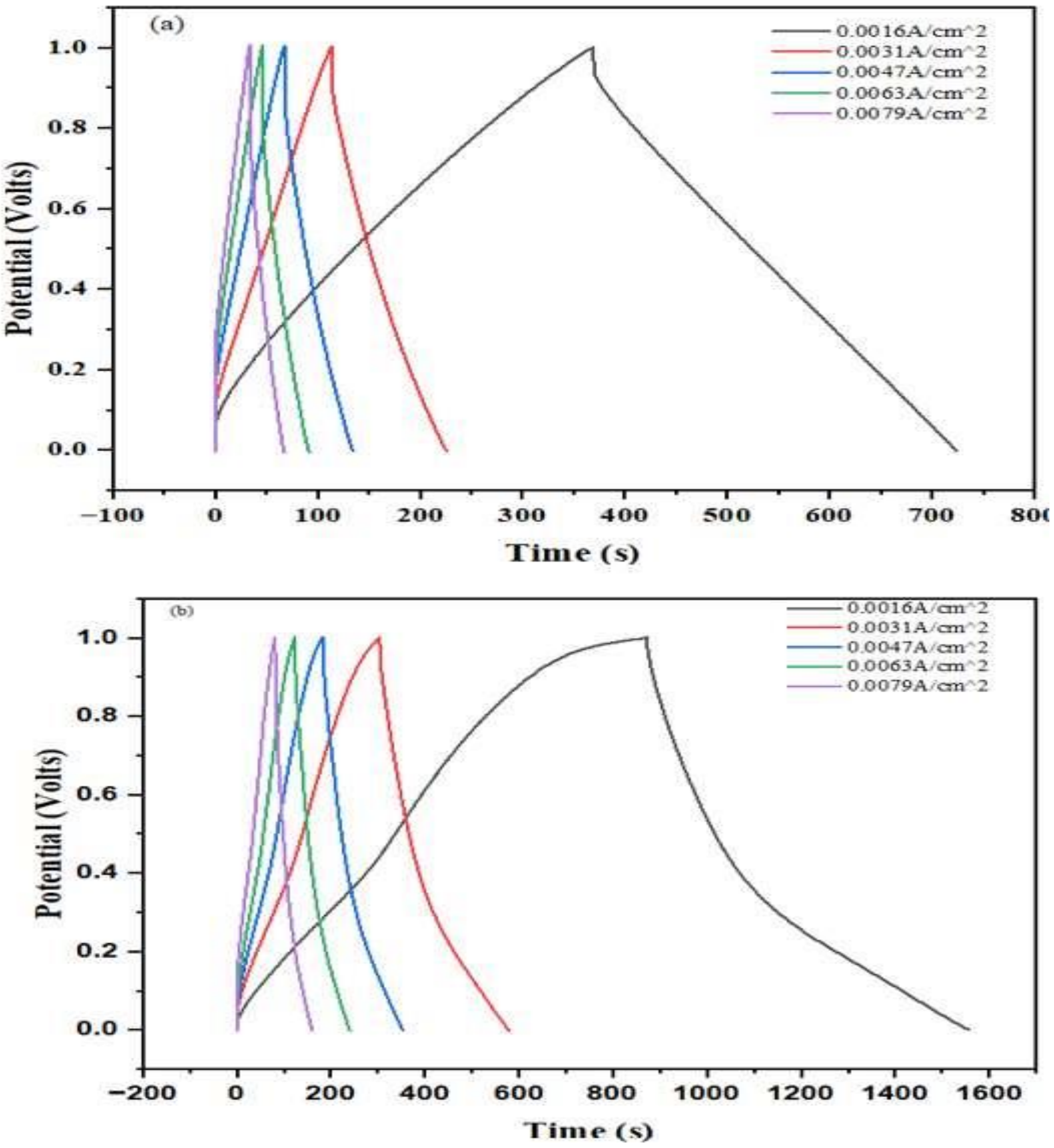

Figure 21. (a) Two, and (b) Three-electrode GCD profiles of rGO at current densities ranging from 0.0016-0.0079 A/cm^2

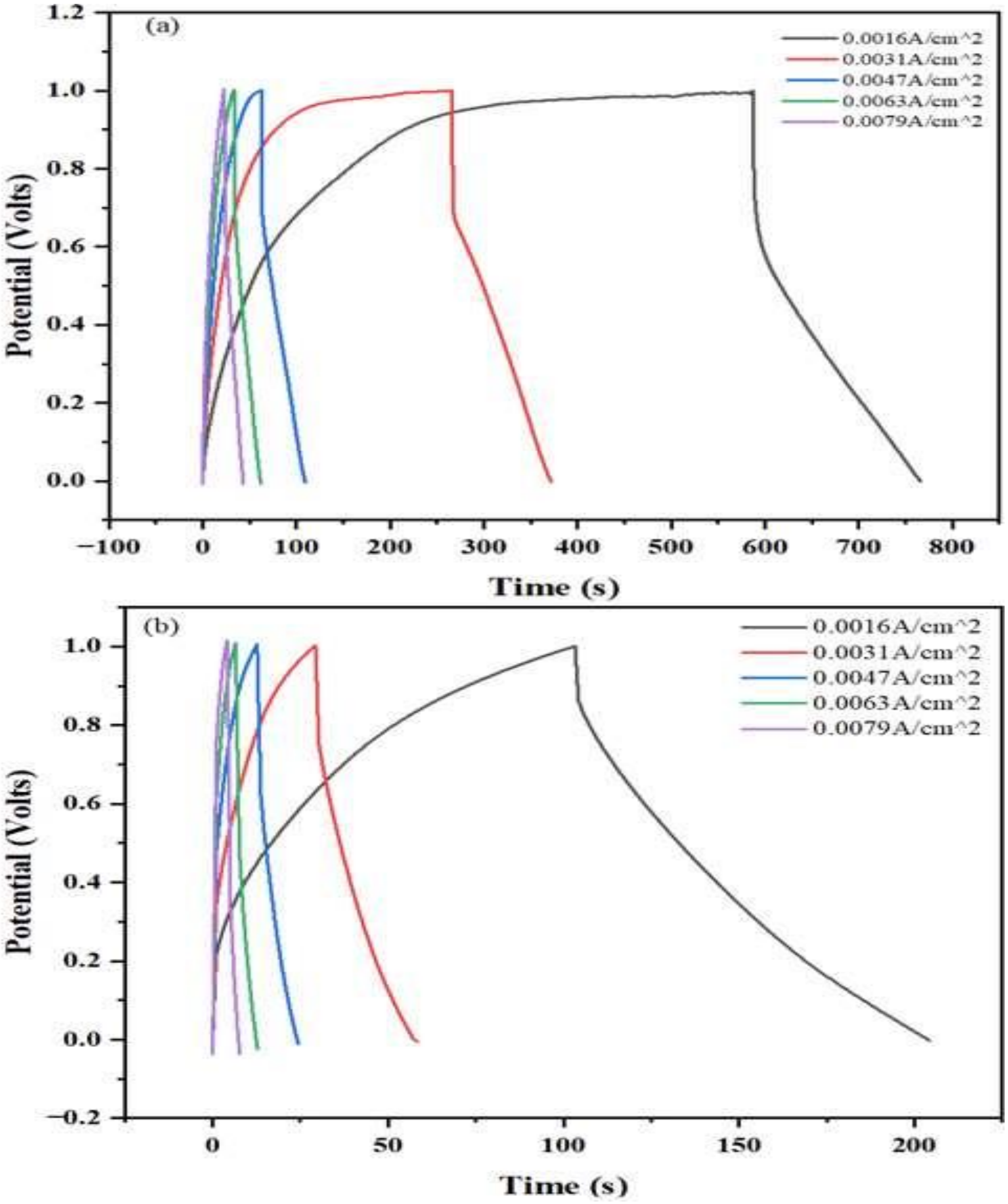

Figure 22. (a) Three, and (b) Two-electrode GCD profiles of rGO/MnO_2/PDMA from 0.0016-0.0079 A/cm^2 current densities

Table 3 A summary of the specific capacitance values at a current density of 0.0016A/cm^2 from all the samples (rGO, PDMA, MnO_2/PDMA, rGO/MnO_2/PDMA, MnO_2/PDMA-60%, rGO/MnO_2/PDMA-60%, MnO_2/PDMA-30%, and rGO/MnO_2/PDMA-30%)

	Specific capacitance(F/g)		
	Three-Electrode system	Two-electrode system	
Electrode Material	Asymmetric configuration	Asymmetric configuration	Symmetric configuration
rGO	499.5	151.5	117.6
PDMA	66.3	50.3	1.7
MnO_2/PDMA	157.9	56.8	18
rGO/MnO_2/PDMA	176.4	87	2.1
MnO_2/PDMA-60%	49	22.5	-
rGO/MnO_2/PDMA-60%	30	15.9	-
MnO_2/PDMA-30%	25.6	12.4	-
rGO/MnO_2/PDMA-30%	30.3	26.7	-

In assessing the efficacy of supercapacitors, particularly for industrial use, the electrochemical series resistance (ESR) of the electrode materials, the maximum specific energy density (Ed), and the power density (Pd) are the other three critical characteristics. For the rGO, PDMA, and 80%MnO_2 in the binary and ternary composites, the values of Ed, Pd, and ESR were determined.

The calculated energy density (**E_d**), power density **(P_d)**, and ESR values corresponding to maximum specific capacitance values for rGO, PDMA, MnO_2/PDMA, and rGO/MnO_2/PDMA for asymmetric configuration are represented in *Table 4* below:

Table 4 The calculated E_d, P_d, and ESR values for all the active electrode materials for both two and three-electrode systems in the asymmetric configuration

Electrode material	Three-electrode system			Two-electrode system		
	E_d(Wh/Kg)	P_d (W/Kg)	ESR (ohms)	E_d(Wh/Kg)	P_d (W/Kg)	ESR (ohms)
rGO	69.4	1136	12.7	21	1429	10.1
PDMA	9.3	82	254	7	22	465
MnO_2/PDMA	21.9	595	83	6.3	35	16.8
rGO/MnO_2/PDMA	24.5	725	82	12	491	16

The ternary composite poses great potential as an electrode material after rGO since it exhibited a relatively higher energy density and power density compared to the binary composite and the conducting polymer PDMA which has lower energy density and significantly high electrochemical series resistance. The high values of ESR could be due to several possible causes such as resistance due to the current collector material, the electrolyte used as well as the resistance brought about by the long backbone of the polymer’s redox reactions.

Figure 23-26 illustrate the specific capacitance, ESR, and Energy density against current densities. rGO shows a higher level of ESR because of its nature and mode of charge storage which is entirely physical. The accumulation of charges at the interface of electrode and electrolyte exposes the device to possible resistances due to the electrolyte used, the electrode material type, and even resistance due to the current collector material. As the current density increases, the specific capacitance and energy density decreases as observed in the curves. From the figures mentioned above, it is very evident that rGO performs quite well compared to the rest of the materials. However, rGO is very expensive and therefore not economically viable for large-scale energy storage use. This explains the need to consider this work's ternary and binary composites as preferred electrode materials for supercapacitors because they are cost-effective. Using fewer amounts of rGO to improve the conductivity and surface area of the composite material helps to lower the production cost of supercapacitors.

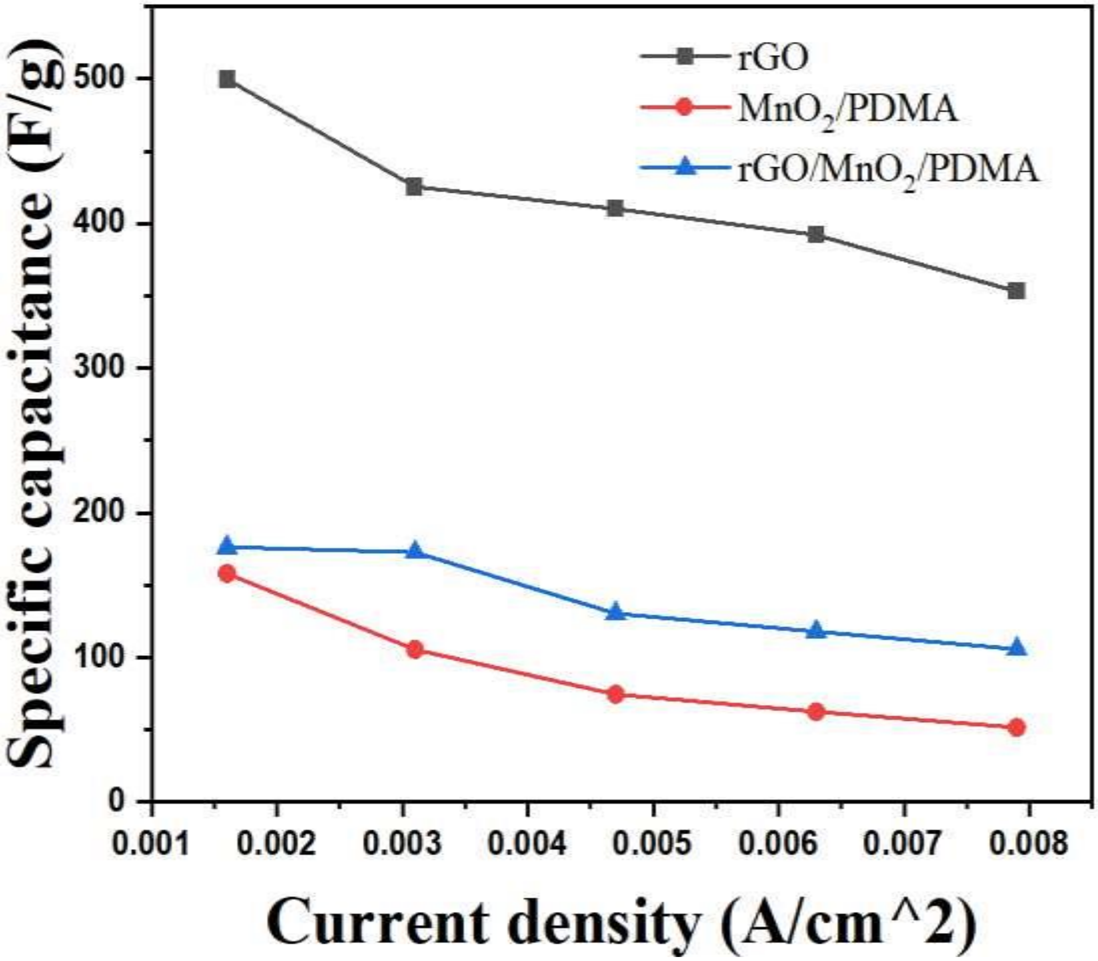

Figure 23. A plot of current densities against specific capacitance values of the synthesized samples in a three-electrode system

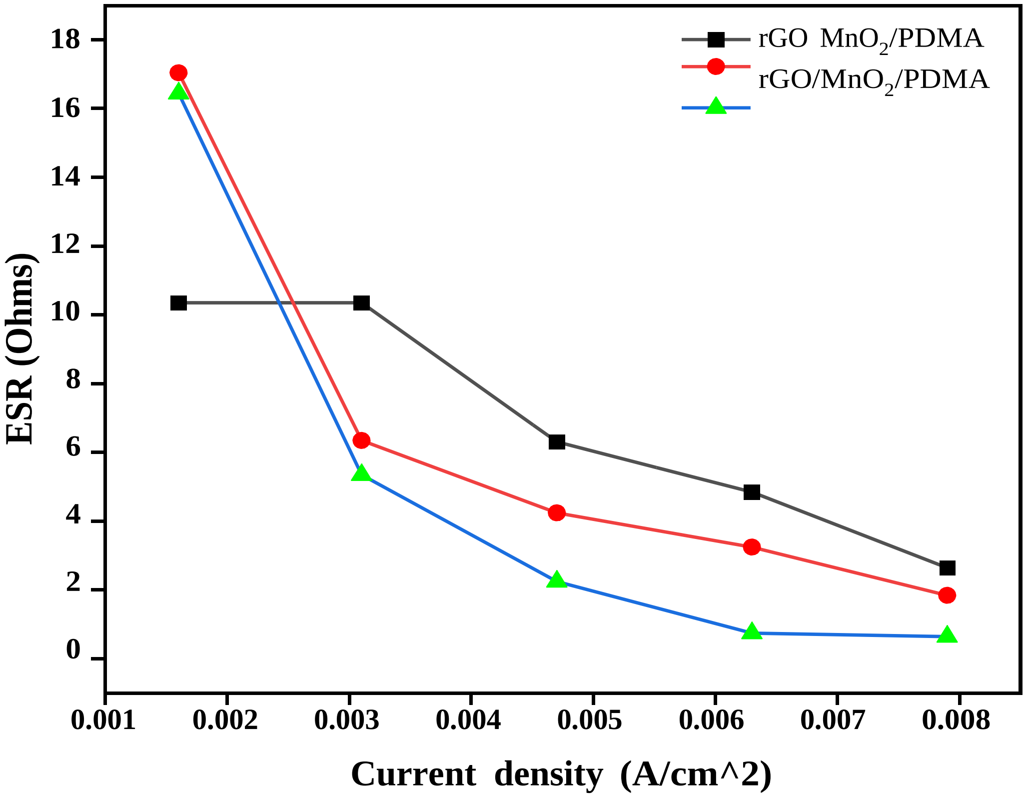

Figure 24. A graph of current densities(A/cm^2) against Electrochemical Series Resistance (ESR) (Ohms) of the samples in a two-electrode system

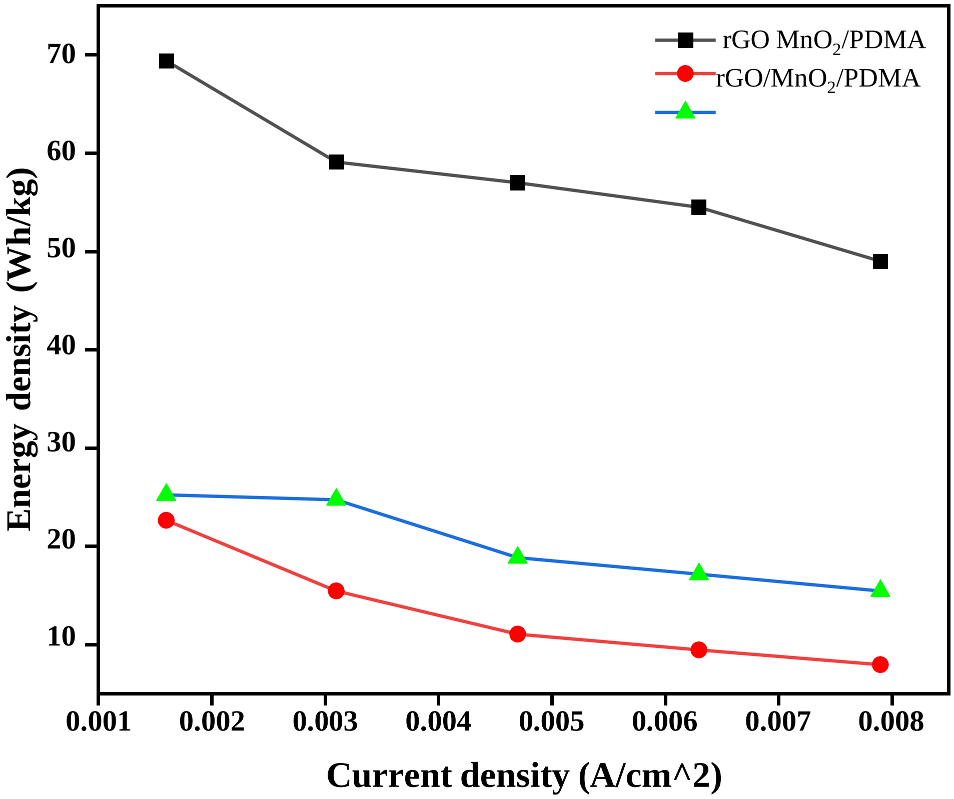

Figure 25. A plot of current densities (A/cm^2) against energy density (Wh/kg) of the synthesized samples in a three-electrode system

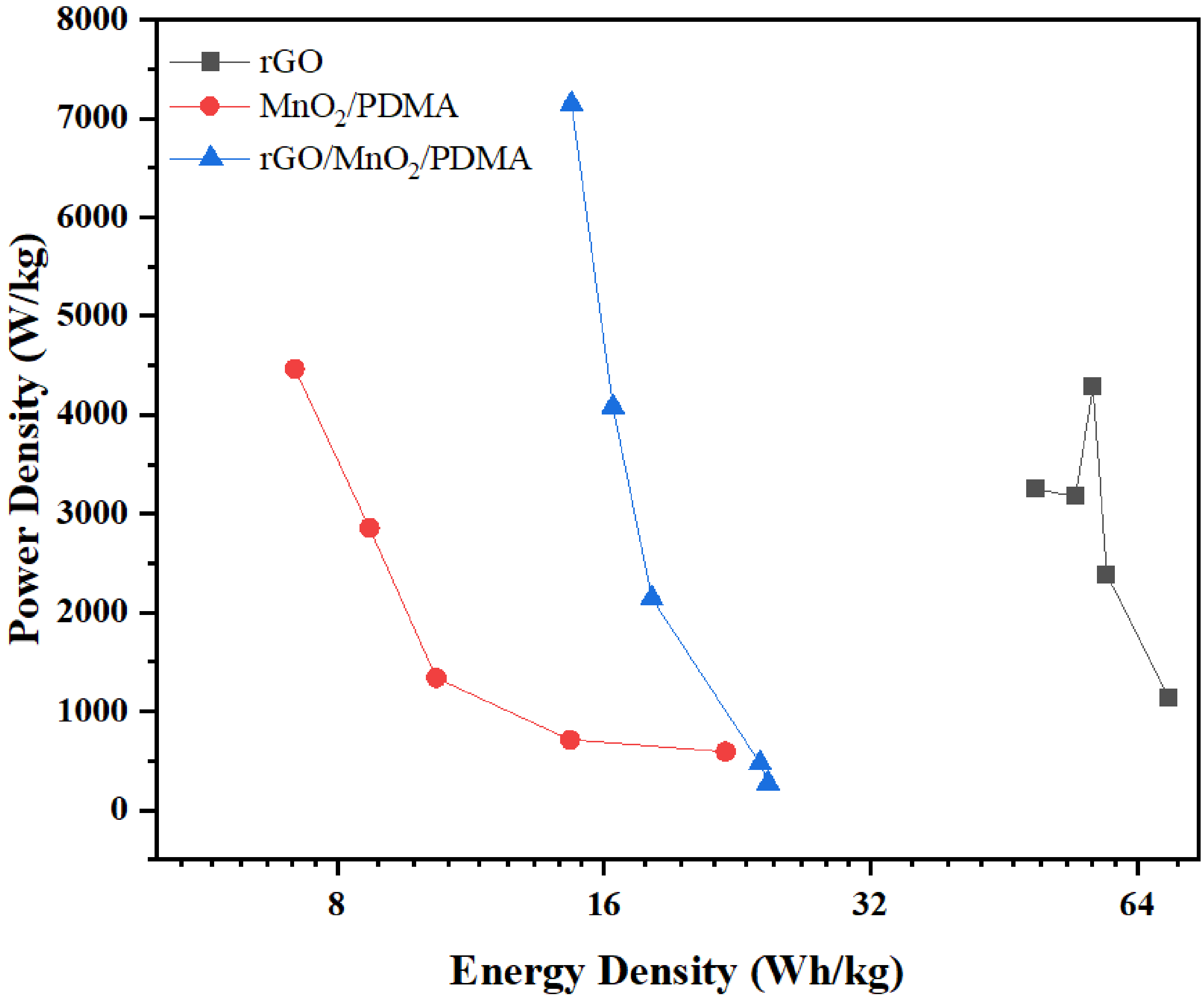

Figure 26. Ragone plot of energy density (Wh/kg) against power density(W/kg) of the synthesized samples

Table 5 A comparative specific capacitance, energy density, and power density results from different electrode materials in different works

Electrode material	Specific capacitance(F/g)	Energy density (Wh/kg)	Power density(W/kg)	Reference
rGO/PANI/MnO_2	512	66.6	1800	[97]
3D-graphene/MnO_2	333.4	51.2	400	[59]
Ppy/NwMnO_2	109	-	-	[41]
Fe_2O_3/PEDOT	252.8	136.3	10526	[35]
Li_2-S-PS_5	7.75	-	-	[32]
rGO/MnO_2/PDMA	176.4	24.5	725	This work

4.2.3. EIS measurements

To comprehend the interfacial charge transfer process for EDLCs and charge transfer due to redox reactions for pseudocapacitor materials, EIS measurements were conducted. The Nyquist plots of the nanocomposites rGO, PDMA, MnO_2/PDMA, and rGO/MnO_2/PDMA are displayed in *Figure 27* because the arc shape provides insight into the properties of charge transport and recombination. Due to the electrochemical double-layer supercapacitive behavior in the plot's shape, a semicircle appeared in the high-frequency region for rGO. This could be attributed to certain functional groups or defects at the surface of the carbon material contributing to the charge transfer resistance. A slight semi-circle appeared that became smaller in the order PDMA, MnO_2/PDMA, and rGO/MnO_2/PDMA respectively which showed that charge transfer resistance was reduced. The semi-circle could also occur as a result of the faradaic reactions occurring in the pseudocapacitive materials as well as due to interfacial impedance occurring at the interface between the current collector and the active material.

Figure 27 shows a comparison Nyquist plot for each electrode material sample. The following observations can be inferred from the plot, the rGO/MnO_2/PDMA curve is the closest to the imaginary axis, indicating the least charge transfer resistance; followed by the binary composite, PDMA, and finally rGO curve. The inset image is an enlarged image of the unresolved part of the curves, as indicated by the arrow. The furthest curve from the imaginary axis indicates the highest resistance, this could be due to the charge storage nature of EDLC material on the interface of the active material and the electrolyte. This exposes the device to resistances due to electrolyte, electrode, and current collector material. These findings are in per with S. Deng in his work titled "Synthesis and electrochemical properties of MnO_2 nanorods/graphene composites for supercapacitor applications"[89].

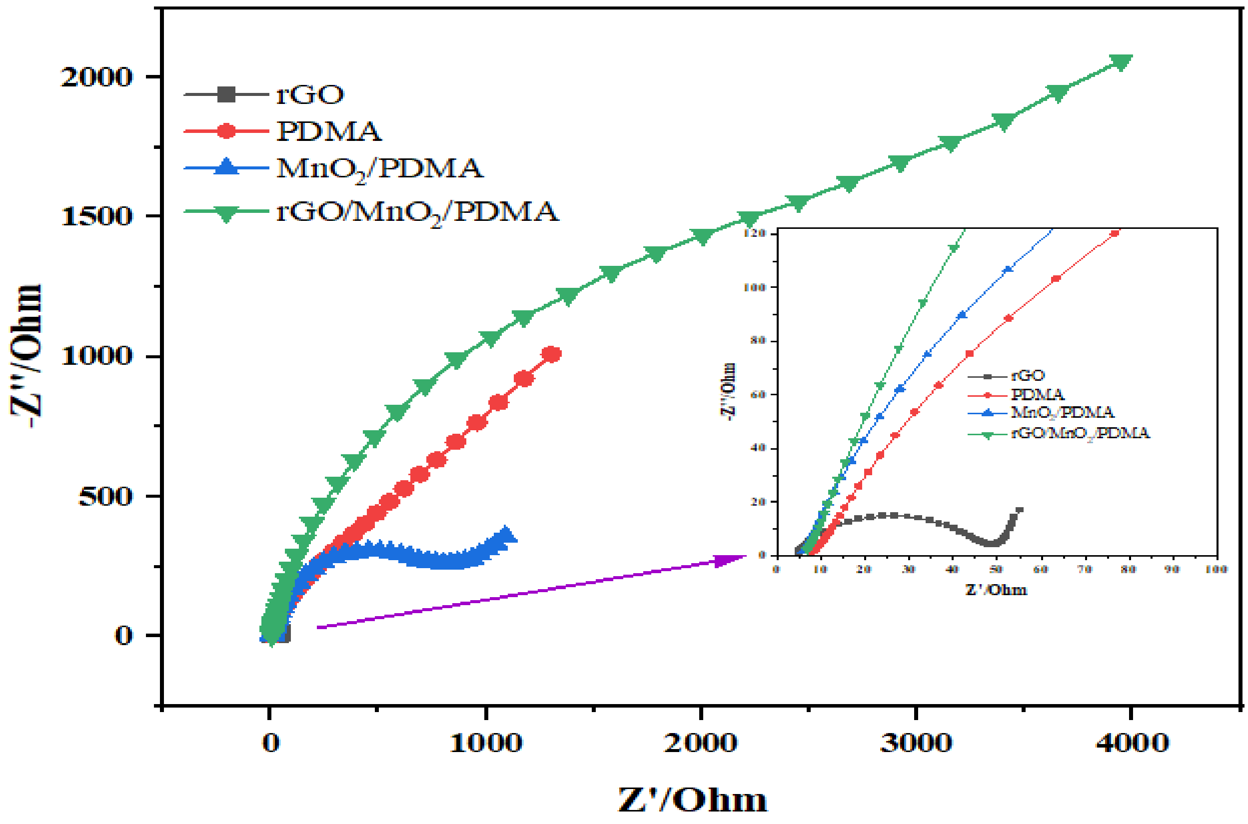

Figure 27. Nyquist plot for symmetric rGO, PDMA, MnO_2/PDMA, and rGO/MnO_2/PDMA. The Inset image shows an enlarged plot of the Nyquist plot.

Chapter Five

5. Conclusion

Four distinct types of electroactive materials (rGO, PDMA, MnO_2/PDMA, and rGO/MnO_2/PDMA) were successfully synthesized using the in-situ approach for the composite materials. FTIR, XRD, SEM, BET analysis, CV, GCD, and EIS were the characterization techniques used to understand the composite's evolution. For electrochemical analysis, three and two-electrode system supercapacitors were assembled. The three-electrode system was configured asymmetrically while the two-electrode system was configured both symmetrically and asymmetrically.

Specific capacitance, energy, and power densities, and ESR values were calculated from the GCD curves of the synthesized electrode materials. From the results obtained, it is evident that the three-electrode system gave significantly higher specific capacitance values, higher energy density values, and lower ESR values compared to the two-electrode system. This is because the three-electrode system performs a single electrode while the two-electrode system gives the capacitive performance of the whole cell, which is the realistic practical performance at the industrial level, hence the lower capacitive values. The asymmetric configuration in two electrode systems also gave higher capacitance and energy density and lower ESR values compared to the symmetric configurations of the same two-electrode system.

The ternary composite material registered its highest specific capacitance value of 176.4F/g, an energy density of 24.5Wh/kg, a power density of 725 W/kg, and an ESR value of 52Ω for three-electrode system at a current density of 0.0016Acm^2. To investigate the effect of the amount of MnO_2 in the composite material, the amount was reduced from 80% to 60% and 30% amount of MnO_2 in both the binary and ternary composite respectively. The results obtained show that as the amount of MnO_2 was reduced, the performance of the binary and ternary composite materials reduced as indicated by the lower specific capacitance, energy, and power densities values, and the increased ESR values. It has been observed that MnO_2 was successfully used to improve the specific capacitance of PDMA to a great extent. To lessen the widespread use of rGO in commercial evaluations, binary (MnO_2/PDMA) and ternary (rGO/MnO_2/PDMA) nanocomposite systems could be used as supercapacitor energy storage devices.

5.1. Recommendations

1. Different synthesis methods for the pure as well as composite materials could be employed and their performances compared to the methods already used in this work.
2. A quaternary composite material including a metal such as silver and iron could be synthesized and analysed for its electrochemical performance and compared to the ternary composite in this work.
3. More characterization techniques could be employed such as XPS, and TEM to get more detailed results.
4. More optimization options could be explored across different composite electrode materials (rGO and PDMA) to get the best-performing ratios for energy device applications.

References

[1] P. A. Owusu and S. Asumadu-Sarkodie, “A review of renewable energy sources, sustainability issues and climate change mitigation,” *Cogent Eng.*, vol. 3, no. 1, pp. 1–14, 2016, doi: 10.1080/23311916.2016.1167990.

[2] P. K. Chaurasiya, V. Warudkar, and S. Ahmed, “Wind energy development and policy in India: A review,” *Energy Strateg. Rev.*, vol. 24, no. April, pp. 342–357, 2019, doi: 10.1016/j.esr.2019.04.010.

[3] L. Wang, Y. Han, X. Feng, J. Zhou, P. Qi, and B. Wang, “Metal-organic frameworks for energy storage: Batteries and supercapacitors,” *Coord. Chem. Rev.*, vol. 307, pp. 361–381, 2016, doi: 10.1016/j.ccr.2015.09.002.

[4] A. K. Thakur, R. B. Choudhary, M. Majumder, G. Gupta, and M. V. Shelke, “Enhanced electrochemical performance of polypyrrole coated MoS2 nanocomposites as electrode material for supercapacitor application,” *J. Electroanal. Chem.*, vol. 782, pp. 278–287, 2016, doi: 10.1016/j.jelechem.2016.10.050.

[5] M. Majumder, R. B. Choudhary, A. K. Thakur, and I. Karbhal, “Impact of rare-earth metal oxide (Eu2O3) on the electrochemical properties of a polypyrrole/CuO polymeric composite for supercapacitor applications,” *RSC Adv.*, vol. 7, no. 32, pp. 20037–20048, 2017, doi: 10.1039/c7ra01438d.

[6] M. Du, Q. Li, Y. Zhao, C. Sen Liu, and H. Pang, “A review of electrochemical energy storage behaviors based on pristine metal–organic frameworks and their composites,” *Coord. Chem. Rev.*, vol. 416, p. 213341, 2020, doi: 10.1016/j.ccr.2020.213341.

[7] C. Zhong, Y. Deng, W. Hu, J. Qiao, L. Zhang, and J. Zhang, “A review of electrolyte materials and compositions for electrochemical supercapacitors,” vol. 44, no. 21, 2015, doi: 10.1039/c5cs00303b.

[8] B. Padya, R. Kali, P. K. Enaganti, N. Narasaiah, and P. K. Jain, “Facile synthesis and frequency-response behavior of supercapacitor electrode based on surface-etched nanoscaled-graphene platelets,” *Colloids Surfaces A Physicochem. Eng. Asp.*, vol. 609, no. July 2020, p. 125587, 2021, doi: 10.1016/j.colsurfa.2020.125587.

[9] Y. Zhao, J. Liu, M. Horn, N. Motta, M. Hu, and Y. Li, “Recent advancements in metal organic framework based electrodes for supercapacitors,” *Sci. China Mater.*, vol. 61, no. 2, pp. 159–184, 2018, doi: 10.1007/s40843-017-9153-x.

[10] R. B. Choudhary, S. Ansari, and M. Majumder, “Recent advances on redox active composites of metal-organic framework and conducting polymers as pseudocapacitor electrode material,” *Renew. Sustain. Energy Rev.*, vol. 145, no. February, p. 110854, 2021, doi: 10.1016/j.rser.2021.110854.

[11] Y. N. Liu, L. N. Jin, H. T. Wang, X. H. Kang, and S. W. Bian, “Fabrication of three-dimensional composite textile electrodes by metal-organic framework, zinc oxide, graphene and polyaniline for all-solid-state supercapacitors,” *J. Colloid Interface Sci.*, vol. 530, pp. 29–36, 2018, doi: 10.1016/j.jcis.2018.06.062.

[12] S. H. Nagarajarao *et al.*, “Recent Developments in Supercapacitor Electrodes: A Mini Review,” *ChemEngineering*, vol. 6, no. 1, 2022, doi: 10.3390/chemengineering6010005.

[13] X. Lu *et al.*, “Facile synthesis of large-area manganese oxide nanorod arrays as a high-performance electrochemical supercapacitor,” *Energy Environ. Sci.*, vol. 4, no. 8, pp. 2915–2921, 2011, doi: 10.1039/c1ee01338f.

[14] S. Ramesh, S. Khandelwal, K. Y. Rhee, and D. Hui, “Synergistic effect of reduced

graphene oxide, CNT and metal oxides on cellulose matrix for supercapacitor applications," *Compos. Part B Eng.*, vol. 138, no. November 2017, pp. 45–54, 2018, doi: 10.1016/j.compositesb.2017.11.024.

[15] D. N. Ampong *et al.*, *MXene: fundamentals to applications in electrochemical energy storage*, vol. 18, no. 1. Springer US, 2023. doi: 10.1186/s11671-023-03786-9.

[16] Z. S. Iro, C. Subramani, and S. S. Dash, "A brief review on electrode materials for supercapacitor," *Int. J. Electrochem. Sci.*, vol. 11, no. 12, pp. 10628–10643, 2016, doi: 10.20964/2016.12.50.

[17] A. K. Thakur, M. Majumder, R. B. Choudhary, and S. B. Singh, "MoS2 flakes integrated with boron and nitrogen-doped carbon: Striking gravimetric and volumetric capacitive performance for supercapacitor applications," *J. Power Sources*, vol. 402, no. August, pp. 163–173, 2018, doi: 10.1016/j.jpowsour.2018.09.029.

[18] T. K. Das and S. Prusty, "Review on Conducting Polymers and Their Applications," *Polym. - Plast. Technol. Eng.*, vol. 51, no. 14, pp. 1487–1500, 2012, doi: 10.1080/03602559.2012.710697.

[19] R. Wang, M. Yao, and Z. Niu, "Smart supercapacitors from materials to devices," *InfoMat*, vol. 2, no. 1, pp. 113–125, 2020, doi: 10.1002/inf2.12037.

[20] D. P. Dubal, N. R. Chodankar, D. H. Kim, and P. Gomez-Romero, "Towards flexible solid-state supercapacitors for smart and wearable electronics," *Chem. Soc. Rev.*, vol. 47, no. 6, pp. 2065–2129, 2018, doi: 10.1039/c7cs00505a.

[21] T. Zhai *et al.*, "3D MnO2–graphene composites with large areal capacitance for high-performance asymmetric supercapacitors," *Nanoscale*, vol. 5, no. 15, pp. 6790–6796, 2013, doi: 10.1039/c3nr01589k.

[22] R. Kalifa, "Electrochemical behavior of conducting polymers," 2022.

[23] S. K. Kandasamy and K. Kandasamy, "Recent Advances in Electrochemical Performances of Graphene Composite (Graphene-Polyaniline/Polypyrrole/Activated Carbon/Carbon Nanotube) Electrode Materials for Supercapacitor: A Review," *J. Inorg. Organomet. Polym. Mater.*, vol. 28, no. 3, pp. 559–584, 2018, doi: 10.1007/s10904-018-0779-x.

[24] Q. Meng, K. Cai, Y. Chen, and L. Chen, "Research progress on conducting polymer based supercapacitor electrode materials," *Nano Energy*, vol. 36, no. April, pp. 268–285, 2017, doi: 10.1016/j.nanoen.2017.04.040.

[25] M. Sajjad, M. Ibrar, F. Cheng, and W. Lu, "A review on selection criteria of aqueous electrolytes performance evaluation for advanced asymmetric supercapacitors," *J. Energy Storage*, vol. 40, no. May, p. 102729, 2021, doi: 10.1016/j.est.2021.102729.

[26] W. Ye, H. Wang, J. Ning, Y. Zhong, and Y. Hu, "Review New types of hybrid electrolytes for supercapacitors," *J. Energy Chem.*, 2020, doi: 10.1016/j.jechem.2020.09.016.

[27] J. Feng, "Environmental Science Ion regulation of ionic liquid electrolytes for supercapacitors," pp. 20–22, 2021, doi: 10.1039/d0ee04002a.

[28] P. E. Lokhande, "Chapter 2 Inorganic Electrolytes in Supercapacitor," no. May, pp. 10–30, 2022, doi: 10.21741/9781644900499-2.

[29] B. E. Francisco and C. R. Stoldt, "Energetics of Ion Transport in NASICON-Type Electrolytes," 2015, doi: 10.1021/acs.jpcc.5b03286.

[30] P. Lokhande and U. Chavan, "Inorganic Electrolytes in Supercapacitor," 2019, pp. 11–30. doi: 10.21741/9781644900499-2.

[31] R. Liang *et al.*, "Transition Metal Oxide Electrode Materials for Supercapacitors : A Review of Recent Developments," 2021.

[32] M. Ates, I. Mizrak, O. Kuzgun, and S. Aktas, "Synthesis , characterization , and supercapacitor performances of activated and inactivated rGO / MnO 2 and rGO / MnO 2 / PPy nanocomposites," 2020.

[33] M. Tomczykowa and M. E. Plonska-Brzezinska, "Conducting polymers, hydrogels and their composites: Preparation, properties and bioapplications," *Polymers (Basel).*, vol. 11, no. 2, pp. 1–36, 2019, doi: 10.3390/polym11020350.

[34] S. Banerjee and K. K. Kar, "Conducting polymers as electrode materials for supercapacitors," *Springer Ser. Mater. Sci.*, vol. 302, pp. 333–352, 2020, doi: 10.1007/978-3-030-52359-6_13.

[35] P. Forouzandeh, V. Kumaravel, and S. C. Pillai, "Electrode materials for supercapacitors: A review of recent advances," *Catalysts*, vol. 10, no. 9, pp. 1–73, 2020, doi: 10.3390/catal10090969.

[36] P. H. Wadekar, R. V. Khose, D. A. Pethsangave, and S. Some, "One-step Preparation of Conducting Polymer/Metal Oxide Doped RGO Trinary Composite for Supercapacitor Applications," *ChemistrySelect*, vol. 5, no. 38, pp. 11769–11777, 2020, doi: 10.1002/slct.202002911.

[37] E. Lim, C. Jo, and J. Lee, "A mini review of designed mesoporous materials for energy-storage applications: From electric double-layer capacitors to hybrid supercapacitors," *Nanoscale*, vol. 8, no. 15, pp. 7827–7833, 2016, doi: 10.1039/c6nr00796a.

[38] Q. Cheng, J. Tang, J. Ma, H. Zhang, N. Shinya, and L. C. Qin, "Graphene and nanostructured MnO2 composite electrodes for supercapacitors," *Carbon N. Y.*, vol. 49, no. 9, pp. 2917–2925, 2011, doi: 10.1016/j.carbon.2011.02.068.

[39] V. C. Lokhande, A. C. Lokhande, C. D. Lokhande, J. H. Kim, and T. Ji, "Supercapacitive composite metal oxide electrodes formed with carbon, metal oxides and conducting polymers," *J. Alloys Compd.*, vol. 682, pp. 381–403, 2016, doi: 10.1016/j.jallcom.2016.04.242.

[40] Q. Li *et al.*, "Extra storage capacity in transition metal oxide lithium-ion batteries revealed by in situ magnetometry," *Nat. Mater.*, doi: 10.1038/s41563-020-0756-y.

[41] B. Liu *et al.*, "Optimized synthesis of nitrogen-doped carbon with extremely high surface area for adsorption and supercapacitor," *Appl. Surf. Sci.*, vol. 538, no. August 2020, p. 147961, 2021, doi: 10.1016/j.apsusc.2020.147961.

[42] G. Yang and S. J. Park, "MnO2 and biomass-derived 3D porous carbon composites electrodes for high performance supercapacitor applications," *J. Alloys Compd.*, vol. 741, pp. 360–367, 2018, doi: 10.1016/j.jallcom.2018.01.108.

[43] N. Wang, P. Zhao, K. Liang, M. Yao, Y. Yang, and W. Hu, "CVD-grown polypyrrole nanofilms on highly mesoporous structure MnO2 for high performance asymmetric supercapacitors," *Chem. Eng. J.*, vol. 307, pp. 105–112, 2017, doi: 10.1016/j.cej.2016.08.074.

[44] G. Wang, Z. Jin, and Q. Guo, "Ordered Self-supporting NiV LDHs@P-Nickel foam Nano-array as High-Performance supercapacitor electrode," *J. Colloid Interface Sci.*, vol. 583, pp. 1–12, 2021, doi: 10.1016/j.jcis.2020.08.127.

[45] L. Ma, X. Shen, H. Zhou, Z. Ji, K. Chen, and G. Zhu, "High performance supercapacitor electrode materials based on porous NiCo2O4 hexagonal nanoplates/reduced graphene oxide composites," *Chem. Eng. J.*, vol. 262, pp. 980–988, 2015, doi: 10.1016/j.cej.2014.10.079.

[46] Y. Liu, X. Zhang, K. Matras-Postolek, and P. Yang, "Ni2P nanosheets modified N-doped

hollow carbon spheres towards enhanced supercapacitor performance," *J. Alloys Compd.*, vol. 854, p. 157111, 2021, doi: 10.1016/j.jallcom.2020.157111.

[47] H. Chen, X. Du, J. Sun, R. Wu, Y. Wang, and C. Xu, "Template-free synthesis of novel Co3O4 micro-bundles assembled with flakes for high-performance hybrid supercapacitors," *Ceram. Int.*, vol. 47, no. 1, pp. 716–724, 2021, doi: 10.1016/j.ceramint.2020.08.181.

[48] M. Dai, D. Zhao, and X. Wu, "Research progress on transition metal oxide based electrode materials for asymmetric hybrid capacitors," *Chinese Chem. Lett.*, vol. 31, no. 9, pp. 2177–2188, 2020, doi: 10.1016/j.cclet.2020.02.017.

[49] P. Hu, D. Zhao, H. Liu, K. Chen, and X. Wu, "Engineering PPy decorated MnCo2O4 urchins for quasi-solid-state hybrid capacitors," *CrystEngComm*, vol. 21, no. 10, pp. 1600–1606, 2019, doi: 10.1039/c8ce01959b.

[50] S. D. Raut *et al.*, "Electrochemically grown MnO2nanowires for supercapacitor and electrocatalysis applications," *New J. Chem.*, vol. 44, no. 41, pp. 17864–17870, 2020, doi: 10.1039/d0nj03792c.

[51] P. Liu *et al.*, "Rational construction of bowl-like MnO2 nanosheets with excellent electrochemical performance for supercapacitor electrodes," *Chem. Eng. J.*, vol. 350, no. March, pp. 79–88, 2018, doi: 10.1016/j.cej.2018.05.169.

[52] L. Wang, Y. Ouyang, X. Jiao, X. Xia, W. Lei, and Q. Hao, "Polyaniline-assisted growth of MnO2 ultrathin nanosheets on graphene and porous graphene for asymmetric supercapacitor with enhanced energy density," *Chem. Eng. J.*, vol. 334, pp. 1–9, 2018, doi: 10.1016/j.cej.2017.10.005.

[53] P. Zhao, M. Yao, H. Ren, N. Wang, and S. Komarneni, "Nanocomposites of hierarchical ultrathin MnO 2 nanosheets/hollow carbon nanofibers for high-performance asymmetric supercapacitors," *Appl. Surf. Sci.*, vol. 463, pp. 931–938, 2019, doi: 10.1016/j.apsusc.2018.09.041.

[54] X. L. Bai *et al.*, "Supercapacitor performance of 3D-graphene/MnO2foam synthesized via the combination of chemical vapor deposition with hydrothermal method," *Appl. Phys. Lett.*, vol. 117, no. 18, 2020, doi: 10.1063/5.0018708.

[55] J. Jang, "Emissive Materials Nanomaterials," *Adv. Polym. Sci.*, vol. 199, no. 1, pp. 189–259, 2006.

[56] M. El Rhazi, S. Majid, M. Elbasri, F. E. Salih, L. Oularbi, and K. Lafdi, "Recent progress in nanocomposites based on conducting polymer: application as electrochemical sensors," *Int. Nano Lett.*, vol. 8, no. 2, pp. 79–99, 2018, doi: 10.1007/s40089-018-0238-2.

[57] T. Ghosh *et al.*, "Hierarchical Nanocomposites by Oligomer-Initiated Controlled Polymerization of Aniline on Graphene Oxide Sheets for Energy Storage," *ACS Appl. Nano Mater.*, vol. 3, no. 2, pp. 1693–1705, 2020, doi: 10.1021/acsanm.9b02406.

[58] F. Ghorbani Zamani, H. Moulahoum, M. Ak, D. Odaci Demirkol, and S. Timur, "Current trends in the development of conducting polymers-based biosensors," *TrAC - Trends Anal. Chem.*, vol. 118, pp. 264–276, 2019, doi: 10.1016/j.trac.2019.05.031.

[59] S. Ben Jadi *et al.*, "Electropolymerization and corrosion resistance of polypyrrole on nickel bipolar plate for PEM fuel cell application," *Mater. Today Proc.*, vol. 22, no. xxxx, pp. 52–56, 2020, doi: 10.1016/j.matpr.2019.08.072.

[60] Y. Han and L. Dai, "Conducting Polymers for Flexible Supercapacitors," *Macromol. Chem. Phys.*, vol. 220, no. 3, pp. 1–14, 2019, doi: 10.1002/macp.201800355.

[61] D. Patil, Y. K. Seo, Y. K. Hwang, J. S. Chang, and P. Patil, "Humidity sensitive poly(2,5-

dimethoxyaniline)/WO3 composites," *Sensors Actuators, B Chem.*, vol. 132, no. 1, pp. 116–124, 2008, doi: 10.1016/j.snb.2008.01.021.

[62] Y. Yang, W. Yuan, S. Li, X. Yang, J. Xu, and Y. Jiang, "Manganese dioxide nanoparticle enrichment in porous conducting polymer as high performance supercapacitor electrode materials," *Electrochim. Acta*, vol. 165, pp. 323–329, 2015, doi: 10.1016/j.electacta.2015.03.052.

[63] S. N. Alam, N. Sharma, and L. Kumar, "Synthesis of Graphene Oxide (GO) by Modified Hummers Method and Its Thermal Reduction to Obtain Reduced Graphene Oxide (rGO)*," *Graphene*, vol. 06, no. 01, pp. 1–18, 2017, doi: 10.4236/graphene.2017.61001.

[64] J. Cherusseri, D. Pandey, and J. Thomas, "Symmetric, Asymmetric, and Battery-Type Supercapacitors Using Two-Dimensional Nanomaterials and Composites," *Batter. Supercaps*, vol. 3, no. 9, pp. 860–875, 2020, doi: 10.1002/batt.201900230.

[65] F. Baig, Y. Hameed Khattak, S. Jemai, B. Marí Soucase, and S. Beg, "Hydrothermal syntheses of Vanadium doped A-Fe2O3 cubic particles with enhanced photoelectrochemical activity," *Sol. Energy*, vol. 182, no. February, pp. 332–339, 2019, doi: 10.1016/j.solener.2019.02.066.

[66] S. Yu *et al.*, "Synthesis and application of iron-based nanomaterials as anodes of lithium-ion batteries and supercapacitors," *J. Mater. Chem. A*, vol. 6, no. 20, pp. 9332–9367, 2018, doi: 10.1039/c8ta01683f.

[67] Y. Shao *et al.*, "Design and Mechanisms of Asymmetric Supercapacitors," *Chem. Rev.*, vol. 118, no. 18, pp. 9233–9280, 2018, doi: 10.1021/acs.chemrev.8b00252.

[68] N. Wu *et al.*, "Recent Advances of Asymmetric Supercapacitors," *Adv. Mater. Interfaces*, vol. 8, no. 1, pp. 1–17, 2021, doi: 10.1002/admi.202001710.

[69] S. X. Deng *et al.*, "Synthesis and electrochemical properties of MnO2 nanorods/graphene composites for supercapacitor applications," *Electrochim. Acta*, vol. 111, pp. 707–712, 2013, doi: 10.1016/j.electacta.2013.08.055.

[70] M. Dowsett, R. Wiesinger, and M. Adriaens, "X-ray diffraction," *Spectrosc. Diffr. Tomogr. Art Herit. Sci.*, pp. 161–207, 2021, doi: 10.1016/B978-0-12-818860-6.00011-8.

[71] B. C. Roy, M. D. Gupta, L. Bhowmik, and J. K. Ray, "Synthesis and characterization of poly(2,5-dimethoxyaniline) and poly(aniline-Co-2,5-dimethoxyaniline): The processable conducting polymers," *Bull. Mater. Sci.*, vol. 24, no. 4, pp. 389–396, 2001, doi: 10.1007/BF02708636.

[72] B. J. Inkson, *Scanning Electron Microscopy (SEM) and Transmission Electron Microscopy (TEM) for Materials Characterization*. Elsevier Ltd, 2016. doi: 10.1016/B978-0-08-100040-3.00002-X.

[73] R. Bhargava, S. Q. Wang, and J. L. Koenig, "FTIR microspectroscopy of polymeric systems," *Adv. Polym. Sci.*, vol. 163, pp. 137–191, 2003, doi: 10.1007/b11052.

[74] D. C. Lingegowda, J. K. Kumar, A. G. D. Prasad, M. Zarei, and S. Gopal, "Ftir Spectroscopic Studies on Cleome Gynandra – Comparative," *Rom. J. Biophys.*, vol. 22, no. June 2014, pp. 137–143, 2013.

[75] Y. Jia, A. Ahmed, X. Jiang, L. Zhou, Q. Fan, and J. Shao, "Microfluidic fabrication of hierarchically porous superconductive carbon black/graphene hybrid fibers for wearable supercapacitor with high specific capacitance," *Electrochim. Acta*, vol. 354, p. 136731, 2020, doi: 10.1016/j.electacta.2020.136731.

[76] C. Zhang and N. Lu, "Augmented Brunauer–Emmett–Teller Equation for Water Adsorption on Soils," *Vadose Zo. J.*, vol. 18, no. 1, pp. 1–12, 2019, doi:

10.2136/vzj2019.01.0011.

[77] M. Thommes, R. Guillet-Nicolas, and K. A. Cychosz, “Physical Adsorption Characterization of Mesoporous Zeolites,” *Mesoporous Zeolites Prep. Charact. Appl.*, pp. 349–384, 2015, doi: 10.1002/9783527673957.ch11.

[78] P. Sinha, A. Datar, C. Jeong, X. Deng, Y. G. Chung, and L. C. Lin, “Surface Area Determination of Porous Materials Using the Brunauer-Emmett-Teller (BET) Method: Limitations and Improvements,” *J. Phys. Chem. C*, vol. 123, no. 33, pp. 20195–20209, 2019, doi: 10.1021/acs.jpcc.9b02116.

[79] Z. A. Alothman, “A review: Fundamental aspects of silicate mesoporous materials,” *Materials (Basel).*, vol. 5, no. 12, pp. 2874–2902, 2012, doi: 10.3390/ma5122874.

[80] B. Zhang, S. Song, W. Li, L. Zheng, and X. Ma, “Asymmetric supercapacitors with high energy density and high specific capacitance based on Ni-Co-Mn multiphase metal structure MOF,” *Ionics (Kiel).*, vol. 27, no. 8, pp. 3553–3566, 2021, doi: 10.1007/s11581-021-04056-3.

[81] S. Wu *et al.*, “An Aqueous Zn-Ion Hybrid Supercapacitor with High Energy Density and Ultrastability up to 80 000 Cycles,” *Adv. Energy Mater.*, vol. 9, no. 47, pp. 1–7, 2019, doi: 10.1002/aenm.201902915.

[82] S. Sharma and P. Chand, “Supercapacitor and electrochemical techniques: A brief review,” *Results in Chemistry*, vol. 5. 2023. doi: 10.1016/j.rechem.2023.100885.

[83] M. Shanmugavadivel, V. V. Dhayabaran, and M. Subramanian, “Fabrication of high energy and high power density supercapacitor based on MnCo2O4 nanomaterial,” *J. Phys. Chem. Solids*, vol. 133, no. April, pp. 15–20, 2019, doi: 10.1016/j.jpcs.2019.04.029.

[84] F. Ciucci, “Modeling electrochemical impedance spectroscopy,” *Curr. Opin. Electrochem.*, vol. 13, pp. 132–139, 2019, doi: 10.1016/j.coelec.2018.12.003.

[85] S. Kandambeth *et al.*, “Covalent Organic Frameworks as Negative Electrodes for High-Performance Asymmetric Supercapacitors,” *Adv. Energy Mater.*, vol. 10, no. 38, pp. 1–9, 2020, doi: 10.1002/aenm.202001673.

[86] Z. Wang, J. Ni, L. Li, and J. Lu, “Theoretical Simulation and Modeling of Three-Dimensional Batteries,” *Cell Reports Phys. Sci.*, vol. 1, no. 6, p. 100078, 2020, doi: 10.1016/j.xcrp.2020.100078.

[87] D. Ickecan, R. Zan, and S. Nezir, “Eco-Friendly Synthesis and Characterization of Reduced Graphene Oxide,” *J. Phys. Conf. Ser.*, vol. 902, no. 1, 2017, doi: 10.1088/1742-6596/902/1/012027.

[88] M. Masikini *et al.*, “Label free poly(2,5-dimethoxyaniline)-multi-walled carbon nanotubes impedimetric immunosensor for fumonisin B1 detection,” *Materials (Basel).*, vol. 9, no. 4, 2016, doi: 10.3390/ma9040273.

[89] G. Han *et al.*, “MnO2 nanorods intercalating graphene oxide/polyaniline ternary composites for robust high-performance supercapacitors,” *Sci. Rep.*, vol. 4, 2014, doi: 10.1038/srep04824.

[90] S. Xiong *et al.*, “Fabrication of high yield and highly crystalline poly(2,5-dimethoxyanline) nanoplates using various organic sulfonic acids as the dopant agents and soft-templates,” *J. Mater. Sci. Mater. Electron.*, vol. 27, no. 11, pp. 11142–11150, 2016, doi: 10.1007/s10854-016-5232-8.

[91] V. Sannasi and K. Subbian, “Influence of Moringa oleifera gum on two polymorphs synthesis of MnO2 and evaluation of the pseudo-capacitance activity,” *J. Mater. Sci. Mater. Electron.*, vol. 31, no. 19, pp. 17120–17132, 2020, doi: 10.1007/s10854-020-

04272-z.

APPENDIX A

A.1.SEM images of rGO and PDMA

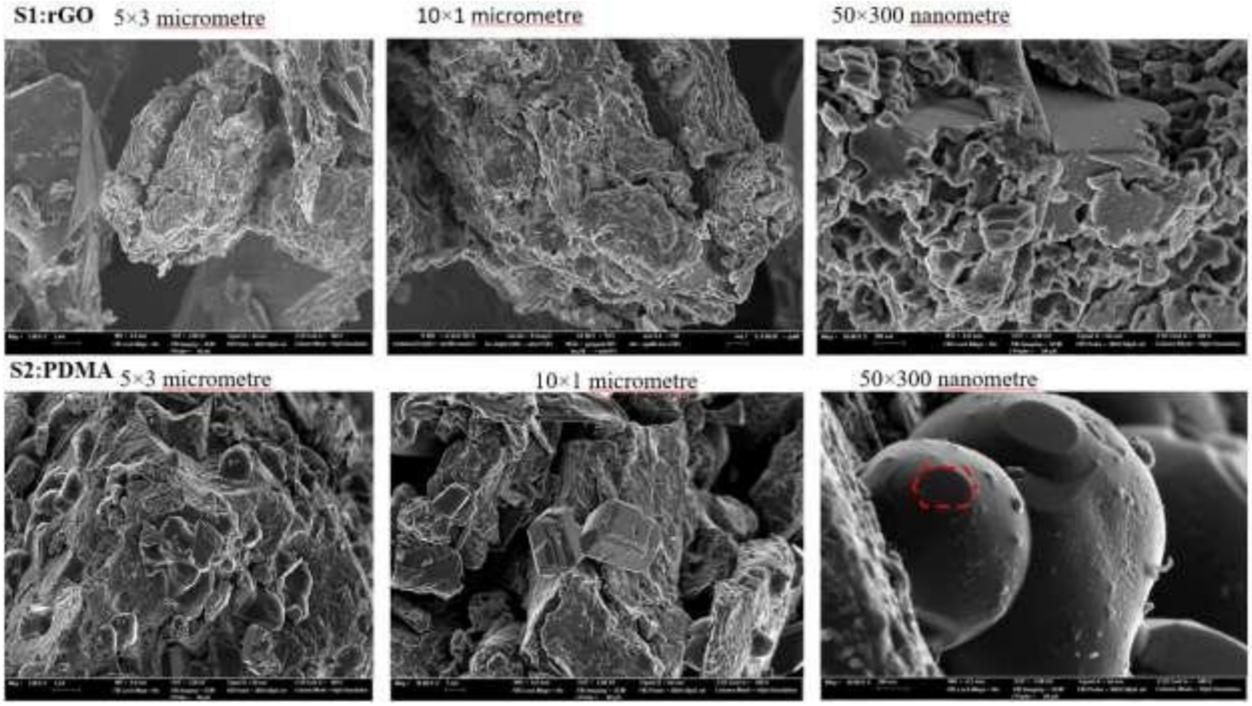

Figure A1 SEM-EDS morphological images of 5*3, 10*1 micrometre, and 50*300nanometre for rGO and PDMA

A.2. SEM images of binary and ternary composites

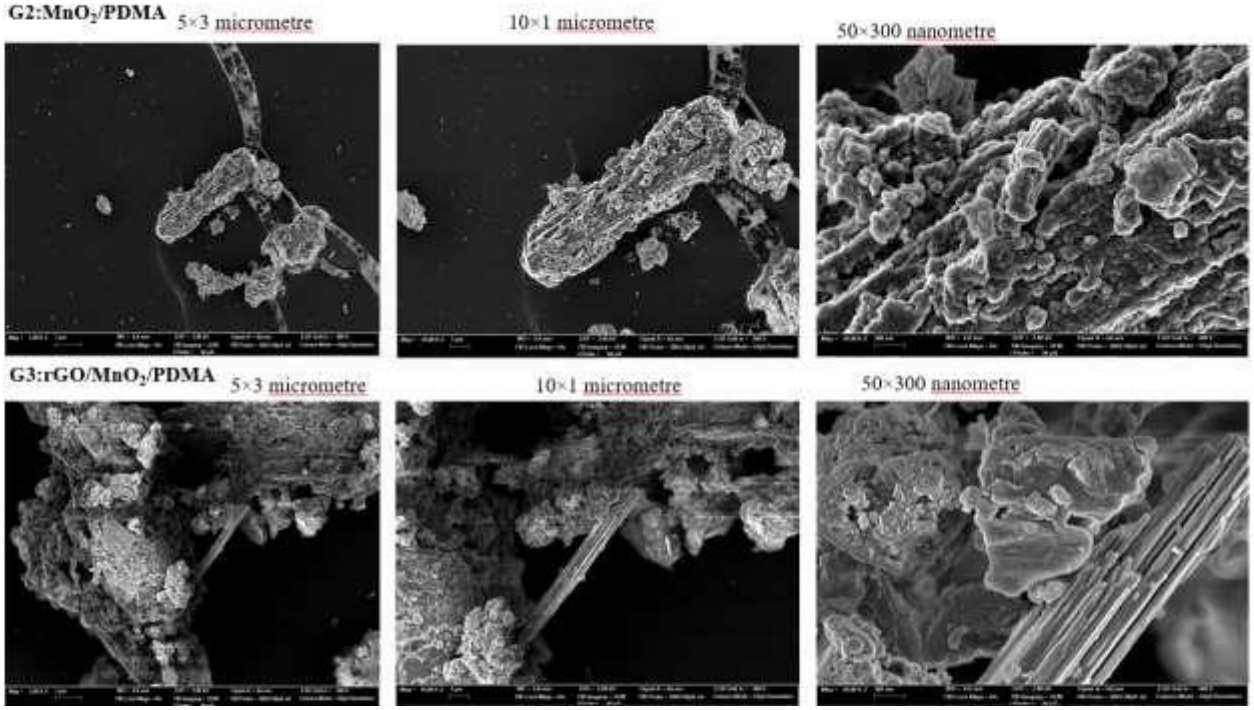

Figure A2 SEM-EDS morphological images of 5*3, 10*1micrometre, and 50*300nanometre for MnO$_2$/PDMA and rGO/MnO$_2$/PDMA

A.3.Laboratory Images

Figure A3 Laboratory images of the experimental process